Astronomy Letters, Vol. 26, No. 1, 2000, pp. 1–8. Translated from Pis'ma v Astronomicheskiĭ Zhurnal, Vol. 26, No. 1, 2000, pp. 3–12.

ART-P/Granat Observations of the X-ray Pulsar 4U0115+634 during the Outburst in February 1990

A. A. Lutovinov[1], S. A. Grebenev[1]*, and R. A. Sunyaev[1, 2]

[1] *Space Research Institute, Russian Academy of Sciences, ul. Profsoyuznaya 84/32, Moscow, 117810 Russia*
[2] *Max-Planck Institut für Astrophysik, Garching, Germany*

Received April 6, 1999

Abstract—Observations of the transient X-ray pulsar 4U0115+634 with the ART-P telescope aboard the Granat Observatory during the outburst in February 1990 are presented. The source exhibited a strong, regular and irregular variability, including X-ray bursts of duration 300–500 s. Two absorption features were detected in the source's photon spectrum at ~12 and ~22 keV, which were interpreted as the lines of resonance scattering of its emission at the first and second cyclotron harmonics. The magnetic-field strength B on the neutron-star surface that corresponds to these lines is $\sim 1.3 \times 10^{12}$ G. The ratio of the line energies slightly differs from the harmonic ratio 1 : 2. Moreover, this ratio and the line energies themselves vary appreciably with phase on a time scale of one pulsation period. The dependence of other spectral parameters for 4U0115+634 on pulse phase is investigated. © *2000 MAIK "Nauka/Interperiodica"*.

INTRODUCTION

The transient X-ray source 4U0115+634 was discovered by the Uhuru satellite during its outburst in January 1971 [1]. Subsequently, during the giant outburst of 1978 [2], pulsations of its emission with a period of 3.6 s were detected. These pulsations showed that the object is a rapidly rotating, accreting neutron star with a strong magnetic field. Doppler shifts in the period allowed the binary's parameters—its orbital period $P_{\rm orb} \simeq 24.3$ days, eccentricity $e \simeq 0.34$, and projection of the orbital semimajor axis $a_{\rm X}\sin i \simeq$ 140 light seconds—to be measured [3]. At the same time, the properties of the optical companion—the star V635 Cas—have long remained unknown. Only recently have Unger *et al.* [4] showed that this star is a supergiant of spectral type O9e. Long-term observations of the binary system suggest that X-ray outbursts occur approximately once every three years and last for several weeks [5–8]. Giant outbursts, during which the source's X-ray luminosity increases by tens or hundreds of times to reach the Crab luminosity, occur even more rarely. The positive correlation between the source's optical and X-ray activities (with a delay between X-ray and optical events of several months), which was found by Mendelson and Mazeh [9] for a number of outbursts, indicates that the outbursts are attributable to occasional envelope ejection by V635 Cas; accretion begins only after a sufficient amount of material capable of overcoming the centrifugal barrier at the neutron-star magnetospheric boundary is accumulated in the capture region [10].

The source 4U0115+634 is a bright representative of the group of "hard" X-ray transients; by their properties, they differ markedly from "soft" transients, X-ray novae. In general, its spectrum is well described by a power law with a photon index $\alpha \sim 0.5$ and with an exponential cutoff at energies above 10–15 keV. While analyzing the HEAO-1 data, Wheaton *et al.* [11] detected an absorption line near ~20 keV in the pulsar spectrum. Subsequent observations showed that there were actually two features at $\simeq 11.5$ and $\simeq 23$ keV in the source's spectrum [12, 13]. These features were interpreted as the cyclotron absorption lines in a strong magnetic field that correspond to the fundamental frequency and its second harmonic. Recently, the detection of a third harmonic with energy ~33.6 keV by the RXTE satellite has been reported [14]. Occasionally, the source exhibits even more unusual properties. In particular, during the outburst of 1994, it was found by the HEXE instrument aboard the Mir-Kvant module in an abnormally hard state with a power-law spectrum up to ~100 keV without any evidence of a cutoff at high energies [15].

In this paper, we present the observations of the pulsar 4U0115+634 with the ART-P telescope aboard the Granat Observatory in February 1990 during a strong (giant) X-ray outburst.

OBSERVATIONS

The onset of this outburst was detected on February 5, 1990, by the Japanese Ginga satellite [16]. Shortly afterward (on February 18, 19, and 22), three observing sessions of the pulsar were carried out with the ART-P telescope with exposures of 6420, 2070, and 6310 s, respectively.

The coded-aperture ART-P telescope has a $3\overset{\circ}{.}4 \times 3\overset{\circ}{.}6$ field of view (FWHM) and an angular resolution of 5′ (the coded-mask element size). The geo-

* e-mail: sergei@hea.iki.rssi.ru

metric area of the telescope position-sensitive detector is 625 cm^2; half of the detector is covered with opaque mask elements. The telescope is sensitive to photons in the energy band 2.5–60 keV and has an energy resolution of ~22% in the 5.9-keV iron line. A detailed description of the telescope is given in [17].

The observations were performed in the "photon-by-photon" mode, in which, for each photon, its coordinates on the detector, energy (1024 channels), and arrival time were written into buffer memory. Since the data transfer to the satellite's main memory was made after the temporary buffer was filled and took 25–35 s, on the average, the written information takes the form of individual exposures with breaks between them.

Figure 1 shows the image of the field near 4U0115+634 which was obtained during the observing session on February 19. Despite the relatively short integration time (2070 s), the source was detected at a very high confidence level (~210σ), suggesting that it was bright. During this and subsequent observing sessions, the source 2S0114+650 was within the telescope field of view; this source is located one and a half degrees from the pulsar 4U0115+634 and, like the latter, is a member of a binary system with a massive optical companion—the Be star LSI+65°010 (see [18, 19]). No X-ray emission from this source was detected with the ART-P telescope (the 3σ upper limit on the 3–20-keV photon flux was 18 mCrab, as inferred from the sum of three sessions).

X-RAY VARIABILITY

Figure 2 (upper panel) shows the light curve of 4U0115+634 in the energy band 4–30 keV that was obtained during its observations with ART-P. The three groups of points correspond to different observing sessions, and each individual point represents the count-rate measurement during a single exposure (from 45 to 80 s in duration). The measurement was corrected for the background count rate and other instrumental effects (collimator transmission, misses due to dead time, etc.). We see from the figure that, apart from the monotonic, though fairly rapid (a factor of ~1.5 in four days) decrease in the source's intensity, its flux exhibited fairly large erratic variations on a characteristic time scale of several tens or even hundreds of seconds. In particular, several bursts of duration 300–500 s were detected on February 18, which occurred once every 1000–3000 s and during which the flux from the source increased by ~20–30%. Figure 3 shows the profiles of two such bursts with a high time resolution (the bin size was taken to be 7.2 s to remove the pulsation variability, where possible). The time intervals for these bursts near 18.5195 and 18.5604 UT are indicated in Fig. 2 by the vertical dotted lines. Note that X-ray bursts have also been previously observed in such pulsars as SMC X-1, LMC X-4, and Cen X-3 (see [20] and references therein). Note also that, despite the large variations in the source's intensity, its exposure-averaged "hardness" was essentially constant during the entire series of observations. This is confirmed by the lower panel in Fig. 2, which shows the ratio of count rates in the ART-P hard (18–30 keV) and soft (4–6 keV) energy bands. Only individual short bursts, during which the hardness slightly decreased (the lower panel in Fig. 3), may have constituted an exception. Having analyzed ten outbursts observed between 1969 and 1987, Whitlock *et al.* [7] previously concluded that the source's X-ray hardness was approximately constant.

According to data from the All-Sky Monitor (ASM) aboard the Ginga satellite, the 1–20-keV intensity of the source during the outburst under discussion was at a maximum on February 11 [8]. This implies that the ART-P observations were carried out on the descent of its X-ray light curve. Nevertheless, the source was still very bright. Table 1 gives the measurements of its flux (relative to the Crab photon flux) and luminosity (for an assumed distance of ≈3.5 kpc to the source; see [3]) for each of the three observing sessions.

SPECTRA

Apart from the emission properties characteristic of most X-ray pulsars, such as a power-law spectrum in the standard (2–10 keV) X-ray band, an exponential cutoff at high energies, and possible iron emission lines, the spectrum of 4U0115+634 exhibits two absorption features at energies ~12 and ~23 keV, which attracted particular attention to this source [11, 13]. These features are assumed to result from the resonance cyclotron scattering of X-ray emission by electrons in the neutron-star magnetic field. To analyze the ART-P spectroscopic data, we modified the standard empirical spectral model for X-ray pulsars proposed by White *et al.* [12] by including the absorption lines in it:

$$I(E) = I_0 E^{-\alpha} \exp[-L_1(E) - L_2(E)] \times \begin{cases} 1, & \text{if } E < E_c; \\ \exp[-(E - E_c)/E_f], & \text{if } E \geq E_c. \end{cases} \quad (1)$$

Here, the photon energy E is in keV, α is the photon index, and

$$L_i(E) = \tau_i \left(\frac{E}{E_i}\right)^2 \frac{W_i^2}{(E - E_i)^2 + W_i^2} \quad (2)$$

is the Lorentz function, which describes the profile of a cyclotron line with energy E_i, width W_i, and optical depth τ_i at the line center. A line with such a profile can be formed by scattering in an optically thin ($\tau_i \lesssim 1$), sufficiently cold ($kT_e \ll E_i$) magnetized plasma (see, e.g., [21]). The model disregards the interstellar absorption, because there was no appreciable distortion in the source's spectra measured with ART-P that could be attributed to absorption. In most cases, the possible [13] iron-line emission at 6.4–6.9 keV was also ignored. Only the February 19 spectrum, in which a

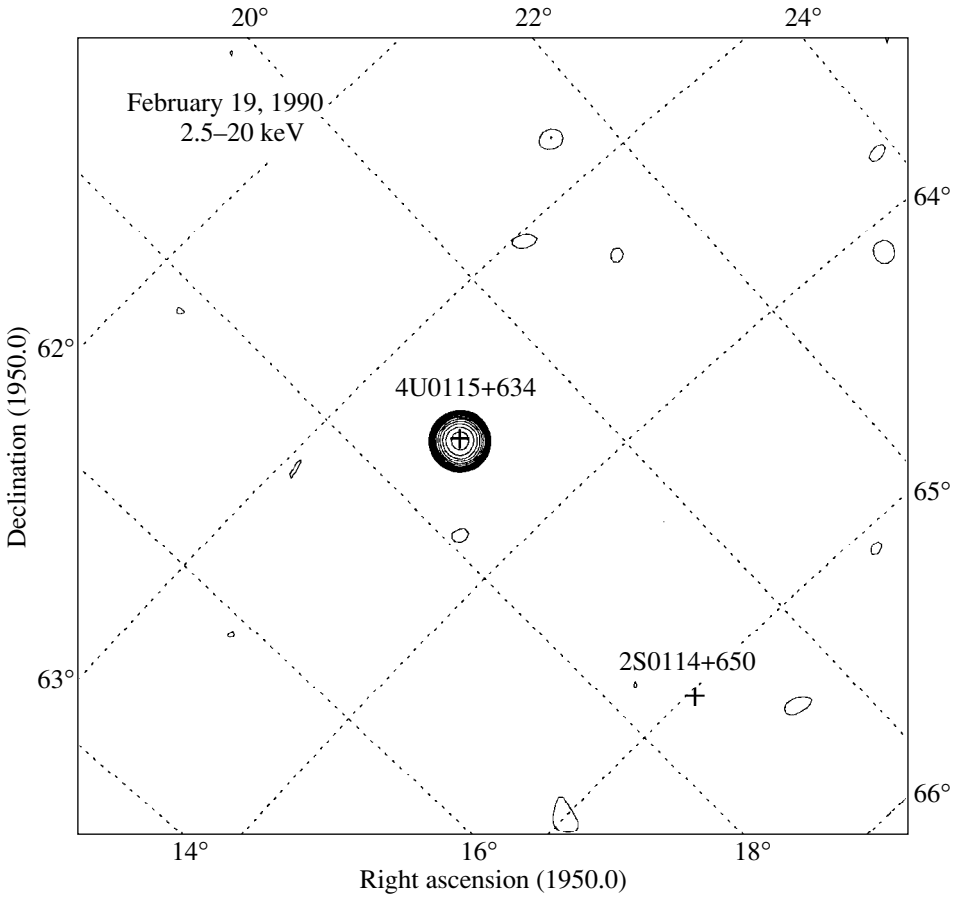

Fig. 1. The 2.5–20-keV image in the ART-P field of view obtained on February 19, 1990, when the transient pulsar 4U0115+634 was observed. The 3, 4, 5, 6.5, …, and 180σ confidence regions of the source detection (at logarithmic steps) are indicated by the contours.

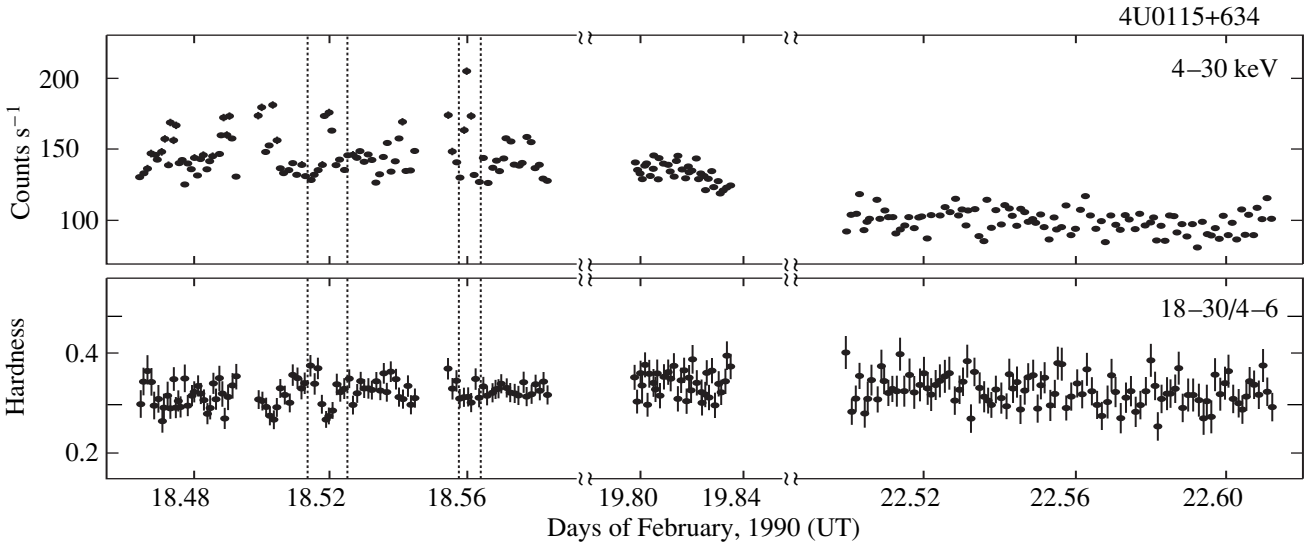

Fig. 2. The ART-P light curve of 4U0115+634 in the energy band 4–30 keV during the outburst in February 1990 (upper panel) and the corresponding variations in the source's hardness, the ratio of count rates in the hard (18–30 keV) and soft (4–6 keV) bands (lower panel). The vertical dotted lines indicate the time intervals for which Fig. 3 shows higher resolution light curves. The errors correspond to 1σ.

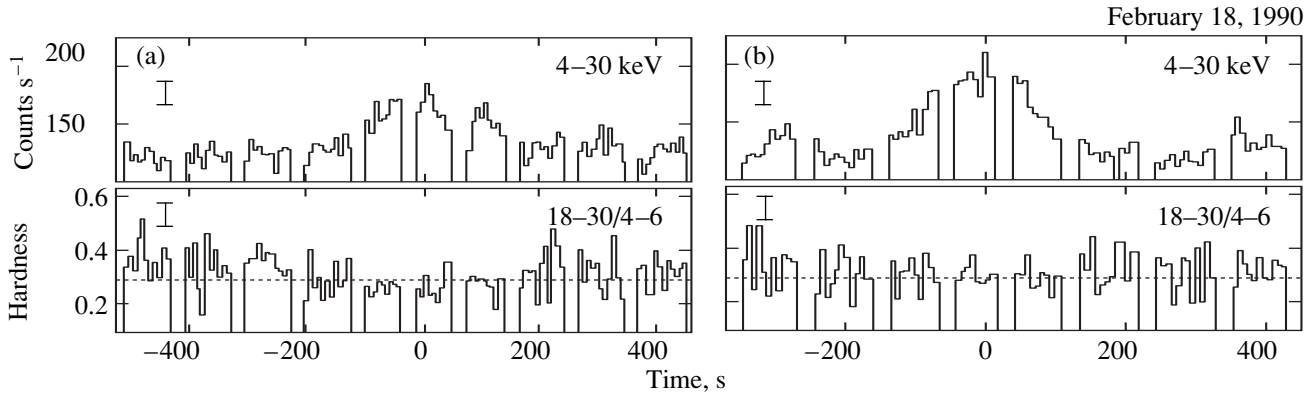

Fig. 3. The light curves of 4U0115+634 and its hardness curves as measured during X-ray bursts with a high time resolution [panels (a) and (b) were constructed for the intervals indicated in Fig. 2 by the dotted lines; the zero times correspond to February 18.5195 and 18.5604 UT].

narrow 6.4-keV line was detected at a moderately high confidence level (see below), constituted an exception.

The best-fit parameters [for the model (1)] for the source's spectra, as measured during the three observing sessions, are given in Table 2. We see that the photon index α and the exponential-cutoff energy E_c of the spectrum slightly changed from session to session, while the folding energy E_f, which characterizes the cutoff rate, was virtually constant. However, all the three measured spectra contained features (local breaks and irregularities) because of which their description by the simple model that ignored cyclotron-line absorption was not quite satisfactory (see the χ^2_N values in the table). Allowance for the absorption lines improved appreciably the fits to the spectra obtained on February 19 and especially on February 22. In the former case, we found only one line near energy ~11.5 keV, which corresponds to the first cyclotron harmonic, while in the second case, the absorption lines were observed both at the first ($E_1 \simeq 12.1$ keV) and second ($E_2 \simeq 22.2$ keV) harmonics. The absorption-line widths were assumed to be fixed and equal to $W_1 = 1.5$ keV and $W_2 = 2.0$ keV for the first and second harmonics, respectively. According to our analysis, this parameter could be measured using the ART-P data only with a large uncertainty (in particular, for the February 22 spectrum we obtained $W_1 \simeq 1.46 \pm 1.08$ keV and $W_2 \simeq 4.4 \pm 3.5$ keV, where the errors are given at a 1σ level).

In order to show how significant the decrease in χ^2_N is when one or two absorption lines are added to the model, in Table 3 we give an estimate of the probability that this decrease in χ^2_N occurred by chance for each specific case. The probabilities were calculated by using the $\Delta\chi^2$ statistics. We see from the table that, at least on February 22, the cyclotron absorption lines were detected in the spectrum of 4U0115+634 at a very high confidence level. The pulsar spectrum on this date is shown in Fig. 4a. The dots represent the pulse-height spectrum (in counts s^{-1} cm^{-2} keV^{-1}), and the solid line represents the corresponding model spectrum (in phot. s^{-1} cm^{-2} keV^{-1}) in which the cyclotron absorption at the fundamental and second harmonics was taken into account. For comparison, the dotted line indicates the model spectrum with the same parameters but without absorption lines. The deviations of the measured spectrum from the model spectra convolved with the instrumental response matrix are shown in Figs. 4b-4d in order of increasing complexity: without cyclotron lines, with one line, and with two lines.

When the February 19 spectrum of the source was fitted, in addition to the cyclotron absorption line at ~11.5 keV, it was necessary to include the emission line

Table 1. The photon flux and luminosity of 4U0115+634 in February 1990 as determined from ART-P data

Date (UT)	Orbital phase[a]	Photon flux, mCrab			L_X^b, 10^{37} erg s^{-1}
		3–6 keV	6–18 keV	18–30 keV	3–30 keV
18.464–18.584	0.951	460 ± 8	873 ± 9	802 ± 41	3.04 ± 0.03
19.798–19.835	0.004	393 ± 8	763 ± 9	792 ± 38	2.67 ± 0.05
22.503–22.612	0.117	304 ± 4	628 ± 5	577 ± 22	2.15 ± 0.02

[a] According to the ephemerides in Table 4.
[b] Assuming a distance of ≃3.5 kpc to the source.

Table 2. The best-fit parameters for the spectrum of 4U0115+634 as deduced from ART-P data[a]

Date	I_0	α	E_c	E_f	$I^b_{6.4}$	CL^c	$\chi^2_N(N)^d$
Feb. 18, 90	0.305 ± 0.060	0.454 ± 0.118	7.19 ± 0.52	8.57 ± 0.64			1.74(35)
Feb. 19, 90	0.208 ± 0.049	0.315 ± 0.148	6.54 ± 0.61	8.48 ± 0.81			1.95(35)
	0.282 ± 0.033	0.540 ± 0.064	9.85 ± 0.88	8.74 ± 0.81	2.89 ± 0.69	1	1.52(32)
Feb. 22, 90	0.164 ± 0.021	0.327 ± 0.078	7.20 ± 0.32	8.27 ± 0.39			2.26(35)
	0.142 ± 0.019	0.242 ± 0.080	7.33 ± 0.37	8.80 ± 0.51		2, 3	0.77(31)

[a] Based on the model (1): I_0 is the normalization of the power-law component (phot. cm^{-2} s^{-1} keV^{-1}), α is the photon index, E_c and E_f (keV) are the parameters of the exponential cutoff; all errors are at a 1σ level.

[b] The photon flux (10^{-2} phot. cm^{-2} s^{-1}) in the iron fluorescence line (the line energy and width were assumed to be 6.4 and 0.1 keV, respectively).

[c] The presence in the spectrum of a cyclotron resonance line with the following parameters: 1—E_1 = 11.45 ± 0.34 keV, τ_1 = 0.28 ± 0.12, W_1 = 1.5 keV (first harmonic); 2—E_1 = 12.10 ± 0.25 keV, τ_1 = 0.25 ± 0.04, W_1 = 1.5 keV (first harmonic); 3—E_2 = 22.24 ± 0.56 keV, τ_2 = 0.51 ± 0.13, W_2 = 2.0 keV (second harmonic).

[d] The χ^2 value is normalized to the number of degrees of freedom N.

with a Gaussian profile at a centroid energy of 6.39 ± 0.15 keV (Table 2). In the spectra of X-ray sources, this line usually results from the fluorescence of weakly ionized iron as the X-ray emission is reflected from the surface of a normal star, an accretion disk, or matter which flows over the neutron-star magnetosphere. The line was assumed to be spectrally narrow (σ = 0.1 keV, which is outside the ART-P resolution range), and its equivalent width was 282 ± 68 eV. During the observing sessions on February 18 and 22, this line was undetectable, and we were able to obtain only upper limits on its equivalent width at a 3σ level, 245 and 200 eV, respectively.

PULSE PROFILE

Having carried out three observing sessions in a row for the source near orbital phases 0.95, 0.00, and 0.12, we were able to determine the epoch of its periastron passage and refine the orbital period [22]. The parameters of the binary system 4U0115+634/V635 Cas that we used in the subsequent calculations are given in Table 4.

An analysis of the pulse profiles for the pulsar 4U0115+634 at different epochs and in different energy bands shows that their shape is virtually independent of orbital phase. To achieve a higher time resolution and to improve the statistics, we constructed the pulse profiles (see Fig. 5) averaged over all the three observing sessions in four energy bands (3–6, 6–12, 12–18, and 18–30 keV). The ratio of simultaneous flux to average (over the pulsation period) flux is plotted along the vertical axis. This allows us to keep track of the variations in pulse fraction when passing from one band to another. It is obvious that these variations are small. The pulse fraction, which is defined as $PF = (I_{max} - I_{min})/(I_{max} + I_{min})$, where I_{max} and I_{min} are the count rates at maximum and at minimum of the phase curve, respectively, properly corrected for the background and variations in the efficiency of the observations, was in the range 30–40%, and its mean in the band 3–30 keV was 36%.

In general, the ART-P observed pulse profiles had the shape characteristic of this pulsar: a strong, symmetric main peak at phases 0.1–0.45 and a weaker,

Table 3. Significance levels of the detection of cyclotron absorption lines in the spectrum of the pulsar 4U0115+634 with ART-P

Date	Spectral features	Significance level[a]	σ^b
Feb. 19, 90	Line at first harmonic[c]	2.2×10^{-4}	3.7
Feb. 22, 90	Line at first harmonic	8.6×10^{-9}	5.8
	Line at second harmonic[d]	1.2×10^{-4}	3.9
	Lines at both harmonics	2.8×10^{-11}	6.7

[a] The probability of a chance improvement in χ^2_N (see Table 2).

[b] In standard deviations of the normal distribution.

[c] The 6.4-keV iron line was simultaneously included in the model (Table 2).

[d] Relative to the model with one line at the first harmonic.

Table 4. Orbital parameters for 4U0115+634 and the pulsation period at the epoch of ART-P observations (TJD 940.965–945.113)[a]

$a_X \sin i^b$	140.13 ± 0.16 light seconds
P^c_{orb}	24.31643 ± 0.00007 days
e^b	0.3402 ± 0.0004
ω^b	$47^\circ.66 \pm 0^\circ.17$
τ^c	TJD 942.224 ± 0.004
P^c	3.61461 ± 0.00001 s

[a] $a_X \sin i$ is the projection of the orbital semimajor axis onto the plane of the sky, e is the eccentricity, ω is the periastron longitude, τ is the epoch of periastron passage, P_{orb} and P are the orbital and pulsation periods; TJD = JD–2447000.

[b] As inferred by Rappaport *et al.* [3].

[c] As inferred by Lutovinov *et al.* [22].

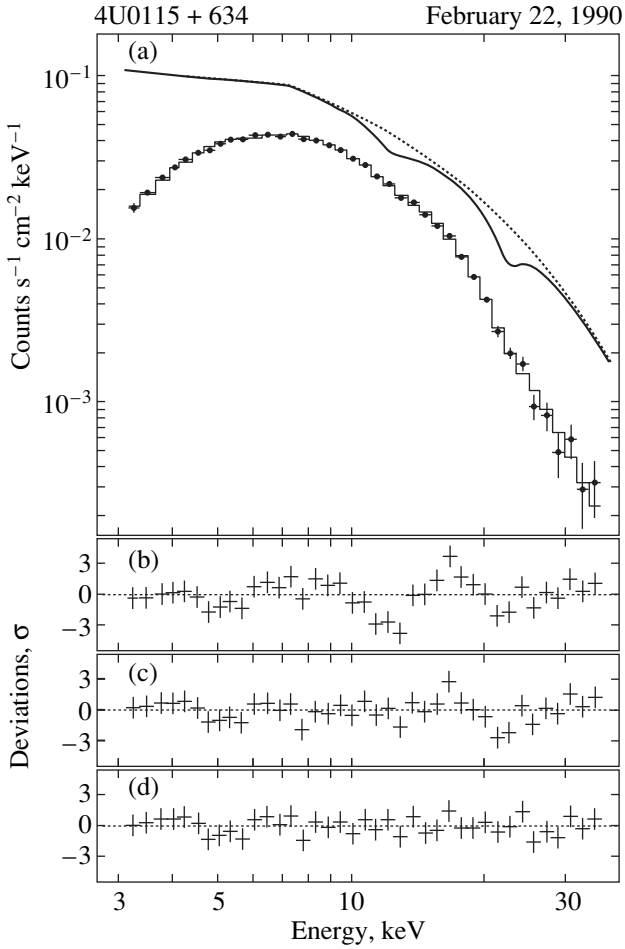

Fig. 4. The ART-P spectrum of 4U0115+634 on February 22, 1990 (panel a). The dots represent the measured (pulse-height) spectrum, and the histogram represents its best fit by the model (1) with allowance for cyclotron absorption at two harmonics. The model (photon) spectrum is indicated by the solid line. The dotted line represents the same spectrum but without absorption lines. Panels (b)–(d) show deviations of the experimental data (in σ) from the best fit for the three model spectra: without cyclotron absorption, with one line, and with two absorption lines, respectively.

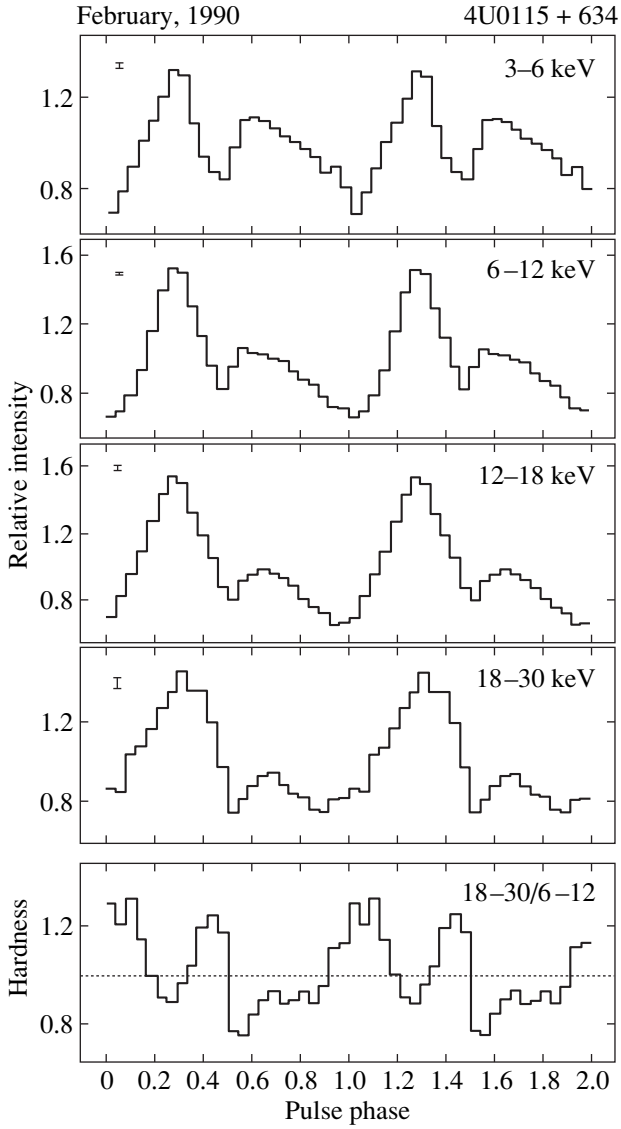

Fig. 5. Energy dependence of the pulse profile for the pulsar 4U0115+634, as derived from ART-P data. The ratio of instantaneous photon flux to average (over the period) flux is plotted along the vertical axis, which allows the change in pulse faction to be judged. The evolution of the source's hardness during the period is shown in the lower panel. The errors correspond to 1σ.

broad asymmetric second peak at phases 0.5–0.9. The width of the first peak increased, while the width and intensity of the second peak decreased with energy. This behavior of the phase curves was accompanied by changes in the source's hardness on a time scale of one pulsation period. This is clearly seen in the lower panel of Fig. 5, which shows the ratio of pulse profiles in the energy bands 18–30 and 6–12 keV.

PHASE-RESOLVED SPECTROSCOPY

To study the changes in the source's spectrum on a time scale of one pulsation period in more detail, we performed its phase-resolved spectroscopy. The data of the third session (which are of greatest interest because of the presence in the source's spectrum of simultaneously two cyclotron absorption lines at this time) were divided into eight successive phase bins. This binning, which is a factor of 3 coarser than that used to construct the phase curves in Fig. 5, was chosen to improve the statistics. The arrival time of each photon was corrected for the motion of the Granat satellite and the Earth around the Sun and for the motion of the neutron star in the binary system. The integration time of the photon spectrum for each bin was ~790 s.

We analyzed the phase-resolved spectra by the method that was already used when studying the pulsar phase-averaged spectra: the model (1) either without cyclotron lines, or with one line, or with two lines was

used to fit the photon spectrum; in each step, the decision on the necessity of using a more complex model was taken on the basis of the $\Delta\chi^2$ test at a 5% significance level. In other words, if the probability that the improvement of χ^2_N for a more complex model did not occur by chance exceeded 95%, then this (or an even more complex) model was used. The results of our analysis are shown in Fig. 6 in the form of plots of the spectral parameters against pulse phase. Note that the source's spectrum exhibits a statistically significant cutoff at high energies over the entire pulsation period, while the absorption lines appear only at certain phases. The energies of the line centers shift with phase; the ratio of energies of the first and second harmonics $H = E_2/E_1$ is not constant. H has the lowest value of $\simeq 1.65$ on the ascent of the main peak in the pulse profile and reaches $H \simeq 1.85$ on its descent and $H \simeq 2.05$ at the beginning of the second peak. Averaging over the phase bins during which both lines were observed yielded $H \simeq 1.79 \pm 0.08$. At the same time, the ratio of energies of these lines in the phase-averaged spectrum of the source was 1.84 ± 0.06 (Table 2).

We see from Fig. 6 that the phase variations in the source's hardness, which was previously defined as the ratio of count rates in the bands 18–30 and 6–12 keV, correlate strongly with the appearance in its spectrum of cyclotron absorption lines and with the variations in their energy. The pattern of variations in photon index α is completely different and must clearly affect the spectral hardness in the softer ($E \lesssim 6$ keV) energy band. In particular, it follows from the figure that the spectral slope in the soft band is positive (i.e., the photon flux density increases with energy) near the maximum of the main peak.

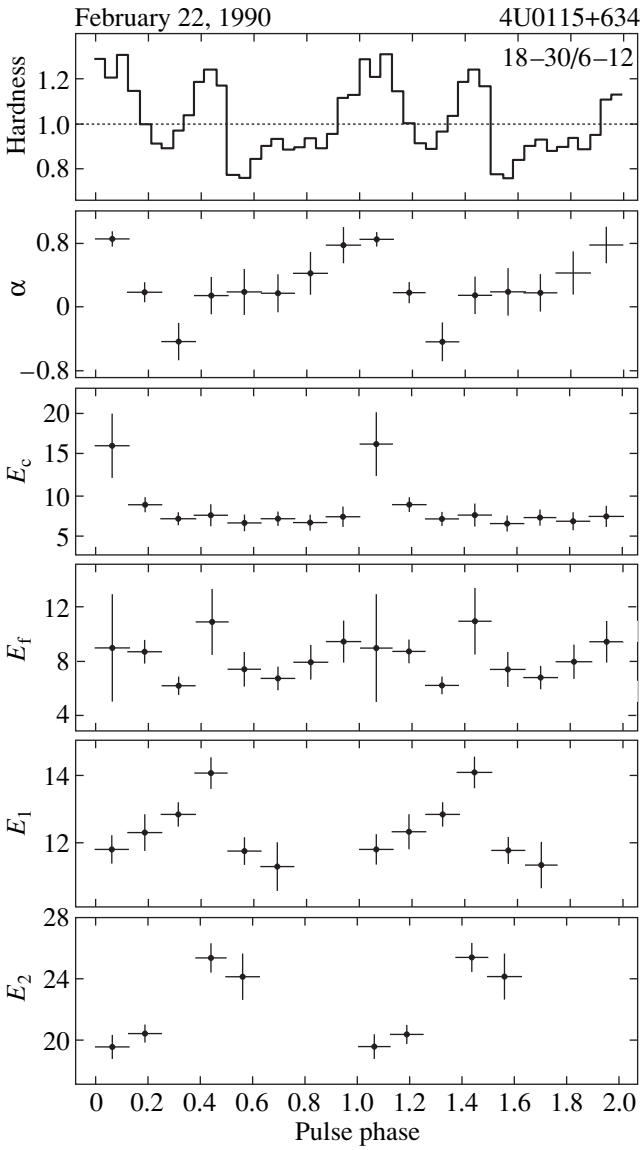

Fig. 6. Spectral parameters of 4U0115+634 versus pulse phase. Here, α is the photon index, E_c and E_f are the parameters of the exponential cutoff in the spectrum, and E_1 and E_2 are the centroid energies of the cyclotron absorption lines which correspond to the two harmonics. For comparison, the upper panel shows a plot of hardness versus pulse phase.

DISCUSSION

We have already mentioned above that X-ray outbursts of 4U0115+634, during which it shows up as an X-ray pulsar, occur approximately once every three years. In complete agreement with this assertion, the CGRO Observatory has recently (in March 1999) detected another outburst of the source [23]. All outbursts can be divided into two groups: strong (giant) and weak; the latter normally occur only near orbital phase 0.55 [7]. The outburst in February 1990, during which the source was observed with the ART-P telescope, belonged to the group of very strong outbursts.

An analysis of the source's X-ray light curve shows that, apart from the general trend in its intensity, its flux exhibited significant variations on time scales from several tens to hundreds and thousands of seconds. In particular, the ART-P telescope detected several short bursts of duration 300–500 s in February 18. The exposure-averaged hardness of the source was essentially constant during the entire series of observations.

The ART-P photon spectrum of the source revealed absorption features at energies $E_1 \simeq 12.1$ keV and $E_2 \simeq 22.2$ keV, which are most likely attributable to the resonance scattering of its emission at the first and second cyclotron harmonics. In this case, the magnetic-field strength on the neutron-star surface is

$$B \simeq 8.6 \times 10^{10} \left(\frac{E_1}{1\,\mathrm{keV}}\right)\left(1 - \frac{2GM}{Rc^2}\right)^{-1/2} \mathrm{G} \simeq 1.3 \times 10^{12}\,\mathrm{G}. \quad (3)$$

Here, we took into account the gravitational redshift of the neutron star by assuming that its radius and mass were $R = 12$ km and $M = 1.4M_\odot$, respectively.

The ratio of cyclotron-line energies $H = E_2/E_1 \simeq 1.8$ differs from $H = 2$ suggested by the harmonic ratio. Moreover, this ratio changes appreciably with line energy on a time scale of one pulsation period. Tamura *et al.* [8] explained the similar results that they obtained when studying 4U0115+634 from the Ginga satellite by the fact that the lines originated in regions with different magnetic fields, for example, those at different heights above the neutron-star surface. This explanation is corroborated by almost a factor of 2 difference in the optical depths, as measured for the first and second harmonics with the ART-P telescope (Table 2). However, two-photon scattering and emission, which, according to Alexander and Meszaros [24], are capable of increasing the depth of the second and higher harmonics in the source's spectrum compared to the depth of the fundamental harmonic, could contribute to this result. In conclusion, note that an appreciable deviation from the harmonic law has recently been also found for the third harmonic which was detected in the spectrum of this pulsar by the RXTE satellite [14].

ACKNOWLEDGMENTS

This study was supported by the Russian Foundation for Basic Research (project nos. 98-02-17056 and 99-02-18178) and the INTAS (grant no. 93-3364-ext). We wish to thank K.G. Sukhanov, flight director, the staffs of the Lavochkin Research and Production Center, RNIIKP, and the Deep Space Communications Center in Evpatoria, the Evpatoria team of the Space Research Institute (Russian Academy of Sciences), the team of I.D. Tserenin, and B.S. Novikov, S.V. Blagiĭ, A.N. Bogomolov, V.I. Evgenov, N.G. Khavenson, and A.V. D'yachkov from the Space Research Institute who operated the Granat Observatory, provided the scientific planning of the mission, and performed a preliminary reduction of telemetry data. We also wish to thank the team of M.N. Pavlinskiĭ (Space Research Institute) and the staff of the former Research and Development Center of the Space Research Institute in Bishkek who designed and manufactured the ART-P telescope.

REFERENCES

1. W. Forman, C. Jones, and H. Tanabaum, Astrophys. J. **206**, L29 (1976).
2. L. R. Cominsky, G. W. Clark, F. Li, *et al.*, Nature **273**, 367 (1978).
3. S. Rappaport, G. W. Clark, L. R. Cominsky, *et al.*, Astrophys. J. **224**, L1 (1978).
4. S. J. Unger, P. Roche, I. Negueruela, *et al.*, Astron. Astrophys. **336**, 960 (1998).
5. G. A. Kriss, L. R. Cominsky, R. A. Remillard, *et al.*, Astrophys. J. **266**, 806 (1983).
6. H. Tsunemi and S. Kitamoto, Astrophys. J. **334**, L21 (1988).
7. L. Whitlock, D. Roussel-Dupre, and W. Priedhorsky, Astrophys. J. **338**, 381 (1989).
8. K. Tamura, H. Tsunemi, S. Kitamoto, *et al.*, Astrophys. J. **389**, 676 (1992).
9. H. Mendelson and T. Mazeh, Mon. Not. R. Astron. Soc. **250**, 373 (1991).
10. I. Negueruela, J. E. Grove, M. J. Coe, *et al.*, Astron. Astrophys. **284**, 859 (1997).
11. W. A. Wheaton, J. P. Doty, F. A. Primini, *et al.*, Nature **282**, 240 (1979).
12. N. White, J. Swank, and S. Holt, Astrophys. J. **270**, 711 (1983).
13. F. Nagase, T. Dotani, Y. Tanaka, *et al.*, Astrophys. J. **375**, L49 (1991).
14. W. A. Heindl, W. Coburn, D. E. Gruber, *et al.*, astro-ph 9904222.
15. V. V. Borkus, Candidate's Dissertation (Moscow, 1998).
16. F. Makino, IAU Circ. No. 4967 (1990).
17. R. A. Sunyaev, S. I. Babichenko, D. A. Goganov, *et al.*, Adv. Space Res. **10** (2), 233 (1990).
18. G. Koenigsberger, J. H. Swank, A. E. Szymkowiak, *et al.*, Astrophys. J. **268**, 782 (1983).
19. S. Yamauchi, I. Asaoka, M. Kawada, *et al.*, Publ. Astron. Soc. Jpn. **42**, L53 (1990).
20. A. A. Lutovinov, S. A. Grebenev, and R. A. Sunyaev, Pis'ma Astron. Zh. **25**, 83 (1999) [Astron. Lett. **25**, 59 (1999)].
21. V. V. Zheleznyakov, *Radiation in Astrophysical Plasmas* (Yanus-K, Moscow, 1997).
22. A. A. Lutovinov, S. A. Grebenev, R. A. Sunyaev, *et al.*, Pis'ma Astron. Zh. **20**, 631 (1994) [Astron. Lett. **20**, 538 (1994)].
23. R. B. Wilson, B. A. Harmon, and M. H. Finger, IAU Circ. No. 7116 (1999).
24. S. G. Alexander and P. Meszaros, Astrophys. J. **372**, 565 (1991).

Translated by V. Astakhov

Astronomy Letters, Vol. 26, No. 1, 2000, pp. 22–33. Translated from Pis'ma v Astronomicheskiĭ Zhurnal, Vol. 26, No. 1, 2000, pp. 27–40.

Variability of Cyg X-1 (V1357 Cyg) in 1995–1996 during the Hard and Soft X-ray Spectral States

E. A. Karitskaya[1]*, V. P. Goranskiĭ[2], K. N. Grankin[3], and S. Yu. Mel'nikov[3]

[1] *Institute of Astronomy, Russian Academy of Sciences, Pyatnitskaya ul. 48, Moscow, 109017 Russia*
[2] *Sternberg Astronomical Institute, Universitetskiĭ pr. 13, Moscow, 119899 Russia*
[3] *Astronomical Institute, Academy of Sciences of Uzbekistan, Tashkent, Uzbekistan*

Received April 6, 1998; in final form, May 11, 1999

Abstract—We report photoelectric *UBVR* observations of Cyg X-1 with the 1-m Tien-Shan and 48-cm Mount Maidanak reflectors from October 1995 through November 1996. The orbital light curve is represented by the model of a tidally deformed star. Various types of flare and fading are observed. The optical and X-ray (ASM/RXTE 2–10 keV) variabilities are compared. A 90-day soft X-ray outburst occurred in the summer of 1996, but no similar event was detected at optical wavelengths. Nevertheless, an interrelation was found between the variabilities in these bands, suggesting that they are affected by the same processes. A correlation between changes in the mean X-ray and optical fluxes was found after the 90-day X-ray outburst and the mean optical orbital light curve were subtracted. A Fourier analysis reveals common features in Fourier spectra of the X-ray and optical data. An orbital X-ray variability with a 5.6% amplitude is confirmed. Optical flares with a $0^m.04$ amplitude and a duration of several days, which coincided with local X-ray minima, were detected. The optical brightness of Cyg X-1 declined by $0^m.04$ in about a week early in November 1996. A possible physical interpretation of the flares and the orbital X-ray variability in terms of accretion instability is offered. The characteristic time it takes for matter to pass through the accretion structure is estimated directly from observations; it was approximately a week in 1996. © *2000 MAIK "Nauka/Interperiodica".*

1. INTRODUCTION

One of the components of the X-ray binary system Cyg X-1 (V1357 Cyg) is a reliable black-hole candidate. Over the period of long-term optical photometric observations, the star has exhibited a mean orbital light curve typical of ellipsoidal variability with an amplitude of $0^m.048 \pm 0^m.003$ and a double-wave period of $5^d.6$ [1]. The light curve can be explained by tidal deformation of the optical star, an O9.7Iab supergiant, in the gravitational field of a relativistic component [2]. The relativistic component is surrounded by an accretion disk whose contribution to the system's total luminosity is a mere 4% [3].

The shape of the orbital optical light curve and the mean brightness vary with a 294^d period in phase with X-ray 3–6-keV variations [1, 4]. This phenomenon was interpreted by precession of the accretion disk in the direction of orbital motion [1], by contrast to the forced precession in Her X-1 and SS 433. Bochkarev and Karitskaya [5] and Karitskaya and Bochkarev [6] explained the "direct" precessional motion by the interaction of infalling matter with the disk. The theoretical curves obtained by Karitskaya [7] for a tilted, precessing starlight-scattering accretion disk describe well the changes in the light curves. Nevertheless, the 294^d period should be verified by currently available observations in various spectral ranges. Other periodicities were also detected by various authors: $39^d.2/78^d.4$ [8–10], $149^d.4$ and $53^d.3$ [11]. A periodicity analysis is complicated by the fact that the optical light variations are small (the OB star dominates) and that an irregular variability and flares are superimposed on the light curve.

In the X-ray 2–6-keV band, apart from a rapid millisecond variability and quasi-periodic oscillations, Cyg X-1 is characterized by transitions from the normal hard X-ray spectral state to the high soft state (outbursts) several tens of days in duration. In this case, the hard X-ray flux varies in antiphase with the soft X-ray flux, so the total flux is nearly constant [12]. One of such outbursts occurred in the summer of 1996 during our photometric observations.

Apart from the 294^d period, other periods were detected in the X-ray band. The ASM/RXTE data [12] revealed a 50^d periodicity in the recurrence of flaring episodes, which matches, within the error limits, the period found by Walker and Quintanilla [11] in the photometric *B* band. During the hard state of Cyg X-1, the ASM/RXTE and Ginga ASM data revealed an orbital modulation with a $5^d.6$ period [13].

Thus, there is presently ample evidence for a relation between the optical and X-ray variabilities, although the nature of these variations may be markedly different. Periodic variations with equal or close

* e-mail: karitsk@sai.msu.ru

periods are seen to be revealed in these two spectral ranges.

The nature of the distortions of the ellipsoidal optical light curve, their characteristic time scales, and the relation with X-ray events remain unclear so far in a number of cases. For example, during the June 1980 transition of Cyg X-1 to the soft state, Kemp *et al.* [14] detected a change in the shape of the optical orbital light curve. J.C. Kemp also surmised that some periodicities could arise during a transition of the X-ray source to the soft state. We therefore organized collaborative observations of Cyg X-1 at various observatories of the Commonwealth of Independent States as part of the International Program "Monitoring unique astrophysical objects" as soon as another transition of the source to the soft state occurred in May 1996. Here, we present the data obtained within the framework of this program at two observatories, which cover both states of Cyg X-1 fairly densely.

2. PHOTOMETRIC OBSERVATIONAL DATA

Observations

The observations at the Tien-Shan Astronomical Observatory in Kazakhstan (2730 m above sea level) were carried out with the 1-m reflector in October 1995 and October–November 1996. We used the four-channel *WBVR* photometer designed by Kornilov and Krylov [15]. This photometer works on the principle of spectrum separation by means of dichroic plates. The *WBVR* system was described in the catalog by Kornilov *et al.* [16], and the spectral sensitivity of the instrument in various photometric bands with and without filters was analyzed in detail by Kornilov [17]. The bands of the Tian-Shan *BVR* system (with filters) are close to the corresponding Morgan–Johnson bands. The instrumental ultraviolet *u* band was realized without filters and differs markedly from the standard; its equivalent wavelength is redshifted from the Morgan–Johnson *U* band [17]. The *u* observations were reduced to the simultaneously performed Mount Maidanak *U* observations. This reduction is proper only if there are no color variations and is suitable for studying the orbital light curve of Cyg X-1. We kept track of the object for a long time during each observing night at Tien-Shan, so it frequently sunk to the position corresponding to the air mass $M(z) = 3$ atm.

The observations at the Mount Maidanak Astronomical Observatory in Uzbekistan (2600 m above sea level) were carried out with the 48-cm reflector from June through November 1996. We used a standard single-channel *UBVR* photometer, which reproduced the Morgan–Johnson system. The object was observed two or three times near the meridian on each night and continuously at JD 2450377.

We obtained a total of 827 observations in three or four spectral bands during 115 nights in 1995–1996. Of them, 102 nights fell within the period of ASM/RXTE X-ray observations.

Comparison Stars

Apart from V1357 Cyg, we performed simultaneous observations of two more stars at the Tien-Shan Observatory in 1995: **a** (BD+34°3816, V1674 Cyg) and **c** (BD+34°3812) [18]. The coordinates, magnitudes, and colors of all the observed objects are given in Table 1. We confirmed the variability of V1674 Cyg discovered by Walker and Quintanilla [11] and have additionally used HD 189474 (no. 1, BD+35°3895, Sp A1V) (Table 1) as a comparison star since 1996. We published a special study of V16374 Cyg in [19].

The Mount Maidanak observations in 1996 were carried out with two comparison stars: BD+40°4147 (HD 229196, NSV 25130, Sp O5) and **c** (BD+34°3812); the latter was also used at Tien-Shan. It subsequently emerged that the former star was known as a double-lined spectroscopic binary and was suspected to be variable by Hill *et al.* [20]; it has now been included in the Supplement to the NSV catalog. We detected a $1^{d}.911$ periodicity of this star in the Fourier spectra of Cyg X-1 and BD+34°3812 with amplitudes of $0^{m}.051$, $0^{m}.054$, $0^{m}.043$, and $0^{m}.041$ in *U*, *B*, *V*, and *R*, respectively. The period was confirmed by Hill *et al.*'s observations and by Hipparcos photometric observations. Based on all observations at JD 2441158–2450755, we determined the elements:

$$\mathrm{Max} = 2450660.30(\pm.06) + 1^{d}.91079(\pm00003) \times E.$$

The light curve has a Cepheid-like shape. The star BD+40°4147 lies near the open cluster NGC 6910 but is probably not its member, as follows from the color-magnitude diagram [21]. The strict periodicity of the comparison star allows the Mount Maidanak observations of Cyg X-1 to be corrected, after which the dispersion of the light curve for Cyg X-1 approaches the dispersion of the mean Tien-Shan light curve.

Peculiarities of the Data Reduction Procedure

The Tien-Shan measurements were reduced by using the standard procedure of correction for the atmosphere with the nightly mean extinction coefficient in each photometric band determined by the Bouguer method. The comparison star HD 189474 and Cyg X-1 have different spectral energy distributions and different colors (Table 1). As might be expected, having reduced the data, we found a correlation between the magnitude of Cyg X-1 and the air mass, the Forbes effect (see, e.g., [22]), in all bands. To allow for the Forbes effect, we took a linear relationship between the star's magnitudes and the air mass. The orbital wave and the other periodicities were first subtracted from the magnitudes. The coefficients of the relationship

Table 1. Coordinates and magnitudes of the observed stars

Star	BD/GCVS	α 2000	δ 2000	*V*	*U–B*	*B–V*	*V–R*	Note**
a	V1674 Cyg	$19^h58^m21^s.7$	+35°13′00″	10.026	–	0.566	0.510	[T]
c	+34 : 3812	19 58 06.3	+35 22 47	9.082	−0.013	−0.029	0.024	[M]
				9.085	–	0.010	0.001	[T]
1	+35 : 3895	19 58 51.6	+35 29 52	6.998	+0.051*	0.040	0.031	[K]
	+40 : 4147	20 23 10.9	+40 52 30	8.498	−0.211	0.935	0.631	[M]
var	V1357 Cyg	19 58 21.7	+35 12 06	8.866	−0.279	0.842	0.871	[M]
				8.883	–	0.896	0.833	[T]

* *W–B* are given.

** The table gives the following photometric data: [T] averaged over all Tien-Shan observations; [M] from the Mount Maidanak observations; [K] from the catalog by Kornilov *et al*. [16].

were calculated by the least-squares method. The maximum coefficient in *B* was $-0^m.0124$ per atmosphere. These coefficients were used to correct the original observational data for the Forbes effect. This procedure resulted in the disappearance of all trends (gradual brightenings of the object during the night as it sunk), which are particularly pronounced in the short-wavelength *u* and *B* bands) in the light curves of Cyg X-1.

The mean extinction coefficients as determined by the Bouguer method in *u*, *B*, *V*, and *R* were, respectively, $0^m.304$, $0^m.202$, $0^m.126$, and $0^m.066$ in the fall of 1997. The accuracy of our Tien-Shan observations varied in the range $0^m.003$–$0^m.006$ on different nights.

The Mount Maidanak observations revealed no relationship between the magnitude and the air mass. After reducing the instrumental magnitudes to the standard ones, we found small systematic differences between the Tien-Shan and Mount Maidanak data (see Table 1). The corrections for the differences between the Tien-Shan and Mount Maidanak series were determined from simultaneous observations and from the levels averaged over the observing period. They were used to reduce the Tien-Shan *BVR* magnitudes to the Mount Maidanak photometric *BVR* system. The nightly mean photoelectric *UBVR* observations after all the previously described reductions are given in Table 2 (in electronic form).* Column 2 lists the Mount Maidanak *U* magnitudes and the Tien-Shan instrumental *u* magnitudes reduced to the *U* system by the method described above. Columns 6–9 give the rms deviations in *UBVR* on each night.

3. LIGHT CURVES OF Cyg X-1

The orbital *UBVR* light curves for 1995–1996 are shown in Fig. 1. We used the following elements:

$$\text{Min.Ihel.} = 2441561.22 + 5^d.599763(30)E. \quad (1)$$

The elements were refined by using two epochs of minima: GCVS IV and the current epoch derived from our data JD Min.Ihel = 2450364.05 ± 0.06 (the same result is obtained if the initial epoch from [1] is used instead of the GCVS initial epoch). The mean orbital light curve is well described by the model of a binary with a tidally distorted star. In Fig. 2a, the light curve is fitted with one of the model curves from [23] by the method described in [24]. The following model parameters were used in the calculations: the mass ratio $q = 0.25$, the Roche-lobe-filling coefficient $\mu = 0.9$, the gravitational-darkening coefficient $\beta = 1/4$, the orbital inclination $i = 45°$, and the limb-darkening coefficient $u = 0.4$. For comparison, Fig. 2b shows the light curve only for the soft X-ray state. No appreciable change in the curve shape is observed.

We analyzed our data together with the ASM/RXTE X-ray 2–10-keV data (http://space.mit.edu/XTE, May 1997). The nightly mean X-ray and optical (*B*) measurements are shown in Fig. 3. The X-ray data are presented on a logarithmic magnitude scale (Fig. 3a). The dispersion of the observations does not depend on whether the object is in the high or low state, which allows all data to be reduced simultaneously. The errors in the daily mean X-ray data do not exceed the point size in the figure. Individual several-day long X-ray episodes and the main 90-day double-peaked outburst, which corresponds to the high soft X-ray state, are seen during JD 2450220–50310 [13, 25]. The optical *B* data are shown in the form of deviations from the mean orbital light curve, a double wave (Fig. 3d). Figures 3b and 3c show the mean X-ray and optical light curves constructed by the method of moving average for a smoothing interval of 17^d at steps of $3^d.4$; the rms errors in the means are given in the figures. The mean optical light curve in Fig. 3c is indicated in Fig. 3d by the polygonal line. When computing the average X-ray light curve (Fig. 3b), we first subtracted the outburst, whose curve is indicated in Fig. 3a by the solid line, from the X-ray data.

It follows from Figs. 3a and 3c that the 90-day X-ray outburst had no effect on the mean optical light variations. However, after this outburst was subtracted, a comparison of the mean light curves in Figs. 3b and 3c

* Table 2 is published in electronic form only and is accessible via ftp cdsarc.u-strasbg.fr/pub/cats/J (130.79.128.5) or http://cdsweb.u-strasbg.fr/pub/cats/J.

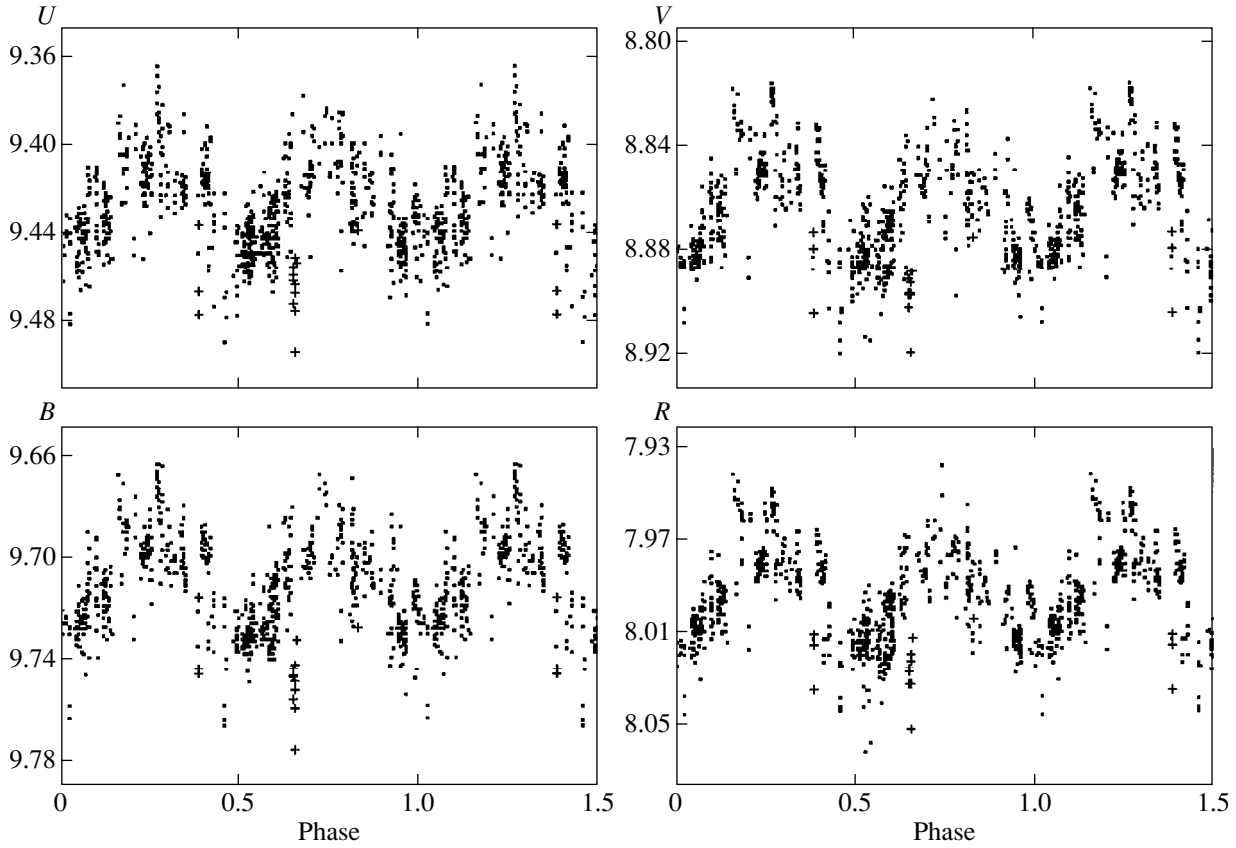

Fig. 1. Orbital light curves of Cyg X-1 in four bands with all individual measurements in 1995–1996. The crosses represent the observations during the week-long profound brightness decline in November 1996.

reveals optical variations on a characteristic time scale of several days, which follow the corresponding X-ray variations with a small shift in time. The mean optical brightness was $0^m.014$ lower at the minimum corresponding to the dip between the two peaks of the main X-ray outburst and reached a normal value by the end of the high state, passing through the maximum corresponding to the second peak of X-ray emission. After the 90-day X-ray outburst, the fluctuations in mean brightness continued with the same amplitude. The features of the optical light curve precede the features of the X-ray light curve by approximately a week. The correlation analysis in Sect. 4 confirms this qualitative conclusion. An explanation of this delay is offered in Sect. 6.

The large scatter of points about the mean smooth light curve in Fig. 3d can be explained by the two types of variability that we detected in V1357 Cyg in 1996. For clarity, two segments of the light curve are shown in Fig. 4 on an enlarged scale.

We detected intense flares with a $0^m.03$-$0^m.04$ amplitude, which is comparable to the peak-to-peak amplitude of the orbital variability, and a duration of several days. Local X-ray fadings correspond to these flares. Two flares of $0^m.04$ amplitude which lasted for several days with its maxima at JD 2450267 (July 2) (Fig. 4a) and JD 2450366 (October 9) are most characteristic. They were accompanied by 20% local X-ray fadings.

Apart from intense long flares, the light curve exhibits relatively short flares (with an amplitude up to $0^m.025$) of the order of several hours in duration. They are generally accompanied by small increases in X-ray fluxes by $0^m.1$–$0^m.2$. One of such flares was observed on October 21, 1995, as a rise in the stellar flux above the level of the ellipsoidal light curve followed by a rapid decline during the night. The flare amplitude and frequency do not depend on orbital phase.

Individual optical fadings (up to $0^m.01$) commonly coincide with local X-ray minima.

Early in November 1996, we observed an unusually profound fading of Cyg X-1 by $0^m.04$ simultaneously in all the four spectral bands, which lasted for about a week (JD 2450390–2450397) [26] (crosses in Fig. 1). The object's mean brightness at a phase close to elongation is seen to have dropped below the level of the secondary minimum. The fading amplitude was equal to the accretion-disk contribution to the system's total flux that was previously estimated by Bruevich *et al.* [3]. This brightness decline occurred between two soft

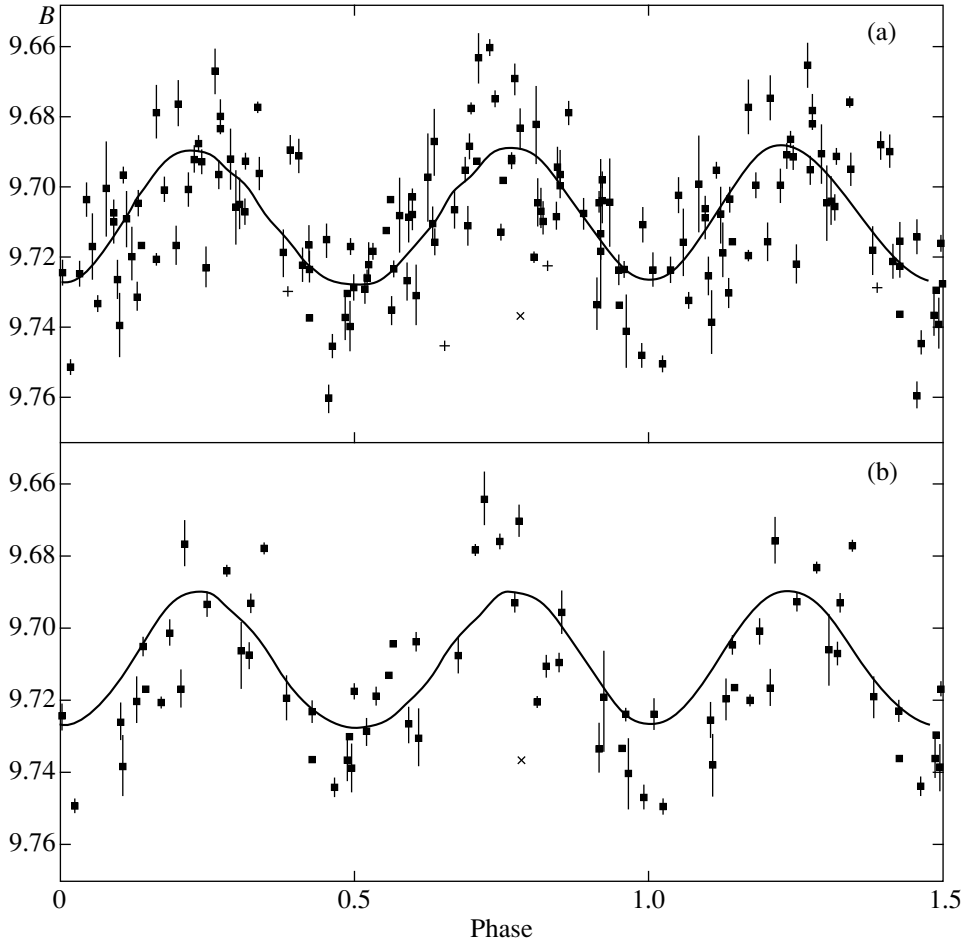

Fig. 2. Orbital *B* light curves of Cyg X-1 with nightly mean points obtained (a) over the entire period of observations 1995–1996 and (b) only during the soft X-ray state. The rms deviation is shown for each night. The solid line represents the theoretical light curve calculated in the model of a tidally deformed OB star. The crosses indicate the data during the profound brightness declines at JD 2450256 and JD 2450390–2450397.

X-ray flaring episodes and approximately coincides in time with a local 20% decline in X-ray flux (Fig. 4b). Another, shorter decline of the same amplitude was detected at JD 2450257.

We conclude that, irrespective of global X-ray changes, the optical orbital light curve retains its double-wave shape; it may be distorted by the previously described features at different phases. Our observations reveal no dependence of these distortions on orbital phase (Fig. 1). The scarcity of observational data in analyzing a flare at an arbitrary orbital phase may lead us to the erroneous conclusion that the shape of the optical orbital light curve changes during a transition to the soft X-ray state [27].

4. CORRELATION BETWEEN X-RAY AND OPTICAL VARIATIONS IN Cyg X-1

Since there is no optical event similar to the 90-day X-ray outburst and since there is no X-ray orbital variability similar to the optical variability, we calculated the cross-correlation functions between the X-ray data in the form of a residual series after the X-ray outburst was subtracted and the optical data in the form of residuals after the orbital light curve was subtracted. In this case, the results of the calculations could depend on the representation of the mean flux of the X-ray outburst on its descent. We therefore performed the calculations for various possible cases. It turned out that the conclusions did not change qualitatively.

The cross-correlation functions were calculated in the range of shifts τ from –30 to 30 days. There is no statistically significant correlation between the residual series. The cross-correlation function is at a maximum [$R_{xy}(\tau) = 0.29$] for the delay $\tau = 7^{d}$. Given the previously reached conclusions about the different types of Cyg X-1 variability on different time scales, one might expect the lack of a direct correlation between the X-ray and optical data. We therefore must separate, where possible, the variations on a particular time scale when studying correlations between the variations on different time scales, because the remaining types of vari-

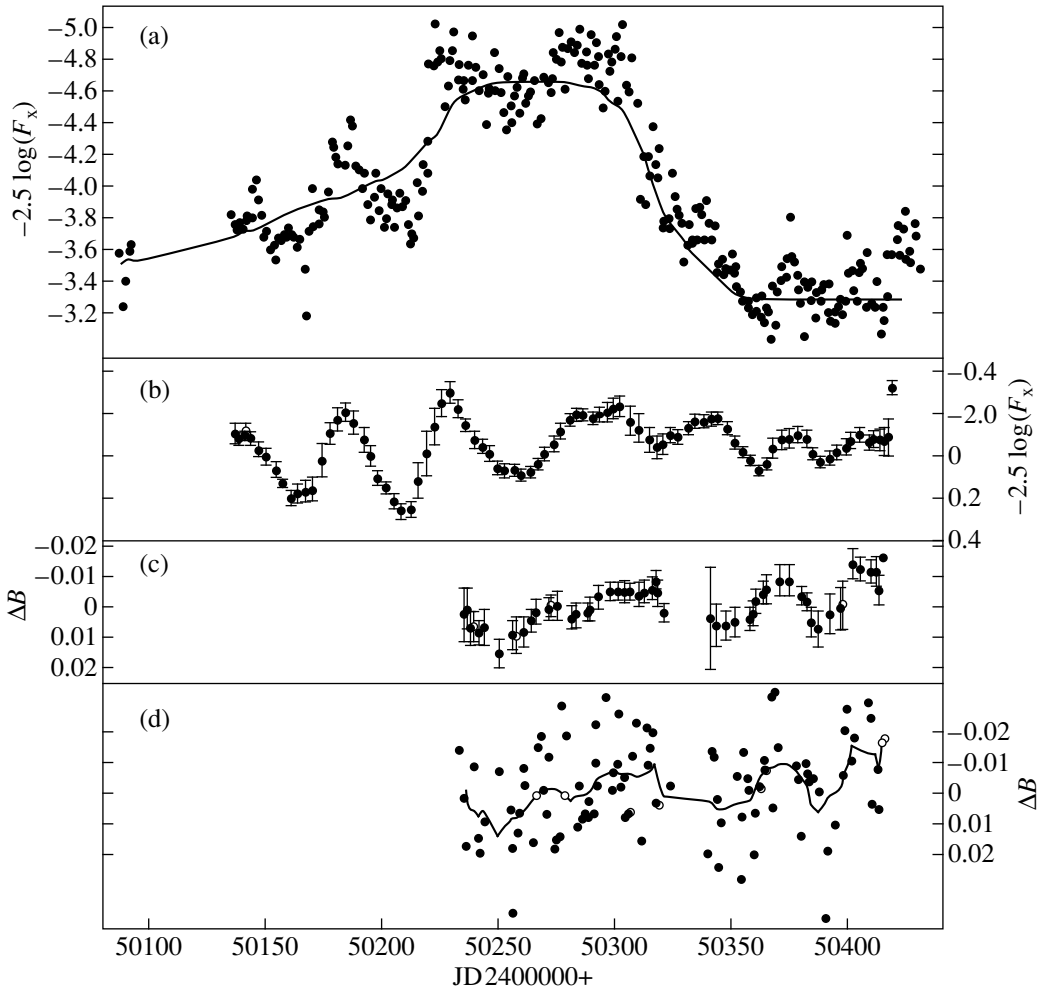

Fig. 3. Comparison of the X-ray and optical (*B*) light curves for 1996. Deviations from the mean smoothed orbital double wave are given. All data were averaged over the night. (a) The observed X-ray light curve; the solid line represents the light curve of the X-ray outburst. (b) The X-ray light curve after the X-ray outburst was subtracted smoothed by the method of moving average. (c) The optical light curve smoothed by the method of moving average. (d) The observed optical light curve; for comparison, curve (c) is indicated by the polygonal line.

ability distort the correlation function. For example, when the delays between rapid X-ray and optical variations on time scales of several days are analyzed, the slow trends on scales of tens and hundreds of days must be taken into account. By contrast, when the long-term variations are analyzed, the residual series must be smoothed; the method of moving average is suitable for this purpose.

The cross-correlation function of the smoothed (see Sect. 3) series (Figs. 3b and 3c) is shown in Fig. 5. Here, there is a correlation, $R_{xy}(\tau) = 0.63$, with the shift $\tau = 6^d$ at a confidence level higher than 95%. The smoothed series in other optical bands confirm the correlation of the mean levels with this shift with an even larger value of $R_{xy} = 0.71$ in *V*. To investigate the correlation in the rapid variations on a time scale of a day, we took into account the slow trends in the optical and X-ray light curves (by subtracting the smooth mean light curves). The cross-correlation function of these series revealed no peculiar features and it did not exceed 0.22 in absolute value, suggesting that there is no direct correlation between the rapid X-ray and optical variations; i.e., we cannot separate events of different types on this time scale. For example, in Sect. 3 we noted the existence of two types of flare, one is associated with simultaneous X-ray flares, while the other is associated with declines in X-ray flux.

Thus, we found a statistically significant correlation between the variations in the mean optical and X-ray fluxes (after the 90-day X-ray outburst was subtracted); the X-ray variations lag behind the optical variations by $6–7^d$.

5. FOURIER ANALYSIS OF THE X-RAY AND OPTICAL OBSERVATIONS

We performed a Fourier analysis of the *BVR* observations for 1995–1996 and the ASM/RXTE X-ray (2–

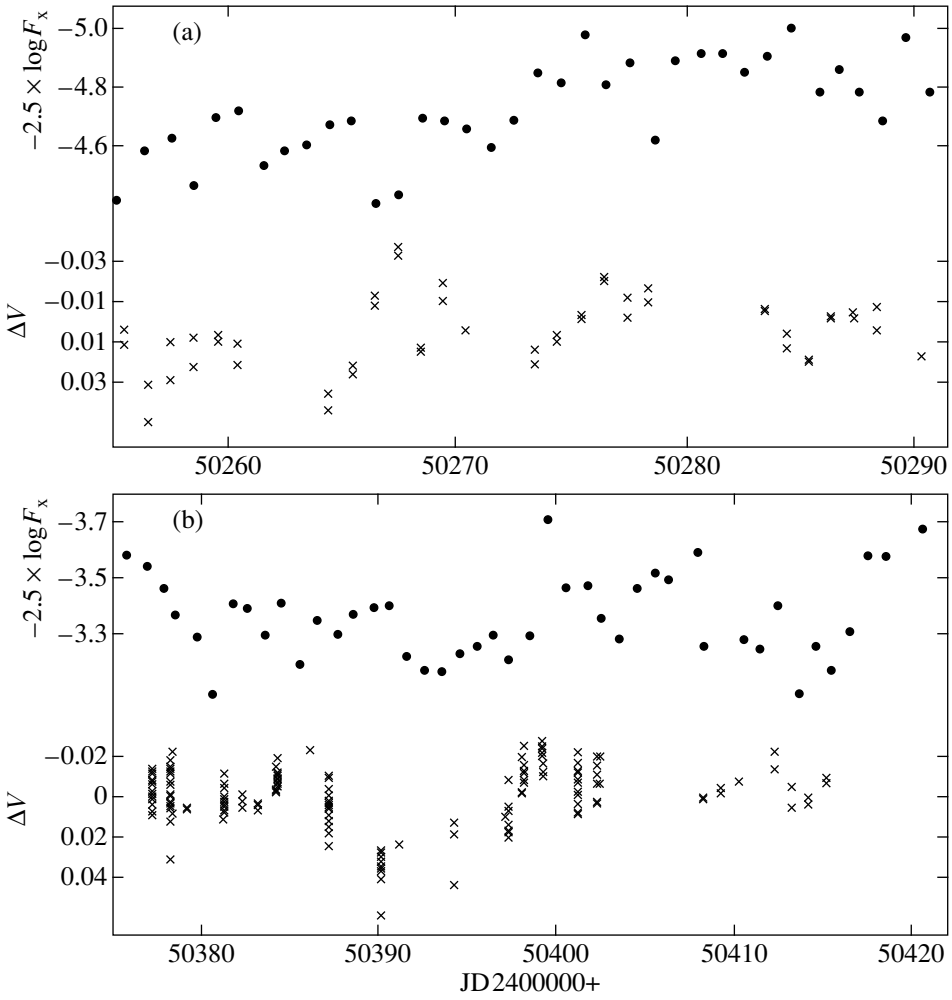

Fig. 4. Portions of the light curves on a scale that allows an examination of the largest optical flare in July 1996 at JD 2450267 (a) and the profound fading in November JD 2450390–2450397 (b). Individual points in *V* were used.

10 keV) data before JD 2450420 by using Deeming's method [28]. We subtracted the mean light curve of the 90-day outburst from the daily mean X-ray fluxes on a logarithmic scale and the average, smoothed double wave of the orbital period from the daily mean optical data. The Fourier spectra are shown in Fig. 6. The light curves were decomposed into Fourier components by sequentially subtracting the smoothed mean light curves of these components in order of decreasing amplitudes. This procedure was justified, in particular, by Terebizh [29] and was used, for example, by Goranskii *et al.* [30] to investigate SS 433. The fact that the rms deviation of the observations from the Fourier representation exponentially approaches the observational error as the number of involved components increases suggests that the above procedure is proper. The principal discrete components of the Fourier decomposition are summarized in Table 3, which shows the presence of the same (within the limits of the errors given in the last column) Fourier components for the X-ray band and the optical *BVR* bands. No results of the Fourier analysis are given for the *U* band, because the reduction of some of the UV observations to the standard band is improper (see Sect. 2), although they independently confirm the presence of the same components.

We estimated the confidence levels of the peaks in the power spectrum by numerically simulating a random series from the original series of observations by mixing the counts with the dates JD retained [29]. The only random value from the set of quantities was chosen in each series of observations for each JD. The synthetic random series had the same distributions of the quantities and dates as the original series. Our calculations of the Fourier spectra for $\sim 10^5$ realizations of random light curves yielded the dependence of the probability of a chance occurrence of a peak in the spectrum on its amplitude. The confidence levels calculated in this way are indicated in each spectrum of Fig. 6 and depend on the peak amplitude alone.

The Fourier spectrum in the X-ray band is dominated by a peak at 50^d (the period of flaring episodes

found by Zhang *et al.* [12] is ≈294^d/6!) and the accompanying local maximum at $37\overset{d}{.}7$. The confidence levels of these features in the spectrum exceed 99.99%. In our view, this structure of the main peak stems from the fact that the amplitude of the oscillations with the 50^d period changes over the period of observations.

In the optical band (*B, V*), this split structure is also observed at $50\overset{d}{.}0$ and $35\overset{d}{.}7$ at a 99% confidence level. The differences between the corresponding X-ray and optical periods do not exceed the errors of their determination. Remarkably, there are no optical observations before the outburst, when the X-ray oscillations with $P = 50^d$ had the largest amplitude; nevertheless, this period shows up in the optical band.

We cannot directly confirm the existence of $P = 294^d$ based on these data, because the series of observations under study is short. However, this previously determined period may show up in the observations as a period in the variations of the amplitude of X-ray oscillations after the outburst has been subtracted. Karitskaya [30] developed this interpretation, which is corroborated by the relationships between the observed frequencies: $f_{37.7} = f_{50} + 2f_{294}$; $f_{44.3} = f_{50} + f_{294}$; and $f_{63.2} = f_{50} - f_{294}$, as well as by Fig. 3 from the cited paper. This figure clearly shows a modulation of the amplitude of the $50\overset{d}{.}0$ oscillations with periods of 294^d and 147^d; six and three such oscillations fit into these periods, respectively.

The optical power spectrum (apart from the orbital period) is dominated by a pair of peaks at $16\overset{d}{.}8$ and $14\overset{d}{.}8$ at a 99.9–99.99% confidence level. Note that subtracting the orbital wave causes the confidence level of these peaks to increase, because the dispersion of the light curves decreases, and, hence, the probability of a random realization of the wave with this amplitude also decreases. The X-ray power spectrum exhibits a small peak at $16\overset{d}{.}4$ (≈50^d/3), but at higher frequencies, a wave with a $8\overset{d}{.}5$ period dominates.

Thus, despite the significant differences in the optical and X-ray Fourier spectra of Cyg X-1, they exhibit common features or multiple periods, which suggest a correlation between the variations in these bands.

In addition, a 96^d (≈294^d/3) period clearly shows up in the optical *B* band; it is also seen in other bands. At the same time, the peak at $P = 143\overset{d}{.}5$ (≈294^d/2), which is also traceable in other bands, is one of the largest peaks in the *V* band. Based on the *B* observations in 1972–1976, Walker and Quintanilla [11] also found close periods, $149\overset{d}{.}4$ and $53\overset{d}{.}3$.

Interestingly, the 39^d period found by Kemp *et al.* [8] and Karitskaya [9] probably matches, within the error limits, our period $P = 37\overset{d}{.}7$.

The peak of the orbital $5\overset{d}{.}6$ period is also seen in the Fourier spectrum of the RXTE data at a relatively low confidence level of 90.0%. Note that when the X-ray series is prewhitened for the low-frequency components whose periods are given in Table 3, the confidence level of this peak increases to 99.7%. (The Fourier spectrum of the optical data is known to be dominated by the peak with a $2\overset{d}{.}8$ period.)

Summarizing the results of the Fourier analysis, it should be noted that the presence of features at low frequencies probably does not reflect any physical, strictly periodic processes such, for example, as nonradial pulsations in multiperiodic variable stars. We considered the Fourier transformation of the light curve, a mathematical function specified for a limited number of values of the argument. After the orbital periodicity has been subtracted, the optical light curves are apparently nonperiodic. The better the synthetic light curve, which is the sum of discrete Fourier components, represents the actual light curve, the larger the number of such discrete components we take into account (inverse Fourier transform).

On the one hand, the presence of identical features in the X-ray and optical frequency spectra is possible only if the intervals of observations are close in length in different bands and if the time distributions of the observations (in both cases, these are daily means) are close and, hence, the spectral windows, the widths of discrete peaks, and the frequency resolutions are similar. On the other hand, this is only possible when the light curves in these two bands, while showing little similarity at first glance, nevertheless reflect some aspects of the same process, for example, mass transfer between the binary components (see Sect. 6). The Fourier analysis independently confirms the qualitative conclusion (see Sect. 3) about the correlation between the optical and X-ray variations after the main soft X-ray outburst and the optical orbital variability have been subtracted and the results of the cross-correlation analysis (see Sect. 4).

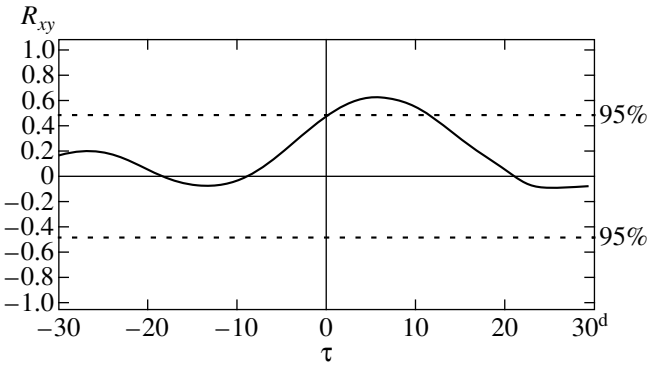

Fig. 5. Cross-correlation function between the smoothed X-ray (Fig. 3b) and smoothed optical (Fig. 3c) light curves.

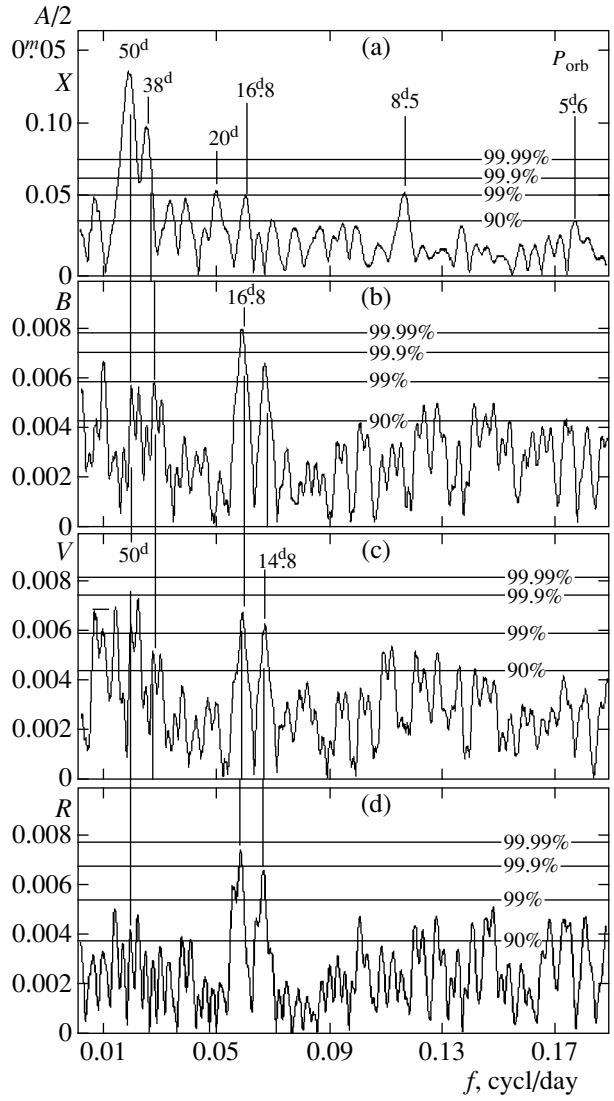

Fig. 6. (a) Fourier spectra of the X-ray data and (b–d) optical *B, V,* and *R* data in the range of periods 5–400^{d}.

Further simultaneous X-ray and optical observations could show how stable the discrete components found in the Fourier spectra are.

6. ORBITAL SOFT X-RAY VARIABILITY AND ITS POSSIBLE INTERPRETATION

Our Fourier analysis of the ASM/RXTE data confirms the existence of the X-ray orbital period discovered by Zhang *et al.* [13] (see Table 3). The mean harmonic amplitude of these variations over the entire time interval we studied is $0^{m}.056$ and close to the optical one, while the peak-to-peak amplitude is higher ($0^{m}.07$). However, by contrast to the ellipsoidal double wave in the X-ray band, the orbital period exhibits a single sine wave (the wave crest and trough turn out to be near phases $0^{p}.4$ and $0^{p}.9$, respectively). Figure 7a shows the X-ray orbital light curve of Cyg X-1 constructed over the entire period of observations under study, JD 2450087–2450422. We first subtracted the light curves of the main 90-day outburst, as well as the waves with periods of 50, 38, 44, 63, 130, 20, and 8.5 days and with amplitudes higher than $0^{m}.10$. For comparison, we also constructed the X-ray orbital light curves both during (Fig. 7b) and after (Fig. 7c) the 90-day outburst. It can be seen from the figure that the orbital variability persisted over the entire period of observations. This conclusion differs from the conclusion of Zhang *et al.* [13], who detected no orbital variability during the soft X-ray outburst, and this was incomprehensible in terms of their interpretation of the orbital X-ray variations by anisotropic photoelectric absorption of X-ray emission in the ambient gas. This discrepancy has now been removed. The discrepancy in the conclusions appears to be explained by the difference in the methods used: we removed all the known low-frequency components.

As follows from Fig. 7, the shape of the orbital X-ray light curve may have slightly changed with time. The light curve exhibited a broad minimum centered at phase $0^{p}.85$ and a narrow maximum at $0^{p}.35$ during the soft outburst and a narrow deep minimum at phase $0^{p}.0$ and a broad maximum at $0^{p}.5$ after the outburst. The change in the shape of the orbital light curve may be caused by a change in the distribution of the surrounding obscuring matter, for example, as the angular momentum of the infalling matter relative to the disk changes. Thus, the conclusion about a possible increase in the relative specific angular momentum of the infalling matter during the transition of Cyg X-1 to the soft state can apparently be drawn from the deduced variability of the shape of the X-ray orbital light curve. This would cause the accretion rate to increase and could be responsible for the transition to this state itself.

7. POSSIBLE INTERPRETATION OF OPTICAL FLARES

The activity that shows up in intense (for the optical variability of Cyg X-1) flares with a duration of several days can apparently be explained by irregular accretion of matter. An isolated portion of this matter interacts with the accretion structure to generate a shock wave, which gives rise to a gas clump whose thermal radiation produces an observable flare. A thickening similar to that proposed by Kemp [32] to explain the polarization variations in Cyg X-1 with orbital phase is formed at the rim of the accretion disk.

The flare of July 1–3, 1996, is most characteristic; the brightness on July 1 increased by about $0^{m}.03$ in all

Table 3. Components of the Fourier spectrum for the X-ray and optical light curves of Cyg X-1

No.	X ray		*B*		*V*		*R*		σ(*P*)
	P	Amplitude	*P*	Amplitude	*P*	Amplitude	*P*	Amplitude	
1	$51\overset{d}{.}1$	$0\overset{m}{.}26$	$49\overset{d}{.}9$	$0\overset{m}{.}011$	$50\overset{d}{.}0$	$0\overset{m}{.}012$	$49\overset{d}{.}9$	$0\overset{m}{.}008$	$\pm 2\overset{d}{.}5$
2	37.7	0.18	35.7	0.011	36.1(?)	0.010	35.8(?)	0.006	±1.3
3	44.3	0.14	44.0	0.011	44.2	0.015	44.2	0.009	±2.0
4	63.2	0.13	69.1(?)	0.006	68.5	0.014	68.5	0.010	±3.5
5	129.4	0.10	128.7(?)	0.009	131.9	0.014	128.9(?)	0.005	±15.0
6	20.0	0.10	–	–	20.1(?)	0.006	–	–	±0.4
7	8.53	0.10	–	–	8.3(?)	0.010	8.3(?)	0.009	±0.1
8	16.4	0.10	16.8	0.016	16.86	0.013	16.9	0.015	±0.3
9	14.3(?)	0.07	14.8	0.014	14.83	0.012	14.8	0.013	±0.2
10	5.61	0.06	2.8	0.04	2.8	0.04	2.8	0.04	±0.05
11	–	–	144.8(?)	0.008	143.5	0.014	143.5(?)	0.007	±19.0
12	–	–	96.0	0.013	102.2	0.012	95.9(?)	0.007	±8.4

bands. The absence of color variations in the star during the flare suggests that the gas was initially optically thick with a temperature $T_g \approx 2 \times 10^4$ K comparable to the supergiant's temperature. The flare luminosity at a distance of 2 kpc [33] was of the order of 9×10^{36} erg s^{-1}, which suggests a radius of the emitting region $R_g \approx 0.2R_* \approx 0.1a$ (R_* is the supergiant's radius, and a is the component separation). The gas then, during the expansion, became optically thin: On July 2, the brightness reached a maximum in V and R (amplitudes $\Delta V \approx \Delta R \approx 0\overset{m}{.}05$) and declined in B ($\Delta B \approx 0\overset{m}{.}027$).

For the interstellar absorption $A_V = 3\overset{m}{.}3$, $E(B–V) = A_V/3.2$ [34], and its standard wavelength dependence, we obtained the luminosity per unit frequency in *B*, *V*, and *R* at a distance of 2 kpc: 3.5×10^{21}, 5.4×10^{21}, and 6.1×10^{21} erg s^{-1} Hz^{-1} (the absolute calibration from [36] was used). These values are in good agreement with the thermal radiation of an optically thin gas with $T_g = 2 \times 10^4$ K and the volume emission measure $ME_V = 2 \times 10^{61}$ cm^{-3}. The total luminosity is 5.3×10^{36} erg s^{-1}. The emission was apparently at a maximum during an unobservable part of the day.

The gas clump was mainly heated by the ultraviolet radiation from the supergiant, $L_* \approx 10^{39}$ erg s^{-1}, by the X-ray radiation from the neighborhood of the black hole, $L_x \approx 2 \times 10^{37}$ erg s^{-1}, and by the conversion of kinetic energy into thermal energy as the infalling matter interacted with the accretion structure. A constraint on the optical depth for Thomson scattering and for free-free absorption yields an estimate of the electron density, $N_e \le 3 \times 10^{12}$ cm^{-3}. It appears that $N_e \ge 10^{13}$ cm^{-3}, $R_g \approx 0.1a$ on July 1 and $N_e \approx 2 \times 10^{12}$ cm^{-3}, $R_g \approx 0.15a \approx 4 \times 10^{11}$ cm on July 2. Since the flare lifetime exceeds appreciably the hydrodynamic time (several hours), it took a long time, at least two days, for the mass transfer through the shock that formed the gas clump. In this case, part of the matter disperses into space. We observed a simultaneous 20% fading in the X-ray 2–10-keV band, which can be explained by an increase in the photoelectric absorption in the additional matter along the line of sight with $N_H = 3.6 \times 10^{22}$ cm^{-2}.

The additional portion of the accreted matter responsible for the flare must increase the X-ray flux in the characteristic passage time of the matter through the disk. Indeed, the soft X-ray flux increased in seven days (see Fig. 4a). Interestingly, this time matches the delay between X-ray features in the light curve with a duration of several tens of days and similar features in the mean optical light curve (Sects. 3 and 4). The rise in the X-ray and optical fluxes appears to be caused by the pumping of matter in isolated portions into the accretion structure whose outer part is responsible for the optical emission and whose inner part, which is responsible for the X-ray emission, is replenished in the characteristic passage time of the matter through the disk (of the order of a week).

By contrast to the May 14/15, 1997 flare [35] attributable to the Balmer-line and Balmer-continuum emission, a longer mass transfer, a higher gas density, and a more compact stable emitting region were observed during the 1996 flare.

It would be natural to explain the observed optical flares with a duration of the order of one day or shorter, which are accompanied by X-ray flares of the same duration, by the reflection of X-ray emission from the outer protruding parts of the accretion structure (disk).

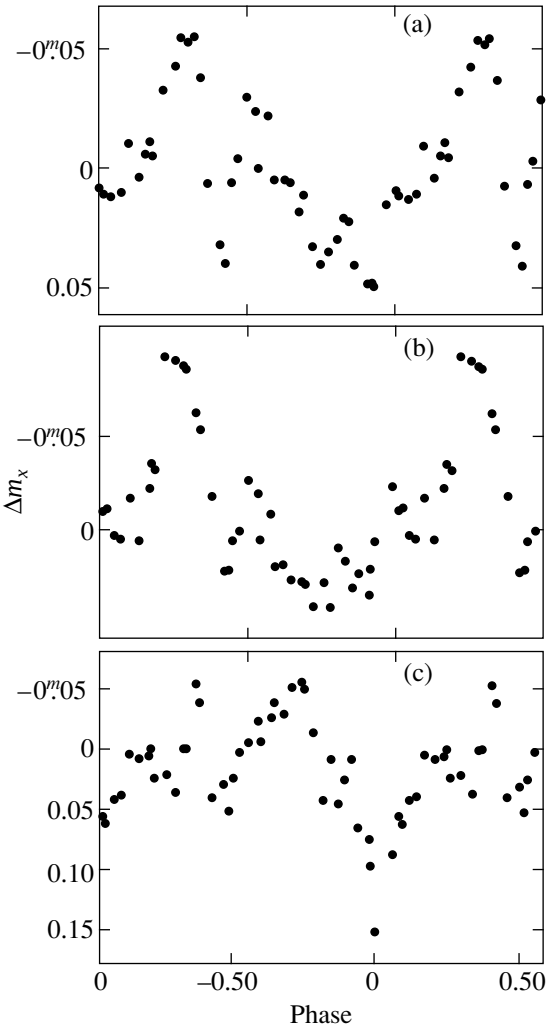

Fig. 7. Orbital X-ray (2–10 keV) light curve of Cyg X-1 (in magnitudes) constructed (a) over the entire period of observations under study JD 2450087–50422, (b) during the soft state JD 2450232–2450310, and (c) after the return to the "normal" state JD 2450232–2450422. The average smoothed light curves of the main 90-day outburst and the low-frequency discrete components with amplitudes higher than $0^m.10$ were first subtracted.

CONCLUSION

In 1996, we observed events associated with an enhancement of the Cyg X-1 activity. There is no direct optical manifestation of the 90-day soft X-ray outburst. However, a comparison of the X-ray and optical variabilities has revealed a relation between them, which is different on different characteristic time scales. We have found the following:

(1) There is a correlation between the variations in the mean optical and X-ray fluxes at a confidence level higher than 95% with a delay of the X-ray variations by one week on time scales of the order of several tens of days.

(2) We detected two fairly intense (for Cyg X-1) optical flares with amplitudes of $0^m.025$-$0^m.05$ on time scales of the order of several days, which coincided with 20% X-ray fadings. They could result from the thermal radiation of a hot gas clump with $T_g \approx 2 \times 10^4$ K and $N_e \approx 2 \times 10^{12}$ cm^{-3} produced when an irregularly flowing matter interacted with the accretion structure. While expanding, part of the gas spreads out and, falling on the line of sight, absorbs the X-ray emission.

(3) We discovered a week-long brightness decline by $0^m.04$, with which the 20% decrease in X-ray flux is associated. Such a dip may be attributable to the temporary disappearance of the outer part of the accretion disk, which is responsible for its optical emission.

(4) Some optical flares with a $0^m.02$ amplitude and a duration of shorter than or of the order of a day coincide in time with X-ray flares. The same flares also occurred in 1995 outside the active state. They may result from the processing of the X-ray flare radiation in the outer protruding parts of the accretion structure.

(5) We observed declines in the optical ($0^m.01$) and X-ray fluxes about one day in duration, which are most frequently correlated with each other.

The mean optical orbital light curve did not change and is consistent with the model of a tidally distorted star.

Fourier spectra of the optical and X-ray light curves revealed the same discrete components, which are close or multiples of each other (50^d, $16^d.8$, etc.). The common features of the main peaks in the X-ray and optical bands reflect their identical amplitude variations, which may be associated with the 294^d period found by Priedhorsky *et al.* [4] and Kemp *et al.* [1]. The time distribution of our data is not wide enough to reject or confirm the precession period of 294^d directly rather than indirectly. Fourier and correlation analyses confirmed the relation between the X-ray and optical variabilities.

The Fourier analysis of the X-ray data confirmed the $5^d.6$ orbital periodicity both during and outside the soft state of Cyg X-1. The orbital light curves suggest a redistribution of the obscuring matter around the accretion disk as these states change, which may be attributable to unstable mass transfer between the binary components. Other observational manifestations of the 1996 activity are probably also associated with this instability.

A comparison of the optical and X-ray variabilities yields an estimate of the characteristic time it takes for the matter to pass through the accretion structure; in 1996, it was about a week.

ACKNOWLEDGMENTS

We wish to thank O.V. Ezhkova and V.B. Kondrat'ev for help with the Mount Maidanak observations. V.P. Goranskiĭ and E.A. Karitskaya are grateful to K. Kuratov, director of the Tien-Shan Astronomical Observatory, and the staff for hospitality and allocation of observing time. This study was supported by the Ministry of Science of the Russian Federation through the scientific program "Optical Monitoring of Unique Astrophysical Objects" and in part by the Russian Foundation for Basic Research (project no. 98-06-17067) and the Astronomy program (no. 1.4.2.2).

REFERENCES

1. J. C. Kemp, E. A. Karitskaya, M. I. Kumsiashvili, *et al.*, Astron. Zh. **64**, 326 (1987).
2. V. M. Lyutyi, R. A. Sunyaev, and A. M. Cherepashchuk, Astron. Zh. **50**, 3 (1973).
3. V. V. Bruevich, N. N. Kilyachkov, R. A. Sunyaev, *et al.*, Pis'ma Astron. Zh. **4**, 292 (1978) [Sov. Astron. Lett. **4**, 292 (1978)].
4. W. C. Priedhorsky, J. Terrell, and S. S. Holt, Astrophys. J. **270**, 233 (1983).
5. N. G. Bochkarev and E. A. Karitskaya, Adv. Space Res. **8** (2–3), 205 (1988).
6. E. A. Karitskaya and N. G. Bochkarev, *Var. Phenomena in Close Bin. Stars* (Konkoly Obs. Hung. Akad. Sci., Budapest, 1989), Vol. 10, Part 7, No. 93, p. 255.
7. E. A. Karitskaya, Astron. Zh. **58**, 146 (1981).
8. J. C. Kemp, L. C. Herman, R. J. Rudy, *et al.*, Nature **270**, 227 (1977).
9. E. A. Karitskaya, Astron. Tsirk., No. **1088**, 1 (1979).
10. V. M. Lyutyi, Astron. Zh. **62**, 731 (1985).
11. E. N. Walker and A. R. Quintanilla, Mon. Not. R. Astron. Soc. **182**, 315 (1978).
12. S. W. Zhang, B. A. Harmon, W. S. Paciesas, *et al.*, IAU Circ. No. 6462 (1996).
13. S. W. Zhang, C. R. Robinson, and W. Cui, IAU Circ. No. 6510 (1996).
14. J. C. Kemp, M. S. Barbour, and R. E. McBirney, Astrophys. J. Lett. **244**, L73 (1981).
15. V. G. Kornilov and A. V. Krylov, Astron. Zh. **67**, 173 (1990).
16. V. G. Kornilov, I. M. Volkov, A. I. Zakharov, *et al.*, Trudy Gos. Astron. Inst. Sternberg **63** (1991).
17. V. G. Kornilov, Balt. Astron. **7**, 513 (1998).
18. V. M. Lyutyi, Perem. Zvezdy **18**, 417 (1972).
19. V. P. Goranskiĭ, E. A. Karitskaya, K. N. Grankin, *et al.*, Inform. Bull. Var. Stars, No. 4682 (1999).
20. G. Hill, R. W. Hilditch, and E. L. Pfannenschmidt, Victoria Obs. Publ. **15**, 1 (1976).
21. A. A. Hoag, H. L. Johnson, B. Iriarte, *et al.*, Naval Obs. Publ., Second series, **17**, VII (1961).
22. A. V. Mironov, *Precision Photometry* (EDEM, Moscow, 1997), p. 67.
23. E. A. Karitskaya, Candidate's Dissertation (Moscow, 1981).
24. N. G. Bochkarev, E. A. Karitskaya, and N. I. Shakura, Astron. Zh. **56**, 16 (1979).
25. W. Cui, IAU Circ. No. 6404 (1996).
26. E. A. Karitskaya and V. P. Goranskiĭ, Inform. Bull. Var. Stars, No. 4404 (1996).
27. I. B. Voloshina, V. M. Lyutyi, and A. E. Tarasov, Pis'ma Astron. Zh. **23**, 335 (1997) [Astron. Lett. **23**, 293 (1997)].
28. T. J. Deeming, Astrophys. Space Sci. **36**, 173 (1975).
29. V. Yu. Terebizh, *Analysis of Time Series in Astrophysics* (Nauka, Moscow 1992).
30. V. P. Goranskiĭ, V. F. Esipov, and A. M. Cherepashchuk, Astron. Zh. **75**, 240 (1998).
31. E. A. Karitskaya, Izv. Ross. Akad. Nauk **62**, 1787 (1998).
32. J. C. Kemp, Astrophys. J. **235**, 595 (1980).
33. B. Margon and S. Bowyer, Astrophys. J., Lett. **185**, Ed. L113 (1973).
34. V. Straizhis, *Multicolor Stellar Photometry* (Mokslas, Vilnius 1977).
35. N. G. Bochkarev and V. M. Lyutyi, Pis'ma Astron. Zh. **24**, 330 (1998) [Astron. Lett. **24**, 277 (1998)].

Translated by V. Astakhov

Astronomy Letters, Vol. 26, No. 1, 2000, pp. 34–37. Translated from Pis'ma v Astronomicheskiĭ Zhurnal, Vol. 26, No. 1, 2000, pp. 41–44.

A Flare of the H_2O Maser in the Source Orion KL

A. M. Tolmachev*

Pushchino Radio Astronomy Observatory, Astrospace Center, Lebedev Physical Institute, Russian Academy of Sciences, Pushchino, Moscow oblast, 142292 Russia

Received May 13, 1999

Abstract—In 1998, the intensity of the 1.35-cm H_2O maser radio line in the source Orion KL increased several hundreds of times. The observations of this flare and its behavior with time are presented. © *2000 MAIK "Nauka/Interperiodica".*

INTRODUCTION

Orion KL, one of the strongest sources of maser emission in the 1.35-cm water-vapor radio line, has been observed for many years with the RT-22 radio telescope of the Lebedev Physical Institute as part of a regular monitoring of such objects. During the burst of emission in 1984, its H_2O line intensity exceeded that of all the other sources by more than an order of magnitude. According to Garay *et al.* [1], the intensity of this line was at a maximum in October 1984–January 1985, when it was 6.7×10^6 Jy. Since then, it has decreased by almost a factor of 1000. In 1998, a new flare similar to the previous flare occurred in Orion. In this paper, we present the results of our observations of this flare with RT-22, but first, we recall that our radio telescope has the following parameters at 1.35 cm: the beamwidth is $2'.5$, the antenna sensitivity for a nonpolarized point-like source is 0.04 K Jy^{-1}, and the noise temperature with allowance for atmospheric noise is 200 K. The spectral resolution of the 128-channel filter-bank spectral analyzer used is 7.5 kHz (101 m s^{-1} in radial velocity at this wavelength).

RESULTS OF OBSERVATIONS

The source Orion KL is actually a whole cluster of maser condensations, which is not resolved spatially in single-dish observations but shows up in the line spectrum as a host of features with continuously varying intensities. Gaume *et al.* [2] provide a small-scale map of this area that was made from the VLA observations of 1991; this map shows precise spatial positions of all the features that existed at that time. Figure 1 shows the spectra of the H_2O line in Orion KL obtained with RT-22 in the second half of 1997 and in early 1998. The strongest features manifest themselves at radial velocities of 7.6 and 11 km s^{-1}. Below, we focus our attention on the analysis of only these features, the first of which is a remnant of the 1984 flare. Its coordinates on the map of Gaume *et al.* [2] are the following: R.A. = $5^h32^m46^s.646$, D. = $-5°24'29''.87$ (1950.0). The second feature, below called the neighboring feature, appears to be virtually unrelated physically to the first feature. Since only their radial velocities are similar, it is convenient to compare their intensities in simultaneous observations. On the map of Gaume *et al.* (1998), the feature with V_{LSR} = 11 km s^{-1} has the coordinates R.A. = $5^h32^m46^s.54$, D. = $-5°24'32''.2$.

The feature at a radial velocity of 7.9 km s^{-1} was most intense on January 22, 1998, and absolutely dominated the other features on February 26, 1998. A small jump in radial velocity (~200 m s^{-1}) slightly shook our confidence that the flare occurred at the same location. However, according to the VLBA observations carried out in March 1998 (V.I. Slysh, private communication), the coordinates of the flare feature match those given above. Subsequently, its intensity became so high that it was impossible to observe it by using the standard procedure, because the RT-22 calibration is made with a gas-discharge tube the calibration signal from which is equivalent to 2000 Jy, and it is difficult to calibrate a signal with an intensity exceeding this value by several orders of magnitude. We therefore used the following procedure: The source was observed by the beam edge, the signal from it was thus attenuated several tens of times, and only the intensity *ratio* of the brightest and neighboring features was measured. The spectral analyzer was retuned in frequency in such a way that the brightest feature was outside the analyzed band, the beam center was pointed toward the source, and we measured the intensity of the neighboring feature, as well as other spectral features, with the exception of the brightest one. Of course, we checked the linearity of the radiometer output, i.e., the constancy of the measured ratio at different signal-attenuation levels, and the invariability of other measured quantities (the widths and radial velocities of the spectral features). Since the calibration of the flare feature was made relative to the neighboring, second brightest feature in the source's spectrum, here we present the measurements for both

* e-mail: tolm@prao.psn.ru

Table 1. Parameters of the brightest feature and the neighboring feature in the spectrum of the maser in Orion KL. If the brightest feature on April 20, 1998, is fitted by one, rather than two Gaussians, its parameters are: 3.4×10^6 Jy, 0.43 and 7.86 km s^{-1}

Date	Main feature			Neighboring feature		
	F, Jy	ΔV, km s^{-1}	V_{LSR}, km s^{-1}	$F \times 10^4$, Jy	ΔV, km s^{-1}	V_{LSR}, km s^{-1}
July 25, 1997	1.2×10^4	0.42	7.59	1.7	0.58	11.00
	0.1	0.68	8.62	0.4	0.53	11.46
Aug. 20, 1997	1.3	0.40	7.61	2.1	0.53	11.06
	0.3	1.09	8.58	0.5	0.34	11.46
Sep. 17, 1997	1.2	0.42	7.60	2.0	0.58	11.08
	0.2	0.63	8.61	0.25	0.63	11.57
Dec. 24, 1997	0.8	0.60	7.65	1.1	0.63	11.05
	0.3	1.12	8.38	0.3	1.00	12.60
Jan. 22, 1998	0.4	0.35	7.47	1.2	0.56	11.02
	1.6	0.56	7.86	0.2	0.51	11.44
	0.35	0.52	8.55	0.3	1.04	12.45
Feb. 26, 1998	0.3×10^5	0.25	7.59	1.7	0.57	11.07
	1.4	0.25	7.85	0.3	0.68	11.50
	0.6	0.25	8.09			
	0.08	1.50	8.15			
Mar. 27, 1998	0.2×10^6	0.44	7.57	1.9	0.56	11.09
	1.5	0.37	7.90	0.4	0.72	11.66
	0.1	0.45	8.35			
Apr. 13, 1998	3.0×10^6	0.40	7.90	1.9	0.45	11.03
				0.55	0.64	11.38
Apr. 20, 1998	2.4	0.33	7.83	2.0	0.51	11.04
	2.2	0.36	8.01			
Apr. 27, 1998	3.2	0.45	7.90	2.1	0.52	11.01
May 11, 1998	0.04	0.25	7.20	1.5	0.53	11.04
	3.0	0.42	7.86			
	0.06	0.34	8.24			
May 25, 1998	2.9	0.48	7.87	1.7	0.52	11.02
June 2, 1998	0.7	0.27	7.60	1.6	0.52	11.01
	3.6	0.41	7.90			
June 15, 1998	2.7	0.47	7.88	1.2	0.54	11.01
July 2, 1998	2.7	0.49	7.88	1.25	0.55	11.00
July 16, 1998	3.0	0.51	7.89	1.1	0.58	11.03
Aug. 13, 1998	5.7	0.48	7.88	1.4	0.52	11.02
Sep. 16, 1998	3.8	0.49	7.85	1.5	0.50	11.01
Sep. 30, 1998	4.4	0.49	7.88	1.3	0.51	11.04
Oct. 13, 1998	4.3	0.47	7.87	1.3	0.48	11.02
Oct. 27, 1998	2.9	0.48	7.83	1.4	0.49	11.02
Nov. 17, 1998	6.5	0.50	7.82	2.0	0.49	11.03
Dec. 28, 1998	2.4	0.43	7.80	2.0	0.47	11.04
	0.4	0.25	7.53			
Jan. 18, 1999	1.5	0.48	7.76	2.1	0.48	11.02
Feb. 5, 1999	1.0	0.47	7.76	2.8	0.49	11.00
Feb. 18, 1999	6.0×10^5	0.50	7.76	2.2	0.51	11.03

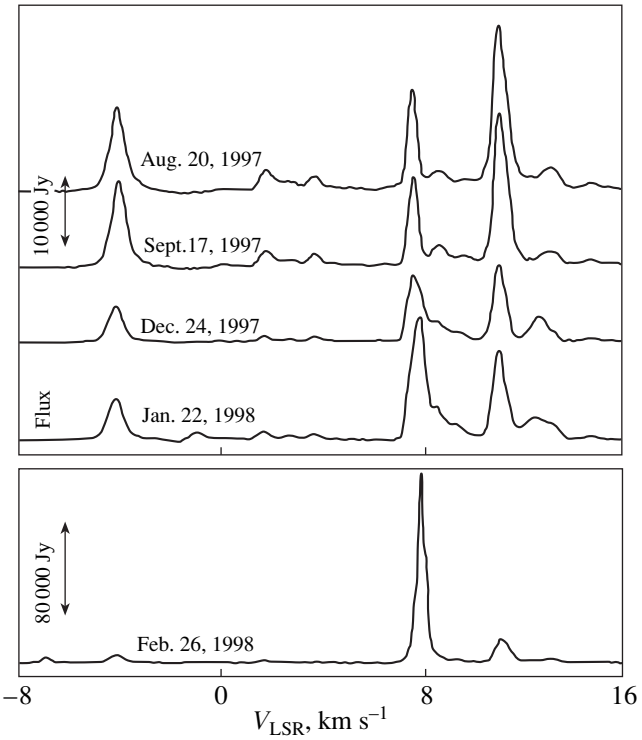

Fig. 1. Development of the flare in Orion KL. The vertical scale for the lower spectrum differs from that for the upper ones; the horizontal axis is common for all spectra.

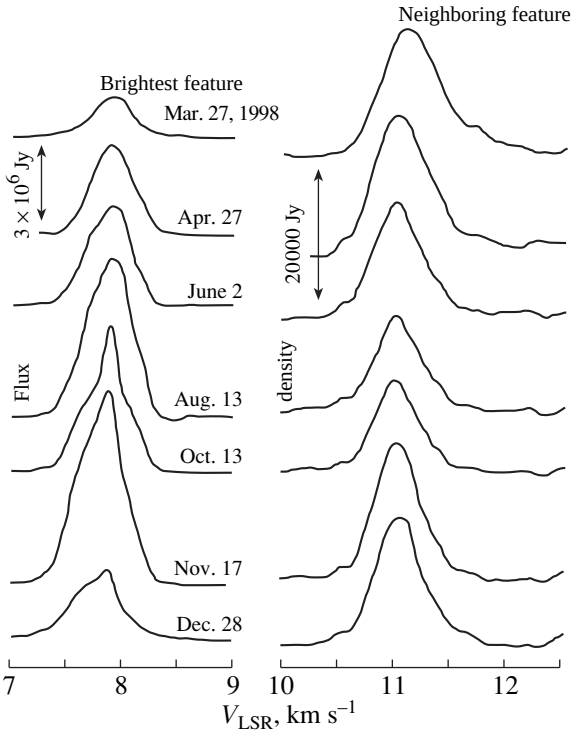

Fig. 2. Spectra of the flare feature and the neighboring feature; each feature is shown on its own vertical scale.

of them. Figure 2 shows portions of the spectra obtained in subsequent observations with the flare feature, together with the neighboring feature on a different scale. The behavior of the remaining, weaker spectral features is not considered here. In order not to overload the figure, not all of the observing sessions are shown in it, but all of their results are summarized in Table 1. Table 1 gives the parameters of the Gaussian fits to our spectra (the amplitude, FWHM, central radial velocity). The profiles of the brightest and neighboring features are sometimes well described by one Gaussian, sometimes the best fit is achieved by a superposition of several Gaussians; the table then gives the parameters of each of them. The errors in the measured parameters are 20% for the intensity and 0.02 km s^{-1} for the line width and velocity. No polarization characteristics of the emission were determined in these observations, although in this case the polarization is known to exist and be significant [3, 4]. Table 2 is provided to subsequently estimate its influence on the received signal. Given the altazimuth mounting of the antenna, the feedhorn-waveguide system of the RT-22 radiometer receives a vertically polarized emission. While moving over the sky, the source changes its orientation in the horizontal system of coordinates, and the position angle PA of the received polarization thus changes. For each observation, Table 2 gives the azimuth A at which it was made and PA. Above, we gave the reasons why the two features in the spectrum were observed nonsimultaneously during the flare. Figure 3 shows the light curve of the flare feature, i.e., a plot of its intensity *versus* time. The observations of numerous smaller features in the spectrum of Orion KL, together with an analysis of our data, will be the subject of the next paper. It should be noted, however, that the results of Matveenko *et al.* [5] largely determine the scope and line of further studies.

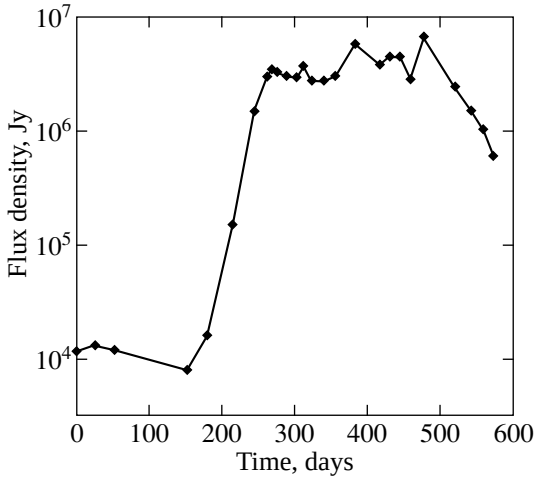

Fig. 3. Light curve of the H_2O maser in Orion KL; the zero time is July 25, 1997

Table 2. Azimuths for the times of observations and the corresponding position angles of polarization

Date of observation	Main feature		Neighboring feature	
	A, deg	PA, deg	A, deg	PA, deg
July 25, 1997	313	−25		
Aug. 20, 1997	333	−15		
Sep. 17, 1997	0	0		
Dec. 24, 1997	36	20		
Jan. 22, 1998	19	11		
Feb. 26, 1998	324	−20		
Mar. 27, 1998	309	−27	32	18
Apr. 13, 1998	309	−27	327	−18
Apr. 20, 1998	32	18	339	−12
Apr. 27, 1998	3	2	319	−22
May 11, 1998	326	−19	348	−7
May 25, 1998	347	−8	307	−28
June 2, 1998	310	−26	315	−24
June 15, 1998	310	−26	315	−24
July 2, 1998	326	−19	335	−14
July 16, 1998	2	1	350	−6
Aug. 13, 1998	331	−16	4	2
Sep. 16, 1998	296	−31	307	−28
Sep. 30, 1998	327	−18	316	−24
Oct. 13, 1998	312	−26	318	−23
Oct. 27, 1998	288	−33	303	−29
Nov. 17, 1998	32	18	338	−12
Dec. 28, 1998	338	−12	325	−19
Jan. 18, 1999	298	−31	321	−21
Feb. 5, 1999	319	−22	297	−31
Feb. 18, 1999	351	−5	329	−17

ACKNOWLEDGMENTS

I wish to thank the staff of the Pushchino Radio Astronomy Observatory: V.A. Samodurov for the use of his program of fitting the spectra by a set of Gaussians and A.A. Anichenkov for help with the computer preparation of the text of the paper and the figures. This study was supported by the Russian Foundation for Basic Research (project no. 99-02-16293). The staff of RT-22 was financially supported by the Russian Ministry of Science (project no. 01-10) and the State Science and Technology Program “Astronomy” (project no. 1.3.4.1).

REFERENCES

1. G. Garay, J. M. Moran, and A. D. Haschick, Astrophys. J. **338**, 244 (1989).
2. R. A. Gaume, T. L. Wilson, R. J. Vrba, *et al.*, Astrophys. J. **493**, 940 (1998).
3. L. I. Matveenko, Pis’ma Astron. Zh. **20**, 456 (1994) [Astron. Lett. **20**, 388 (1994)].
4. Z. Abraham, and J. W. S. Vilas Boas, Astron. Astrophys. **290**, 956 (1994).
5. L. I. Matveenko, P. D. Daimond, and D. A. Graham, Pis’ma Astron. Zh. **24**, 723 (1998) [Astron. Lett. **24**, 623 (1998)].

Translated by G. Rudnitskiĭ

Astronomy Letters, Vol. 26, No. 1, 2000, pp. 38–48. Translated from Pis'ma v Astronomicheskiĭ Zhurnal, Vol. 26, No. 1, 2000, pp. 45–56.

Determining the Period of the Long-Period Activity of the Water-Vapor Maser in W75N

E. E. Lekht[1,2]* and V. V. Krasnov[3]

[1] *Instituto Nacional de Astrofísica, Óptica y Electrónica, Luis Enrique Erro No. 1, Apdo Postal 51 y 216, 72840 Tonantzintla, Puebla, México*
[2] *Sternberg Astronomical Institute, Universitetskiĭ pr. 13, Moscow, 119899 Russia*
[3] *Pushchino Radio Astronomy Observatory, Astrospace Center, Lebedev Physical Institute, Russian Academy of Sciences, Pushchino, Moscow oblast, 142292 Russia*

Received April 1, 1999

Abstract—We present the results of our study of the H_2O maser emission from the source W75N, which is associated with a star-forming region, between November 1994 and March 1999. The observations were carried out with the RT-22 radio telescope of the Pushchino Radio Astronomy Observatory (Lebedev Physical Institute). The maser emission in 1994–1999 can be represented as a superposition of flares of separate components with a duration from two to six months, which occurred mainly in the radial-velocity range 8–17.5 km s^{-1}. We detected a regular drift of the velocity centroid from 13 to 9 km s^{-1} and an abrupt change in its velocity from 9 to 5 km s^{-1}, which took place at the initial stage of maser activity. Based on the variability of the total H_2O flux in all years of our observations of W75N (from December 1979 through March 1999), we conclude that the long-period variability of the water-vapor maser emission has a period of ~11.5 years. We give arguments that this variability is mainly associated with the most compact group of maser spots, whose positions coincide with the position of the continuum source VLA 2. © *2000 MAIK "Nauka/Interperiodica".*

INTRODUCTION

Attempts to determine whether a long-period variability of maser emission exists have been made since the first, more or less regular monitorings of 1.35-cm water-vapor maser sources associated with star-forming regions. However, the time interval of 5–8 years was not long enough to detect such a period. Subsequent regular observations showed that a monitoring must be performed during a longer time, no less than 10–12 years [1, 2]. These studies yielded the periods of long-period variability for several sources (ON1, ON2, G43.8–0.1, W49M). The periods are in the range 10–18 years, in agreement with the theoretical studies of Yorke and Krügel [3], Garlick [4], and Tutukov and Shustov [5]. According to these authors, the star-formation process is more or less stationary, but, nevertheless, oscillatory processes with a period of the order of 10 years may exist, and the forming star may have maxima and minima of its activity (luminosity).

A star at the initial formation stage is hidden from us by a dense gas–dust envelope, which rules out its visual study. The H II region produced by the star during this period is not yet sufficiently developed. Its size is occasionally no larger than 200–300 AU [6]. The age of such objects is estimated to be ~10^3 years. At present, the study of maser (mainly water-vapor) emission can be an indicator of how the star formation at a very early evolutionary stage proceeds.

Our goal here is to study the H_2O 1.35-cm maser emission from the source W75N. The long-term observations of W75N before 1994 were published by Lekht *et al.* [7], Lekht and Sorochenko [8], Lekht [9, 10], and Hunter *et al.* [11].

W75N is located in the star-forming region in Cygnus X, at the core of a molecular cloud. The H_2O maser emission in W75N was detected in 1972 [12]. The H_2O maser is observed toward H II(B), the most compact of the three H II regions found here [13]. The compact H II(B) region is associated with a far-IR source [14]. This IR source (IRS 1) is a reflection nebula; its illumination source coincides with H II(B) [15]. Subsequently, H II(B) was resolved into three ultracompact H II regions (UCH II): W75N(Ba), W75N(Bb), and W75N(Bc) [11]. Five groups of maser spots lie in the region of the brightest of them (Ba and Bb). All these sources (the ultracompact H II regions, the H_2O maser, and the OH maser) are located along the north–south line perpendicular to the axis of molecular outflow [16, 15, 11].

One of the two main groups of maser spots is located in the region of UCH II(Ba). Here one or two features are most intense in W75N, but the total velocity dispersion is smaller than that in the second group. The second group of maser spots has a considerably larger velocity dispersion and lies between Ba and Bb. The angular separation between these groups of maser

* e-mail: lekht@inaoep.mx

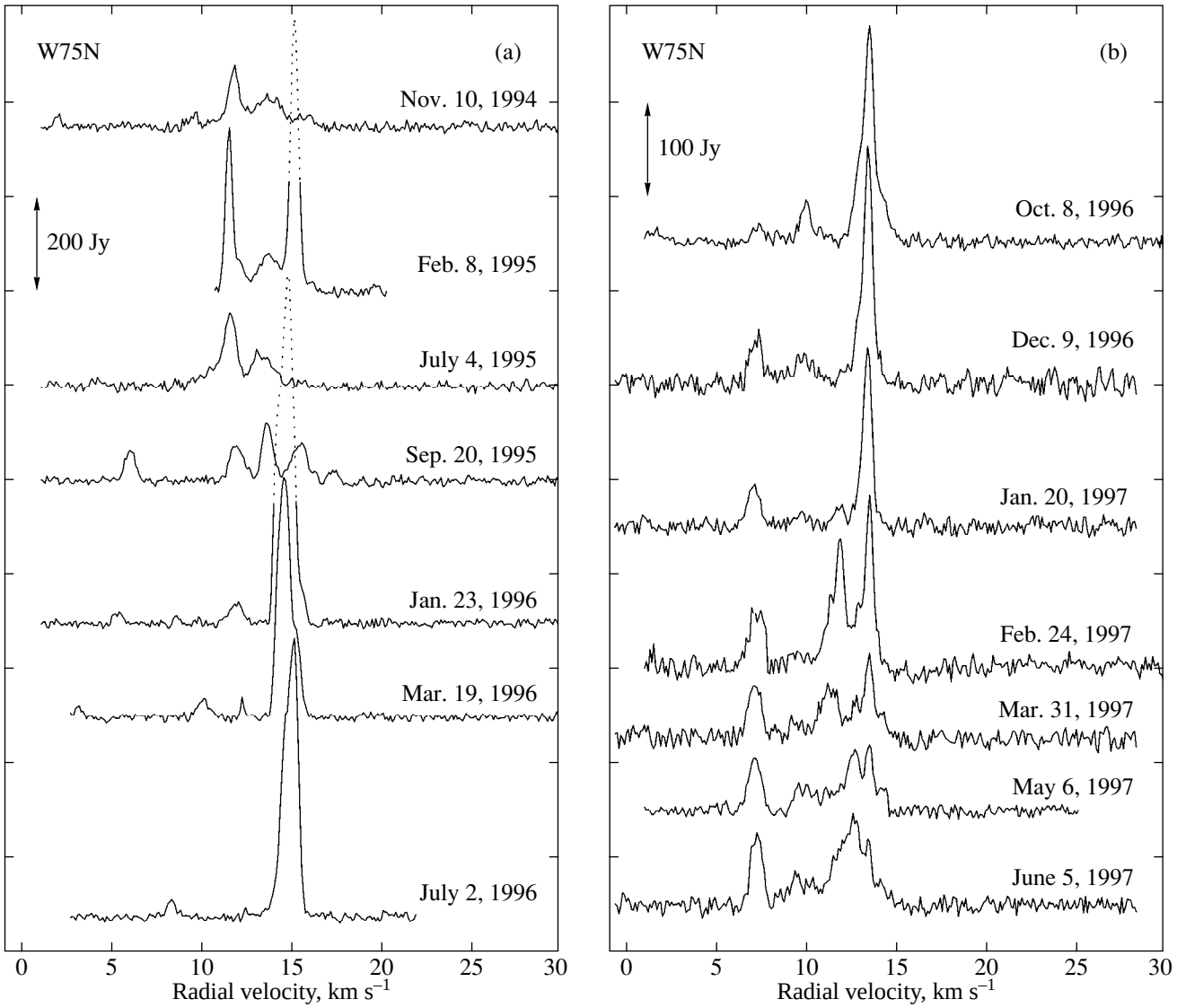

Fig. 1. Spectra of the H_2O maser emission in W75N for 1984–1998. The vertical arrow on the left indicates the value of the large scale division.

spots is less than 1″, which corresponds to $\leq 2.5 \times 10^{16}$ cm for a distance to W75N of 2 kpc.

Subsequent VLA observations of W75N [6] in the 1.35-cm continuum and in the water-vapor line at the same wavelength allowed the structure of this region to be refined appreciably. Three ultracompact H II regions, which were called VLA 1, VLA 2, and VLA 3, were found. The positions of VLA 1 and VLA 3 coincide with W75N(Ba) and W75N(Bb), respectively. VLA 2 lies between VLA 1 and VLA 3. The source VLA 1 is elongated approximately in the direction of the bipolar molecular outflow. The first group of maser spots coincides with this source and is also elongated in the same direction. The second group of maser spots coincides with VLA 2 and is located in an $0\farcs18 \times 0\farcs10$ (360×200 AU) envelope.

Thus, the difficulty of searching for a long-term variability of the H_2O maser emission in W75N with a single dish lies in the fact that the two groups of maser spots, each associated with its ultracompact H II region, are spatially close and have comparable fluxes.

RESULTS OF OBSERVATIONS

The 1.35-cm observations of W75N at a frequency of 22.23508 GHz were carried out with the RT-22 radio telescope of the Pushchino Radio Astronomy Observatory (Lebedev Physical Institute). The system noise temperature was in the range 150–230 K. A cooled transistor amplifier was used in the observations. The spectral resolution was 0.101 km s^{-1}. An antenna temperature of 1 K for a source with unpolarized emission corresponds to a flux density of 25 Jy. Since the beam

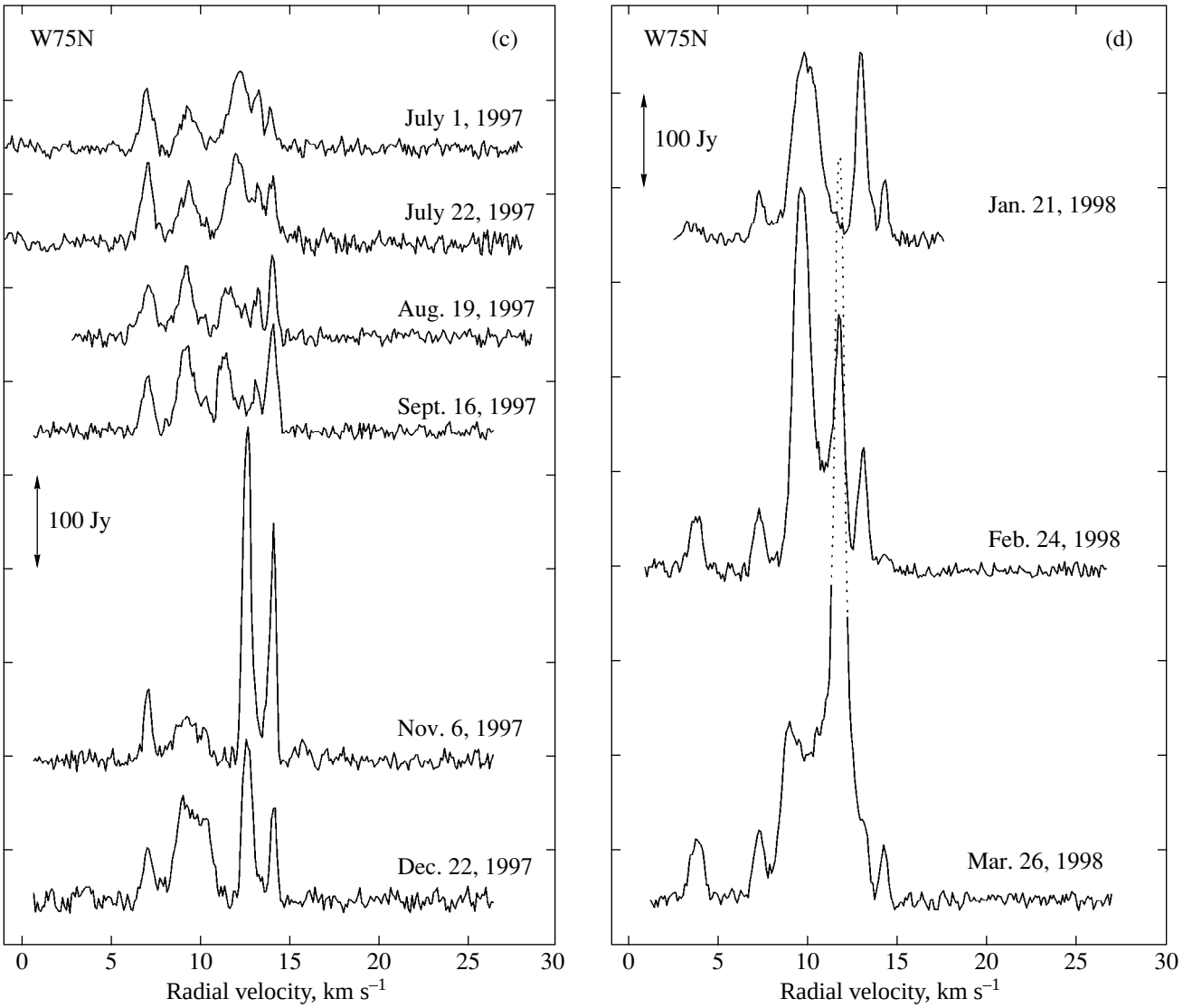

Fig. 1. (Contd.)

FWHM of RT-22 is 2.6′, we recorded the total emission from all the five groups of maser spots in W75N. The mean interval between two consecutive observing sessions was 1.5 months.

Figures 1a–1f show the spectra obtained from November 1994 through March 1999. The date of observation for each spectrum is given on the right. The radial velocities relative to the local standard of rest (V_{LSR}) are plotted along the horizontal axis. For the search of rapid variability of the emission, we took three spectra in December 1998 with an interval of 7 and 5 days (Fig. 2a). The subsequent spectra of January 20 and March 10, 1999, (Fig. 2b) confirm the existence of rapid variability of the H_2O emission and the growth of maser activity as a whole. Figure 3 shows all the spectra that we obtained between November 1994 and March 1999.

To qualitatively determine the pattern of evolution of the H_2O maser emission, we constructed a three-dimensional image (radial velocity, date of observation, and flux density) (Fig. 4.). The upper panel in the figure shows isophotes (in flux units) in the time–velocity coordinate plane. The principle of constructing a three-dimensional image is detailed in [1]. Note only that the missing baseline in several spectra up to the limiting velocities introduced in the graph was added. In addition, because of the long time intervals between the observations from late 1994 until mid-1995, a strong transient flare was registered only on February 8, 1995. For this reason, two auxiliary spectra were constructed as the mean spectra between the observations of November 10, 1994, and February 8, 1995, as well as between February 8 and July 4, 1995. These additions are needed for our three-dimensional imaging method to work. We did not include the velocities below zero,

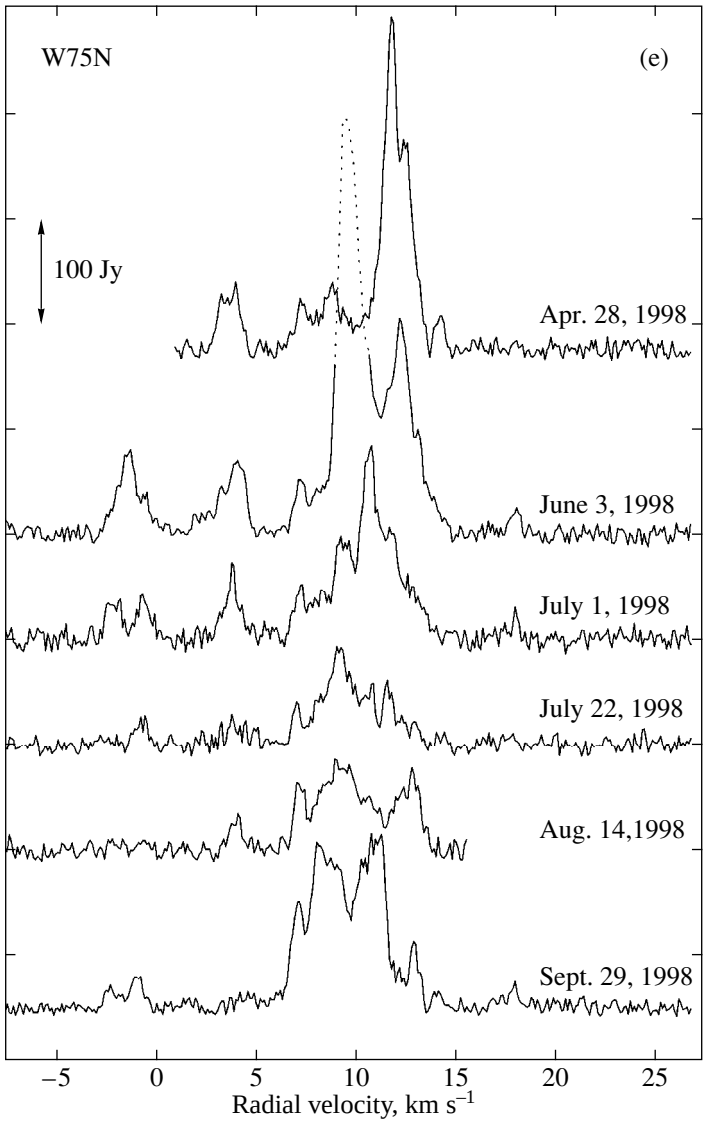

Fig. 1. (Contd.)

because the emission in this velocity range had always been weak (until 1998) and, furthermore, we began regular observations at $V_{LSR} < 0$ only in April 1998.

Figure 5a show the spectrum averaged over the three observations in December 1998. The heavy and thin lines in Fig. 5b represent the difference spectra obtained by subtracting the corresponding preceding spectrum from each succeeding one. The deviation of the curves from the zero level in the entire velocity range from –5 to 15 km s^{-1} implies that there is flux variability of all components.

Figure 6 shows variations in the integrated flux and position of the velocity centroid (weighted-mean radial velocity). The arrow in Fig. 6a marks the position of the total-flux minimum. The position of the velocity centroid was calculated for each spectrum using

$$V_c = \frac{\sum_i F_i V_i \Delta V_i}{\sum_i F_i \Delta V_i},$$

where F_i is the flux density at the radial velocity V_i; and ΔV_i is the velocity bin in the spectrum over which the summation was performed, which is numerically equal to the passband of the filter of the spectral analyzer.

A least-squares-fitted smooth curve without the last two points (January 20 and March 10, 1999) is shown in Fig. 6b. The curve demonstrates a regular drift of the velocity centroid. The rapid variations about this curve stem from the fact that the transient flares of individual components occurred at different radial velocities and in a fairly wide range of their values. Since January 1999, the emission at negative velocities increased

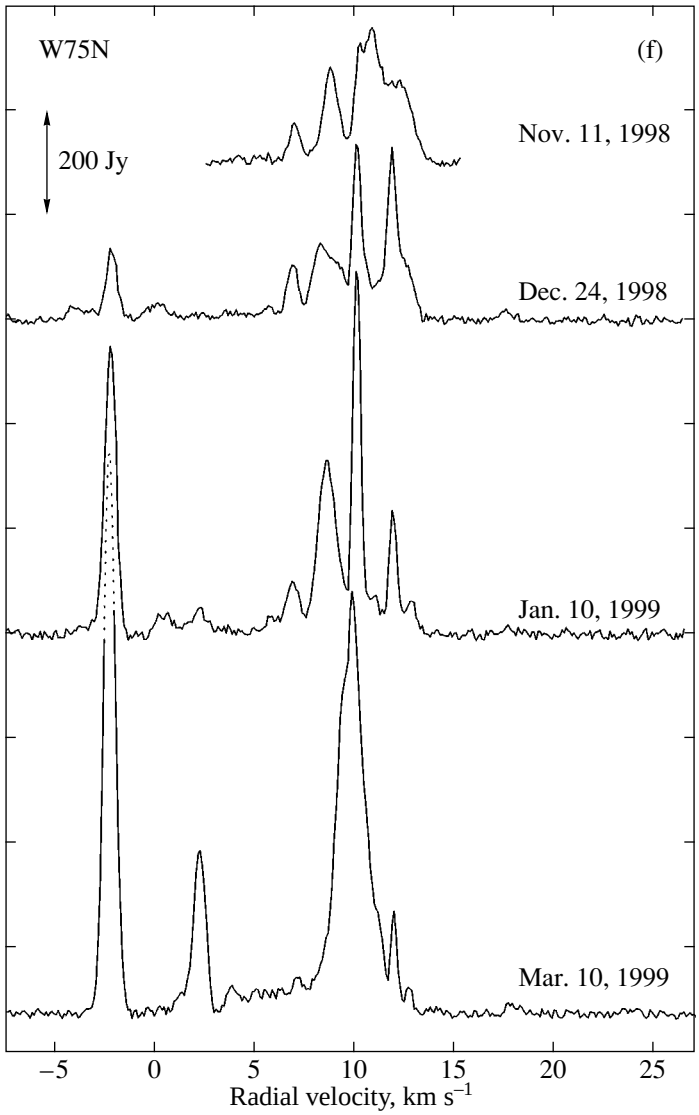

Fig. 1. (Contd.)

greatly in intensity, and a new feature appeared at –9.8 km s^{-1}. This caused the position of the velocity centroid to sharply displace to 5.4 km s^{-1}.

Figure 7 shows variability of the total H_2O flux for all years of our observations of the maser in W75N (1980–1999). Since there was a large break in the observations during one of the minima (May 1993–February 1994), the curve has a break. Four minima of maser activity, whose positions are indicated by the solid arrows, are clearly seen in the figure. There are maxima which are much smaller in amplitude than the main maxima between each pair of flux minima. The dotted arrows indicate the epochs of VLA observations.

DISCUSSION

The evolution of the H_2O maser emission in W75N during 1994–1999 has peculiarities compared to the previous periods of time. The main peculiarities are noted below.

(1) There are no stable spectral components that have been previously observed for several years. For example, the component that appeared in mid-1986 at V_{LSR} = 12.4 km s^{-1} was observed during the longest and most active period in the evolution of the W75N maser, and not at the activity minimum.

(2) There is a regular drift of the velocity centroid (no such studies have previously been carried out for the H_2O maser in W75N).

(3) The emission has appeared at low radial velocities (–10 km s^{-1}), at which it was not observed previously.

(4) Since 1993 there has been no emission at velocities > 20 km s^{-1}.

(5) A pronounced minimum of the total flux has existed for one year (late 1996–early 1997).

According to Figs. 3 and 4, the H_2O emission in the range of radial velocities 8–17.5 km s^{-1} can be represented as a superposition of flares of both individual

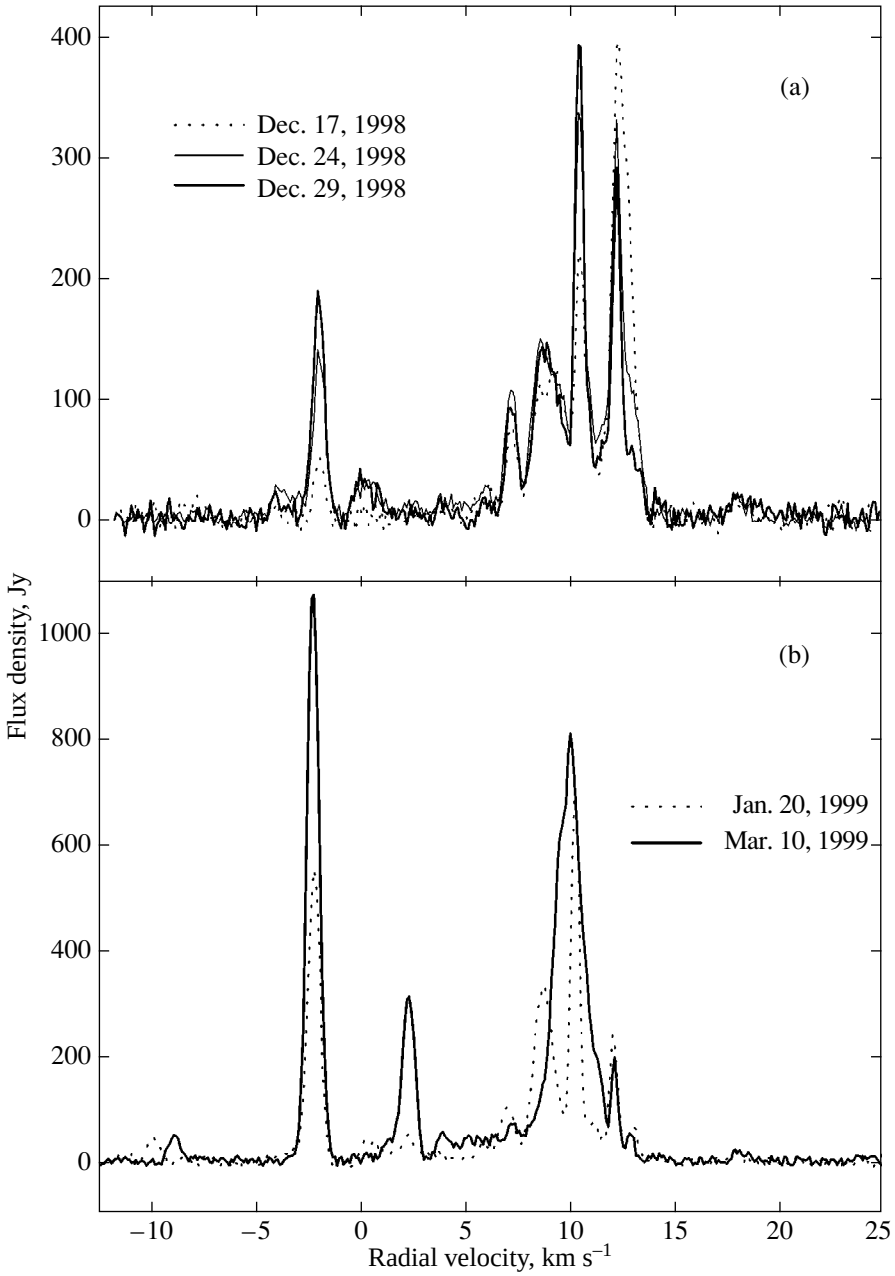

Fig. 2. The H_2O spectra obtained from December 1998 through March 1999, which show the existence of a rapid variability of the maser emission.

components and groups of spectrally close components. In addition, a chain of weaker features is traceable at radial velocities of 6–8 km s^{-1}. The lifetime of individual components at a 0.5 flux level ranged from two to six months and reached one year for a group of close (in radial velocity) features.

Rapid Variations in the Component Emission

There are two main groups of maser spots in W75N that are comparable in intensity and are separated by a distance of $\leq 2.5 \times 10^{16}$ cm [11, 6]. A single-dish spectrum is a superposition of the spectra of these groups of maser spots. For a more reliable identification of individual spectral components, especially weaker ones, we calculated an auxiliary mean spectrum using three spectra (December 17, 24, and 29, 1998) (Fig. 5a). We identified fifteen components in the radial-velocity range from –5 to 20 km s^{-1} with a flux higher than 10 Jy. The spectra of January 20 and March 10, 1999, confirm the existence of a rapid variability of almost all features at this epoch. We detected no variability of the component radial velocities in a period of one month. The emission at $V_{LSR} \approx -10$ km s^{-1} observed in January and March 1999 may be an exception. The velocity change in this time interval was 1 km s^{-1}.

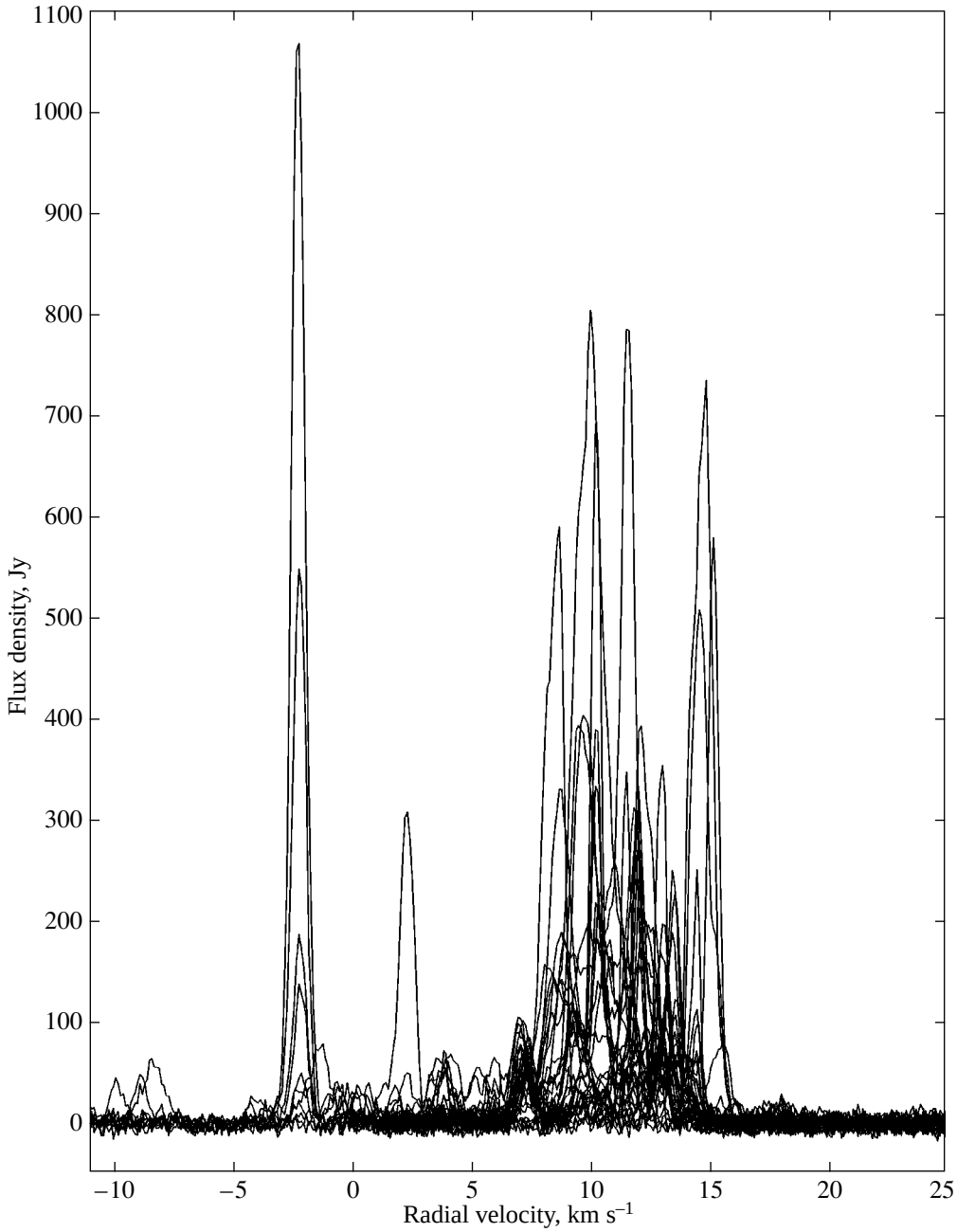

Fig. 3. Superposition of all the spectra obtained from November 1994 through March 1999.

The total number of components that were identified in each spectrum since December 17, 1998, was from 18 to 22. The lower flux limit was above 5 Jy. Given that some features disappeared, while others appeared, we recorded a total of 34 different features with a flux above 10 Jy between December 17, 1998, and March 10, 1999. In reality, there are more components in the H_2O spectrum. However, the very complex structure of the spectra, especially of their central part, prevents a reliable identification of all components, even those with fluxes of the order of 20–30 Jy. According to Torrelles *et al.* (1997), twenty spots were observed toward the two main groups of maser spots (VLA 1 and VLA 2) in December 1996. There were only six of them with fluxes above 4 Jy.

Thus, the increase in maser activity (which is most likely associated with the ultracompact region VLA 2) causes the number of observed maser spots to increase considerably. VLA observations during the periods of maser activity will allow us to increase appreciably the number of observed maser spots and thus to refine the structure they form.

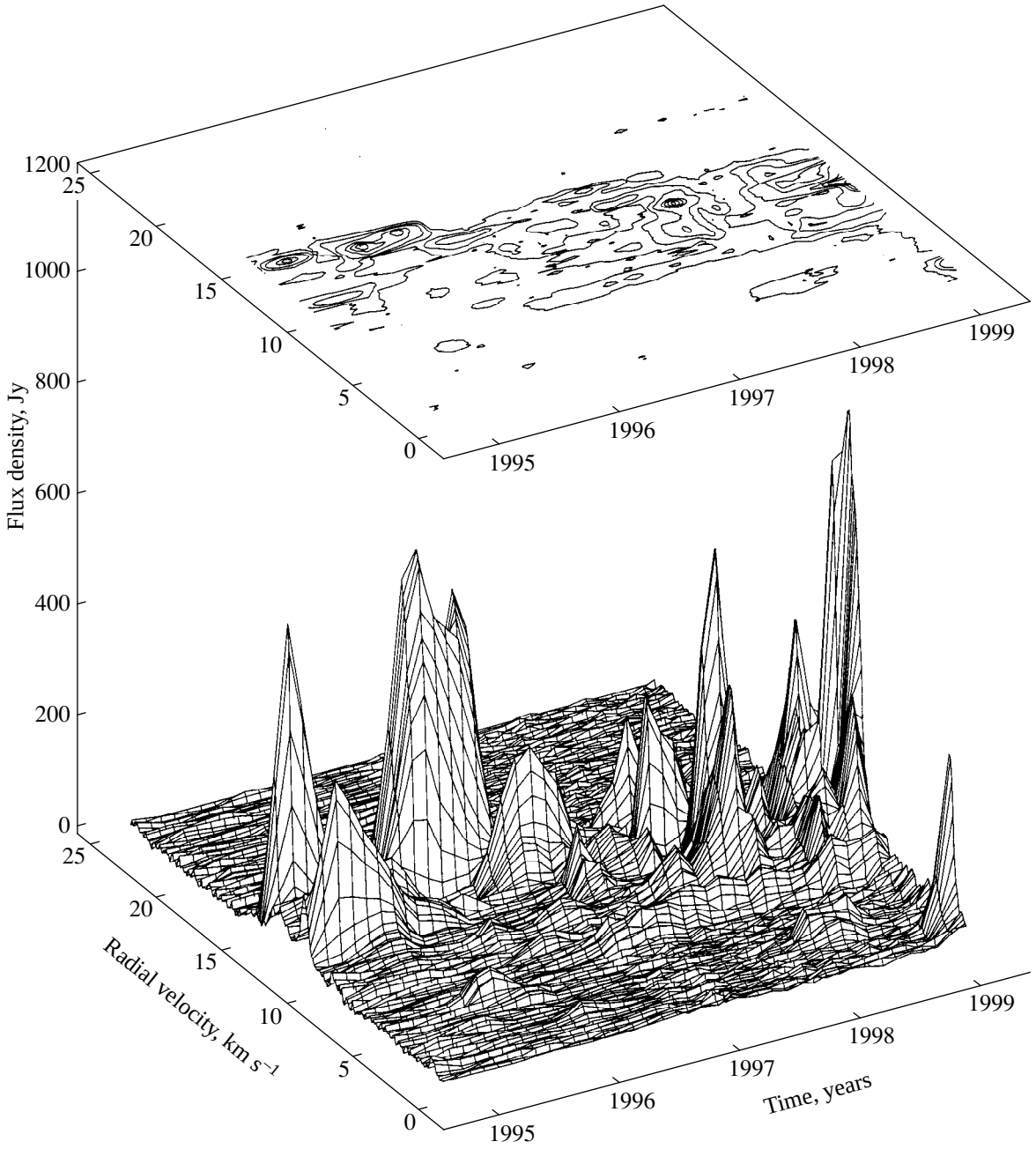

Fig. 4. Three-dimensional representation of the observations of the H_2O maser emission in W75N. The upper panel shows isophotes (in flux units) in the time–velocity coordinate plane.

The Velocity Centroid

An analysis of the H_2O spectra shows that the emission during 1994–1999 shifted to lower radial velocities. Moreover, the emission appeared where it was not observed previously, i.e., near -10 km s^{-1}. To determine the pattern of spectrum transformation, we plotted the velocity-centroid drift against time (Fig. 6b). The curve contains three types of drift: (1) a smooth drift (dashed line); (2) the superposition of small velocity variations within ± 1 km s^{-1} on it; and (3) an abrupt change in the position of the velocity centroid from 9 to 5.4 km s^{-1}.

The smooth drift of the centroid is explained by a gradual shift of the H_2O emission to lower radial velocities. The shift was attributable to the appearance of components at lower velocities (< -2 km s^{-1}) rather than to the drift of the components themselves. The rapid increase in their intensity since early 1999 has caused a sharp displacement in the position of the velocity centroid from 9 to 5.4 km s^{-1}.

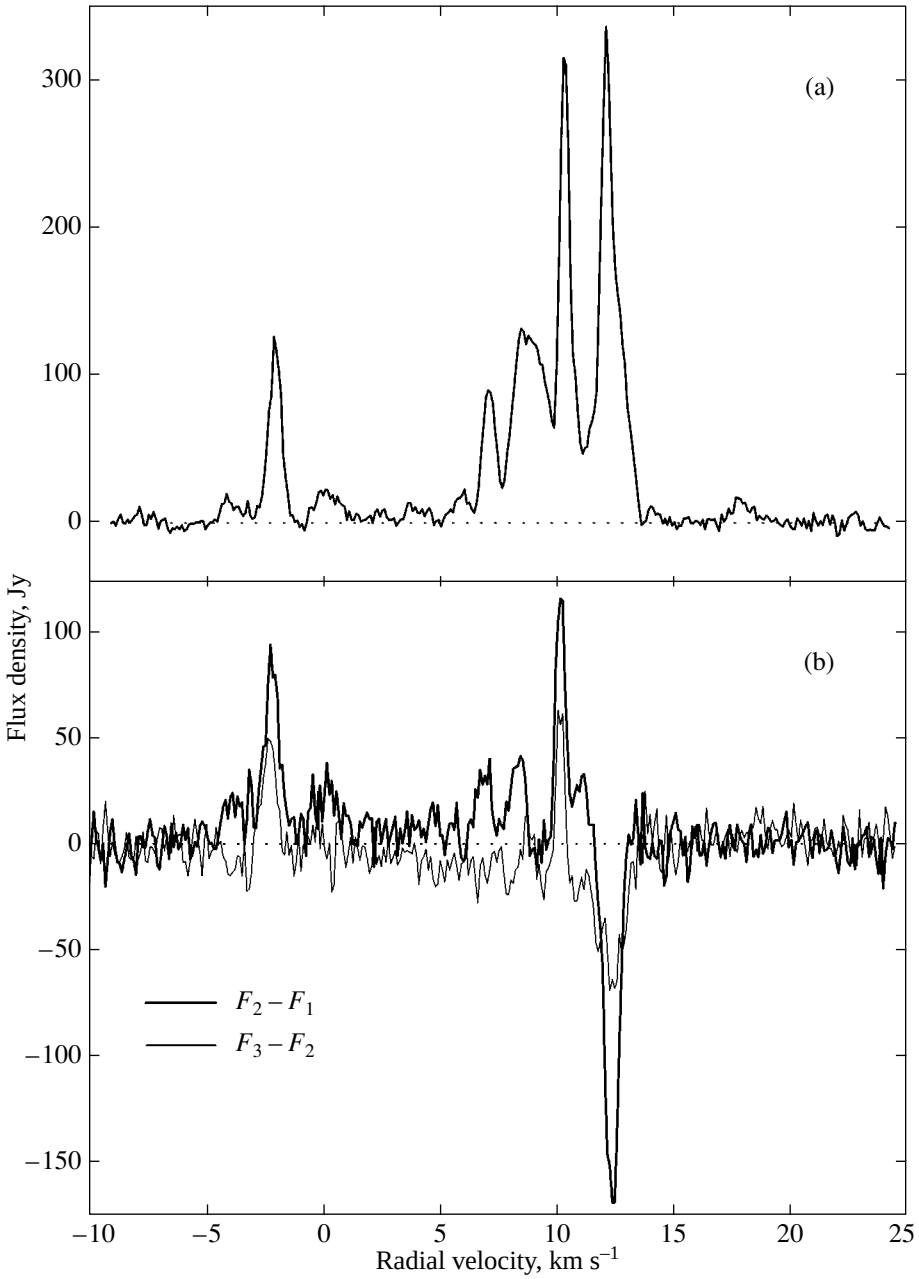

Fig. 5. (a) The mean spectrum of the H_2O maser emission in W75N in December 1998 and (b) the difference between the succeeding and preceding spectra for the same period of observations, where F_1, F_2, and F_3 are the spectra of December 17, 24, and 29, 1998, respectively.

Variability of the Total Flux

The time variations in the total H_2O maser flux from W75N during 1980–1992 were rather complex in pattern [9]. There were deep minima and strong maxima of the flux. Here we obtained two new minima with a minor maximum between them (Fig. 7). The pattern observed in 1982–1986 was repeated. The large increase in maser activity since 1998 suggests that the situation of 1987–1991 is repeated. The question arises: Which of the two groups of maser spots is responsible for the large increase in flux observed both previously (in 1981, 1983, and 1987–1991) and now? The VLA observations of W75N were carried out on November 24, 1992 [11] and December 15, 1996 [6], i.e., only at epochs close to the activity minima of the H_2O maser in W75N. It is therefore difficult to answer this question.

Nevertheless, based on Fig. 7, we assumed that a time interval of 11.5 years between the minima can be taken as the period of the long-period variability of the H_2O maser emission. In our view, the assumption that this variability is more likely associated with VLA 2

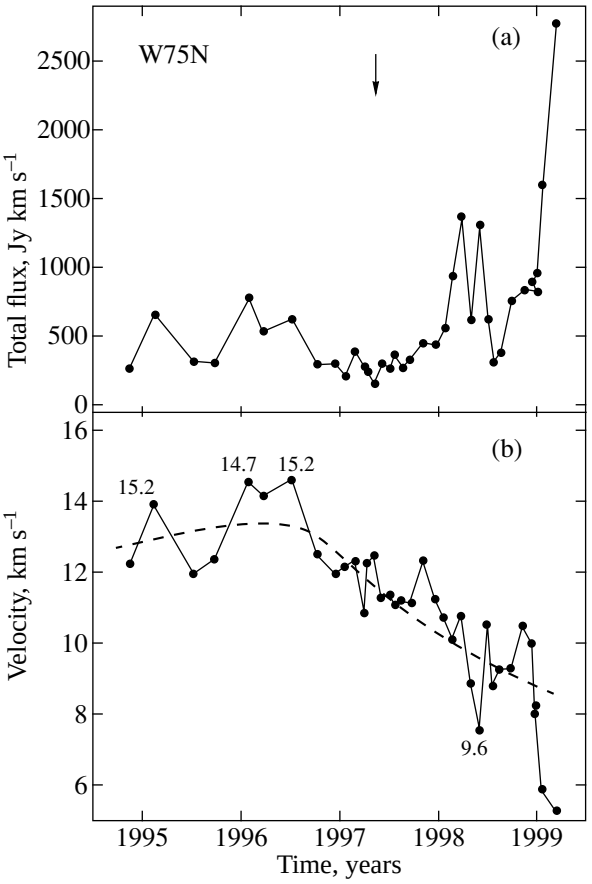

Fig. 6. (a) Variability of the total flux and (b) the velocity-centroid position. The arrow indicates the position of the longest minimum of the total flux. The dashed line represents a least-squares fitted smooth curve. The velocities of the flare components (in km s^{-1}), which caused rapid variations in the velocity centroid, are given near the corresponding points of the graph.

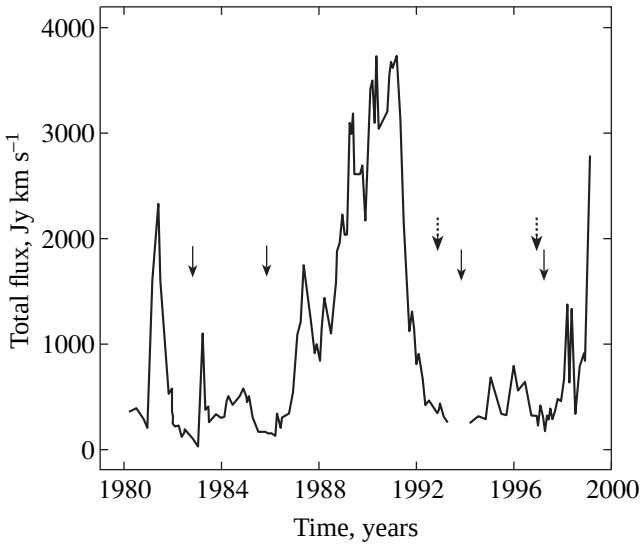

Fig. 7. Variability of the total flux in 1980–1999. The solid arrows mark the positions of the minima, and the dotted arrows indicate the epochs of VLA observations.

and the corresponding group of maser spots than with VLA 1 is preferred. The ground for this can be the following arguments: (1) the H_2O maser emission toward VLA 2 has a considerably larger radial-velocity dispersion than that in VLA 1 and thus gives a larger contribution to the total flux [11]; (2) the fluxes of many spectral components, including those at $V_{LSR} < 10$ km s^{-1}, increase simultaneously; and (3) the group of maser spots in the vicinity of VLA 2 is very compact and forms an envelope with a B0.5 star as the activity center [6], whereas the VLA 1 group is highly elongated along the molecular jet and forms a cylindrical structure.

It is important to note that the 1982–1987 and 1993–1999 segments in the curve of total-flux variability are similar. Thus, the large increase in total flux since 1998 follows the pattern that was observed in W75N since 1987. These circumstances can be an argument that any of the two maser sources (groups of spots) dominates in the total-flux variability. The large difference in the structure of the radio continuum sources VLA 1 and VLA 2 and the corresponding groups of maser spots inevitably results in a difference in the H_2O spectra and time scales of their variability.

These arguments may be inadequate for the final conclusion about which of the two groups of maser spots is dominant to be reached. If these groups give more or less identical contributions to the total flux, the curve of total-flux variability can be considered as a superposition of two curves with different periods. However, we have not yet performed such an analysis, because, in our view, it is necessary to have observations at least for two periods of maser activity in W75N.

CONCLUSION

(1) The H_2O maser emission in the source W75N during 1994–1998 can be mainly represented by a superposition of flares of individual or spectrally close components in the range of radial velocities 8–17.5 km s^{-1}. The typical lifetime of such components at a half-intensity level is from two to six months.

(2) Despite the erratic pattern of the velocity distribution of individual components, there was a regular drift of the velocity centroid from 13 to 9 km s^{-1} and a subsequent abrupt change in velocity to 5.4 km s^{-1}. This may be an argument for the increase in activity in one of the two main groups of maser spots, which has a wider range of velocities of the emission.

(3) The activity of the 1.35-cm water-vapor maser is cyclic in pattern with a probable period of the long-period variability close to 11.5 years. This most likely refers to the maser associated with the source VLA 2.

Since the structure of the maser region in W75N is complex, the interpretation of the total-flux variability may be ambiguous. A continuation of the long-term monitoring of W75N and subsequent VLA observations during the periods when the H_2O masers are not at activity minimum could refine the structure formed

by the maser spots associated with the ultracompact continuum sources VLA 1 and VLA 2, which are at different stages of evolution [6].

ACKNOWLEDGMENTS

This study was supported by the State Committee for Science and Technology of the Russian Federation on the RT-22 radio telescope facility (registration number 01-10) and the State Program "Astronomy" (project no. 1.3.4.1). We wish to thank the staff of the Pushchino Radio Astronomy Observatory for help with the observations.

REFERENCES

1. E. E. Lekht, J. E. Mendoza-Torres, M. I. Pashchenko, *et al.*, Astron. Astrophys. **343**, 241 (1999).
2. T. Liljestrom, K. Mattila, M. Toriseva, *et al.*, Astron. Astrophys. Suppl. Ser. **79**, 19 (1989).
3. H. M. Yorke and E. Krügel, Astron. Astrophys. **54**, 183 (1977).
4. A. R. Garlick, Astron. Astrophys. **68**, 113 (1978).
5. A. V. Tutukov and B. M. Shustov, Nauchn. Inf. Astrosovet. Akad. Nauk SSSR **41**, 125 (1978).
6. J. M. Torrelles, J. F. Gomez, L. F. Rodriguez, *et al.*, Astrophys. J. **489**, 744 (1997).
7. E. E. Lekht, M. I. Pashchenko, G. M. Rudnitskiĭ, *et al.*, Astron. Zh. **59**, 276 (1982).
8. E. E. Lekht and R. L. Sorochenko, Pis'ma Astron. Zh. **10**, 737 (1984) [Sov. Astron. Lett. **10**, 307 (1984)].
9. E. E. Lekht, Pis'ma Astron. Zh. **20**, 464 (1994) [Astron. Lett. **20**, 395 (1994)].
10. E. E. Lekht, Astron. Zh. **72**, 31 (1995).
11. T. R. Hunter, G. B. Taylor, M. Felli, *et al.*, Astron. Astrophys. **284**, 215 (1994).
12. K. J. Johnston, R. M. Sloanaker, and J. M. Bologna, Astrophys. J. **182**, 67 (1973).
13. R. Genzel and D. Downes, Astron. Astrophys. Suppl. Ser. **30**, 145 (1977).
14. A. D. Haschick, M. J. Reid, B. F. Burke, *et al.*, Astrophys. J. **244**, 76 (1981).
15. T. J. T. Moore, C. M. Mountain, T. Yamashita, *et al.*, Mon. Not. R. Astron. Soc. **248**, 377 (1991).
16. J. Fisher, D. V. Sanders, M. Simon, *et al.*, Astrophys. J. **293**, 508 (1985).

Translated by G. Rudnitskii

Astronomy Letters, Vol. 26, No. 1, 2000, pp. 49–60. Translated from Pis'ma v Astronomicheskiĭ Zhurnal, Vol. 26, No. 1, 2000, pp. 57–69.

On the Stability of the Phase Problem

V. Yu. Terebizh*

Sternberg Astronomical Institute, Universitetskiĭ pr. 13, Moscow, 119899 Russia

Received November 5, 1998; in final form, July 6, 1999

Abstract—Phase retrieval of a signal given its intensity is considered as a problem of statistically estimating a set of unknown parameters, the Zernike coefficients. Specifically, the phase problem is presented in the context of classical wave optics in the Fresnel approximation. Investigating the stability in this case suggests first learning if the Zernike coefficients can be restored in principle. If this is indeed the case, it then suggests determining the accuracy of their estimation. The stability of a solution to the phase problem depends, as it does for the other inverse problems, on the spectrum of the Fisher information matrix. An explicit representation of the Fisher matrix is given, and its spectrum is calculated for in-focus and out-of-focus images of a pointlike source. Simulations show that the solutions in the latter case are generally stable, so the coefficients of the Zernike series can be determined with an acceptable accuracy. The principal components, the mutually independent combinations of aberrations that are a generalization of the coefficients of the well-known Karhunen–Loeve decomposition, are calculated. As an example of this approach, the maximum-likelihood method is used to determine the aberrations of the optical system. © *2000 MAIK "Nauka/Interperiodica".*

1. INTRODUCTION

The problem of retrieving the phase of a complex signal from its observed intensity arises in various fields of physics and applied research, in particular, in atmospheric optics, computerized tomography, and crystallography (see, e.g., [1–4]. The main astronomical applications of this problem were initiated by radio and optical interferometric observations [5, 6]. In recent years, the phase problem has attracted particular attention in connection with the launch of the Hubble Space Telescope (HST). It emerged after the spacecraft launch that the HST images suffered a strong spherical aberration [7]. The solution of the corresponding phase problem allowed one to deduce the deviation of the primary-mirror surface from the design shape and then apply a correction to the optical system [8–12].

The phase problem is generally stated as follows. Assume that the object under study is characterized by a two-dimensional complex distribution,

$$p(u, v) = t(u, v)e^{i\phi(u, v)}, \qquad (1)$$

where $i = \sqrt{-1}$, the meaning of the u and v coordinates is determined by the specific problem, the real function $t(u, v)$ is known, and the phase $\phi(u, v)$ is to be retrieved from the known image intensity

$$I(x, y) = \left|\iint e^{-i\times 2\pi(xu + yv)} p(u, v)dudv\right|^2. \qquad (2)$$

To which extent can the characteristics of $\phi(u, v)$ be found from the specified modulus of the Fourier transform of the object and, possibly, some additional information?

Without dwelling on the uniqueness of the solution, which has been the subject of many studies, we only note that the iteration algorithm of Gerchberg and Saxton [13] and its outgrowth proposed by Fienup [14, 15] are used most commonly in practice to retrieve the phase information. The corresponding procedures and a comparison of the above algorithms with other methods of solving the phase problem can be found in the reviews by Fienup [16] and Dainty and Fienup [17].

Here, we consider the phase problem as a problem of statistically estimating a set of unknown parameters, the Zernike coefficients. Specifically, the phase problem is presented in the context of classical wave optics of a thin optical element [1]. Clearly, the phase problem belongs to the so-called inverse problems; in our case, we have an essentially nonlinear inverse problem of estimating the Zernike coefficients. The principal question associated with any inverse problem is its stability: Can the required information be retrieved from observational data, which inevitably suffer a variety of noises, with an acceptable accuracy? A general analysis of inverse problems [18–20] shows that the stability of their solutions is determined by the spectrum of the Fisher information matrix. Below, we therefore give an explicit representation of this matrix for the case in question. Model cases suggest that the phase problem is quite stable under certain conditions.

2. IMAGE-FORMATION MODEL

Let us consider the monochromatic image of an infinitely distant pointlike light source formed by an axisymmetric optical system. Let λ be the wavelength of the light; $(x', y', 0)$ and (x, y, z) are the Cartesian coordinates in the plane of the system's exit pupil and in the image plane, respectively; z is the symmetry axis of the system; $t(x', y')$ is the amplitude transparency function

* e-mail: terebizh@crao.crimea.ua

($0 \le t \le 1$) and $W(x', y', z)$ is the wave aberration of the system in the exit pupil when observed in the z plane (in units of wavelength). We define the pupil function as

$$p(x', y', z) \equiv t(x', y')e^{i \times 2\pi W(x', y', z)}. \quad (3)$$

Denoting the Fourier transform of the pupil function in the range of spatial frequencies (f_1, f_2) by $P(f_1, f_2, z)$, i.e.,

$$P(f_1, f_2, z) = \iint e^{-i \times 2\pi(f_1 x' + f_2 y')} p(x', y', z)dx'dy', \quad (4)$$

we have the following expression for the source's image intensity (see, e.g., [1, 21]):

$$I(x, y, z) = \frac{1}{(\lambda z)^2}\left|P\left(\frac{x}{\lambda z}, \frac{y}{\lambda z}, z\right)\right|^2. \quad (5)$$

Without the loss of generality, we assume that the aperture has the shape of a circle with diameter D. Let $\rho = 2\sqrt{x'^2 + y'^2}/D$ be the radial coordinate in the plane of the exit pupil normalized to unit maximum value, and θ be the corresponding angular coordinate. In the subsequent analysis, it is convenient to isolate the wave aberration in the paraxial focal plane $z = F$ by assuming that $w(\rho, \theta) \equiv W(x', y', F)$. In Fresnel's approximation, we then have

$$W(x', y', z) = w(\rho, \theta) + A_{20}(z)\rho^2, \quad (6)$$

where the coefficient

$$A_{20}(z) = -\frac{1}{8\bar{F}}\frac{\delta z/r_c}{1 + \delta z/F} \quad (7)$$

takes into account the defocus $\delta z = z - F$ when observed in the z plane, $\bar{F} = F/D$ is the focal ratio, and $r_c = \lambda\bar{F}$ is the critical radius for a given wavelength (the spatial frequencies above the critical frequency $f_c = 1/r_c$ of the optical system are known to be filtered out). Note that the condition $|\delta z| \ll F$ need not be satisfied. Denote the *point spread function of* the optical system by $h(x, y, z)$, i.e., the intensity distribution (5) normalized in such a way that the integral of $h(x, y, z)$ over the entire image surface is 1. It then follows from (3)–(7) that

$$h(x, y, z) = \frac{1}{(\lambda Dz)^2 t_0}\left|\iint \exp\left\{-i \times 2\pi\left[\frac{xx' + yy'}{\lambda z} - w(\rho, \theta) - A_{20}(z)\rho^2\right]\right\} t(x', y')dx'dy'\right|^2, \quad (8)$$

where the constant

$$t_0 = \frac{1}{D^2}\iint t^2(x', y')dx'dy'. \quad (9)$$

Equation (8) concretizes the inverse problem under consideration: It is required that the phase $w(\rho, \theta)$ be estimated for the specified point spread function and the amplitude transparency function. As for the coefficient $A_{20}(z)$, of interest are both alternatives: (i) the defocus δz is known in advance, and (ii) it is estimated together with the phase.

If we use the phase decomposition into the orthogonal system of two-dimensional functions $\{Z_j(\rho, \theta)\}$

$$w(\rho, \theta) = \sum_{j=1}^{\infty} a_j Z_j(\rho, \theta), \quad (10)$$

then the vector of coefficients $a = [a_1, a_2, \ldots]^T$ (as usual, the symbol T denotes transposition; below, by the vectors we mean column vectors) is the unknown object. The zero vector a corresponds to an ideal optical system, in which the star image represents the Airy diffraction pattern. For a number of fundamental reasons [21, 22], the set of Zernike polynomials [23], which in recent years has been used predominantly in Noll's nomenclature [24], became a standard orthonormal system of polynomials in optics. For simplicity, we restrict ourselves to the case of an unobstructed aperture. The orthogonality relations for the system of Zernike polynomials are

$$\frac{1}{\pi}\int_0^{2\pi} d\theta \int_0^1 Z_i(\rho, \theta)Z_j(\rho, \theta)\rho d\rho = \delta_{ij}, \quad (11)$$

where δ_{ij} is Cronecker's symbol. For clarity, we give the first eleven Zernike polynomials, which include third-order classical aberrations,

$$\begin{cases} Z_1 = 1, \\ Z_2 = 2\rho\cos\theta, \\ Z_3 = 2\rho\sin\theta, \\ Z_4 = \sqrt{3}(2\rho^2 - 1), \\ Z_5 = \sqrt{6}\rho^2\sin 2\theta, \\ Z_6 = \sqrt{6}\rho^2\cos 2\theta, \\ Z_7 = \sqrt{8}(3\rho^2 - 2)\rho\sin\theta, \\ Z_8 = \sqrt{8}(3\rho^2 - 2)\rho\cos\theta, \\ Z_9 = \sqrt{8}\rho^3\sin 3\theta, \\ Z_{10} = \sqrt{8}\rho^3\cos 3\theta, \\ Z_{11} = \sqrt{5}(6\rho^4 - 6\rho^2 + 1). \end{cases} \quad (12)$$

More specifically, Z_1 represents the constant phase shift; Z_2 and Z_3 describe the corresponding wavefront tilts; Z_4 specifies the field curvature; Z_5 and Z_6 correspond to the third-order astigmatism; Z_7 and Z_8 corre-

spond to the third-order coma; Z_9 and Z_{10} correspond to the triangular fifth-order coma; and Z_{11} corresponds to the third-order spherical aberration. Note that the error in the shape of the HST primary mirror is almost entirely attributable to the large (in absolute value) coefficient a $a_{11} \simeq -0.3$ μm (the mirror eccentricity squared is 1.0140 ± 0.0003 instead of the design value of 1.0022985).

In practice, we always deal with a discrete model. Setting the mesh size on the pupil equal to $\delta x' = \delta y' = D/M$, the pixel size in the image plane equal to $\delta x = \delta y = \lambda z/(Dg)$, and $N = Mg$, where $M \gg 1$ and $g \geq 2$ are integers, we introduce discrete counts,

$$h_{kl} = h(x_k, y_l, z)\delta x \delta y, \quad k, l = 0, 1, \ldots, N-1;$$

$$p_{mn} = \begin{cases} p(x'_m, y'_m, z), & m, n = 0, 1, \ldots M-1, \\ 0, & m, n \geq M. \end{cases} \quad (13)$$

As usual, the pupil function is framed by zeros. For this discretization, M is the number of cells into which the side of the square described around the exit pupil is broken up, g is approximately equal to the number of pixels at the radius of the diffraction image of a point, and N is the number of pixels at the diameter of the entire image $N\delta x$. In the focal plane at $z = F$, we have $\delta x = \delta y = r_c/g$, and the size of the entire image is Mr_c. As a result, relation (8) takes the form

$$h_{kl} = \frac{g^2}{t_0 N^4}\left|\sum_{m=0}^{N-1}\sum_{n=0}^{N-1}\exp\left\{-i\times\frac{2\pi}{N}(km+ln) + i\times 2\pi(w_{mn} + A_{20}\rho_{mn}^2)\right\}t_{mn}\right|^2, \quad (14)$$

where t and w are the $(N \times N)$ amplitude-transparency and wave-aberration matrices, respectively. Note that when the amplitude of a light wave is discretized, the *sampling theorem* [25–27] allows us to set $g = 1$. However, for the information about the intensity of the light to be properly kept, we should adhere to the condition $g \geq 2$, because the Nyquist frequency in this case is twice as high.

Let S be the mean number of events generated at the detector by the light source, and the $(N \times N)$ matrix $b = [b_{kl}]$ specify the mean background, including dark current, sky background, stray light, readout noise, etc. The mean number of detector counts during an exposure is then given by the matrix

$$q(a) = Sh(a) + b. \quad (15)$$

So far we have dealt with the mean quantities. Now we must take into account the inevitable stochastic nature of the counts when the light is recorded. Clearly, the nonuniqueness of the solution of the inverse problem is attributable to this phenomenon.

The precise statistics of photoevents is described by Cox–Mandel's distribution [28–30] or, as it is occasionally called, the double stochastic Poisson distribution. In the range of conditions that are of greatest interest, namely, when the exposure time exceeds significantly the coherence time of light, the statistics of photoevents can be fitted with a high accuracy by the standard Poisson law [31–33]. The fluctuations of all background components, except for the CCD readout noise which is a Gaussian random variable, obey the same law. Nevertheless, as was shown by Snyder *et al.* [34], for an appropriate choice of the normalization, the distribution of readout noise can also be considered to be Poissonian with an acceptable accuracy. We therefore assume that the detector counts in different pixels are Poissonian random variables with the means (15). In this case, the probability of obtaining a set of counts $y = [y_{kl}]$ in an experiment is

$$f(y|a) = \prod_{k,l=1}^{N} e^{-q_{kl}(a)}[q_{kl}(a)]^{y_{kl}}/y_{kl}!, \quad (16)$$

where the dependence of the probability density on object a is specified explicitly. Following Fisher, the distribution density $f(y|a)$ is commonly called the *likelihood* when it is considered as a function of the second argument. The quantity

$$J(y|a) \equiv -\ln f(y|a) \quad (17)$$

represents the *information* as defined by Shannon [26, 27] associated with sample y [19]. The statistical properties of $J(y|a)$ can be directly interpreted in terms of the theory of inverse problems; one of the most important tools in this sense is the Fisher matrix.

3. FISHER'S MATRIX

If we retain the finite number n of terms in the decomposition (10) at which the phase is represented with a satisfactory accuracy, then the estimated object a is the n vector. Clearly, any *estimate* $\tilde{a}$ of the object obtained from the observed image will almost certainly differ from the true value a, because the image is stochastic in nature. For the latter circumstance to be taken into account, apart from the observed image, we must consider the ensemble of random images Y, which is the set of all possible realizations formed in accordance with the distribution density (16). According to Rao–Cramer's inequality [35, 36], the accuracy of estimating the n-dimensional parameter a depends on the symmetric $(n \times n)$ matrix whose $I(a)$ components are given by the relations

$$I_{ij}(a) \equiv \left\langle \frac{\partial^2}{\partial a_i \partial a_j} J(Y|a) \right\rangle, \quad i, j = 1, \ldots, n. \quad (18)$$

The angular brackets here denote averaging over the ensemble Y. Since the matrix I was assumed to give objective "information" about the estimated parameter,

Fisher [35] called I the *information matrix*. Note that Fisher's definition of the information differs from Shannon's widely accepted definition [26, 27]. The properties of the information matrix are discussed in standard manuals on mathematical statistics (see, e.g., [36, 37]).

For the specific case considered here (the phase problem), the components of the Fisher matrix were analytically represented by Fienup *et al.* [10]. In this study, the diagonal components of I are calculated in order to determine, in accordance with Rao–Cramer's inequality, the minimum variance of the *unbiased* estimate of vector a, i.e., the estimate whose mean matches the true object. This gives an idea of the accuracy of object restoration, but the diagonal components of I do not fully characterize, by any means, the issue. The point is that precisely the *biased* estimates of the object are of greatest interest; it is desirable to choose the bias in such a way that the rms deviation of the estimate from the true object is at a minimum (the well-known Kolmogorov–Wiener filter may serve as a good example in this respect). However, Rao–Cramer's inequality becomes much more complicated for biased estimates: the lower limit on the scatter of the estimate depends markedly on the form of the bias function, which is not known *a priori*. For this reason, the value of Rao–Cramer's inequality for real problems is unfortunately very limited.

Without going into further details, we note here that the Fisher matrix in the *Occamian* approach to inverse problems [19, 20] specifies the shape and orientation of the *feasible region* (FR). In the linear approximation, the FR is an n-dimensional ellipsoid whose principal axes are parallel to the eigenvectors $v_1, \ldots, v_n$ of the Fisher matrix and the lengths of its principal axes are inversely proportional to the square root of the eigenvalues $\lambda_1, \ldots, \lambda_n$ of this matrix. Since I is a positive-defined matrix, all its eigenvalues are positive. By numbering them in decreasing order, we have, according to the well-known *spectral theorem* (see, e.g., [38]),

$$\begin{cases} I = V\Lambda V^{\mathrm{T}}, \ V = [v_1, v_2, \ldots, v_n], \ V^{-1} = V^{\mathrm{T}}, \\ \Lambda = \mathrm{diag}(\lambda_1, \lambda_2, \ldots, \lambda_n), \ \lambda_1 \geq \lambda_2 \geq \ldots \geq \lambda_n > 0. \end{cases} \quad (19)$$

These relations imply that the orthogonal matrix V is composed of the eigenvectors of I, while the diagonal matrix Λ contains the spectrum of I. The ratio $c \equiv \lambda_1/\lambda_n$ is known as the *condition number*, in our case, of matrix I. However, we avoid using the concept of condition, because the actual stability of the inverse problem depends not only on c but also on the form of the entire spectrum of the Fisher matrix.

If the spectrum of I covers a wide range of values, then the semiaxes of an ellipsoidal FR differ greatly in magnitude (in practice, the difference generally reaches tens of orders of magnitude!). This is equivalent to the assertion that some combinations of the estimated parameters (the components of vector a) which correspond to the longest FR semiaxes have a very large rms deviation from the true values. The variance of these components even for relatively simple problems is generally so large that their determination from observations should be considered impossible. Accordingly, the Occamian approach suggests that only the most informative set of *principal components* of the inverse estimate is retained. If, however, the spectrum of I is relatively narrow, then the inverse problem is stable and direct methods of estimating the object, such as the inverse solution and the maximum-likelihood method, are admissible.

For arbitrary ensembles that obey the Poisson statistics, the Fisher matrix admits of the following factorized representation via the basic parameters of the direct problem [18]:

$$I(a) = H^{\mathrm{T}} Q(a)^{-1} H, \quad (20)$$

where H is the point spread function, and Q is the diagonal matrix with the components of the vector of means $q(a)$. Before reducing the matrix H to a form convenient for the calculations, we perform auxiliary transformations in the decomposition (10).

According to (12), the first polynomial Z_1 is a constant, so the coefficient a_1 has no effect on the image and it may be chosen arbitrarily; we assume for convenience that $a_1 = 0$. Next, as we see from (12) and (14), the coefficient a_4 of the Zernike polynomial $Z_4(\rho, \theta)$ affects the field curvature just as the defocus does. For this reason, it makes sense to consider these factors simultaneously. Assuming that

$$\begin{cases} \alpha_1 = a_2, \\ \alpha_2 = a_3, \\ \alpha_3 = a_4 + \dfrac{A_{20}}{2\sqrt{3}}, \\ \alpha_4 = a_5, \\ \ldots \\ \alpha_l = a_{l+1}, \\ \ldots \\ \alpha_{n-1} = a_n, \end{cases} \quad (21)$$

we obtain from (10)

$$w(\rho, \theta) + A_{20}\rho^2 = A_{20}/2 + \sum_{l=1}^{n-1} \alpha_l Z_{l+1}(\rho, \theta). \quad (22)$$

The first term on the right-hand side of (22) does not affect the image, so it is necessary to estimate the $n - 1$ parameters $\alpha_1, \ldots, \alpha_{n-1}$. Accordingly, to specify the dependence on the object, below we use α instead of a. If the defocus δz is specified in advance, then, after obtaining an estimate $\tilde{\alpha}$, we can estimate the system's internal field curvature from (7) and (21),

$$\tilde{a}_4 = \tilde{\alpha}_3 - \frac{A_{20}}{2\sqrt{3}}. \quad (23)$$

Otherwise, only the total field curvature is estimated, while its components remain hidden.

We now turn to the derivation of matrix H in (20). To this end, it is convenient to pass to a one-dimensional data representation [10, 39]. More specifically, denote the discrete Fourier transform of the pupil function, i.e., the matrix whose elements are given by the double sum on the right-hand side of (14), by $F = [F_{k_1, k_2}]$. Next, let $R = N^2$ and $L = [L_j]_{j=1}^{R}$ be the column vector composed of the successive columns of matrix F. For brevity, we designate the operation of drawing out the matrix in a column by $\vee$, so

$$L = \vee F = \vee\left\{\sum_{m=0}^{N-1}\sum_{n=0}^{N-1}\exp\left[-i\times\frac{2\pi}{N}(k_1 m + k_2 n) + i\times 2\pi(w_{mn} + A_{20}\rho_{mn}^2)\right]t_{mn}\right\}. \quad (24)$$

Similarly, we "stretch out" the matrices q, h, and b in (15) while retaining the previous designations for them. The vector of the mean image of length R is then

$$q = \kappa|L|^2 + b, \quad \kappa \equiv \frac{g^2 S}{t_0 N^4}, \quad (25)$$

and the diagonal matrix is $Q = \mathrm{diag}(q_1, \ldots, q_R)$. According to (16), the probability of obtaining an image realization $\nu = [\nu_1, \nu_2, \ldots, \nu_R]^{\mathrm{T}}$ in an experiment is

$$f(\nu|\alpha) = \prod_{j=1}^{R} e^{-q_j(\alpha)} q_j(\alpha)^{\nu_j}/\nu_j!, \quad (26)$$

and the corresponding Shannon information (17) is

$$J(\nu|\alpha) = \sum_{j=1}^{R}[q_j(\alpha) - \nu_j \ln q_j(\alpha) + \ln \nu_j!]. \quad (27)$$

Next, according to (18), the elements of the Fisher matrix are

$$I_{lm}(\alpha) = \left\langle \frac{\partial^2}{\partial\alpha_l \partial\alpha_m} J(Y|\alpha)\right\rangle, \quad l, m = 1, 2, \ldots, n-1. \quad (28)$$

Substituting (25) and (27) in (28) yields

$$I_{lm}(\alpha) = (4\pi\kappa)^2 \sum_{j=1}^{R}\frac{1}{q_j}\Im(L_j^* \Phi_{jl})\Im(L_j^* \Phi_{jm}), \quad (29)$$

where the asterisk denotes complex conjugation, and $\Im(z)$ is the imaginary part of z. The $R \times (n-1)$ matrix $\Phi = [\Phi_{jl}]$ is composed of the columns Φ_l of length R, which are obtained by the above operation of drawing out the $(N \times N)$ matrix of the Fourier transform of the product of the pupil function and the $(l+1)$ Zernike polynomial:

$$\Phi_l = \vee\left\{\sum_{m=0}^{N-1}\sum_{n=0}^{N-1}\exp\left[-i\times\frac{2\pi}{N}(k_1 m + k_2 n) + i\times 2\pi(w_{mn} + A_{20}\rho_{mn}^2)\right]t_{mn} Z_{l+1}^{(mn)}\right\}. \quad (30)$$

Finally, let us form the matrix $H = [H_1, \ldots, H_{n-1}]$ from the columns

$$H_l = 4\pi\kappa\Im(L^{*.} * \Phi_l), \quad (31)$$

where, as usual, the sign $.*$ denotes an element-by-element multiplication of the arrays. The sought-for representation of the Fisher matrix in the form (20) then directly follows from formulas (29) and (31).

When the spectrum of $I(\alpha)$ is calculated, it is appropriate to use the decomposition

$$I = A^{\mathrm{T}} A, \quad (32)$$

where we introduced the $[R \times (n-1)]$ matrix

$$A(\alpha) \equiv Q(\alpha)^{-1/2} H. \quad (33)$$

In the notation adopted above, the columns of matrix A are simply expressed in terms of vectors q and H_l:

$$A_l = (1./\sqrt{q}) .* H_l, \quad l = 1, 2, \ldots, n-1, \quad (34)$$

where the sign ./ corresponds to an element-by-element division. After the matrix A has been formed, it is easy to perform its *singular-value decomposition* in the form

$$A = U\Delta V^{\mathrm{T}}. \quad (35)$$

Here, U is an $[R \times (n-1)]$ matrix with orthonormal columns, Δ is a diagonal $[(n-1) \times (n-1)]$ matrix, and V is an orthogonal matrix of the eigenvectors of I in the spectral decomposition (19). As for the eigenvalues $\lambda_1, \ldots, \lambda_{n-1}$ of the Fisher matrix, substituting (35) in (32) yields

$$\Lambda = \mathrm{diag}(\lambda_1, \ldots, \lambda_{n-1}) = \Delta^2. \quad (36)$$

Thus, when the system of eigenvalues and eigenvectors of the Fisher matrix is constructed, the sequence of calculations appears as follows. By specifying the defocus δz, the order of approximation n, and the Zernike coefficients $a_2, \ldots, a_n$ of the wave aberration, we calculate the phase from formulas (7), (21), and (22). The subsequent specification of the image-discretization parameters g, M and the amplitude transparency function $t = [t_{mn}]$ of the optical system allows us to calculate the constant t_0 from (9) and the vector L from (24). To determine the mean image q in (25), the brightness of pointlike source S and the additive background $b =$

$[b_{mn}]$ should be specified. Finally, formulas (30), (31), and (34)–(36) allow the vectors Φ_l, H_l and the matrices A, Δ, V, and Λ to be determined sequentially.

Important information about the correlation between the derived estimates can be extracted from the form of eigenvectors $\{v_l\}$. We cannot go into the details of the Occamian approach to inverse problems [19, 20], in which the meaning of the principal components $p = [p_1, \ldots, p_{n-1}]^T$ of the inverse solution is clearly elucidated. Suffice it to say here that the principal components are mutually uncorrelated linear combinations of the components of the vector of inverse estimate α_{inv} which are formed in such a way that they successively "draw" information out of the unstable inverse solution in a *theoretically most efficient way.* The variance of the principal components increases (strictly speaking, does not decrease) as their number increases. The principal components are a generalization of the coefficients of the well-known Karhunen–Loeve decomposition to a nonsteady random process with allowance for photon noise. If the matrix V in the spectral representation (19) of the Fisher matrix is known, the principal components can be calculated by a simple rotation of the coordinate system,

$$p = V^T \alpha_{inv}, \tag{37}$$

i.e., $p_1 = v_1^T \alpha_{inv}, \ldots, p_{n-1} = v_{n-1}^T \alpha_{inv}$ are the inverse (or maximum-likelihood) estimates of the coefficients $\{\alpha_{inv,l}\}$ which are taken with the weights equal to the components of the eigenvectors of I.

4. MODEL CASES

Below we calculate the spectrum of the Fisher matrix for several simple situations which are of practical interest. Let us first consider the in-focus image ($z = F$) of a point-like source formed by an ideal telescope ($a = 0$),

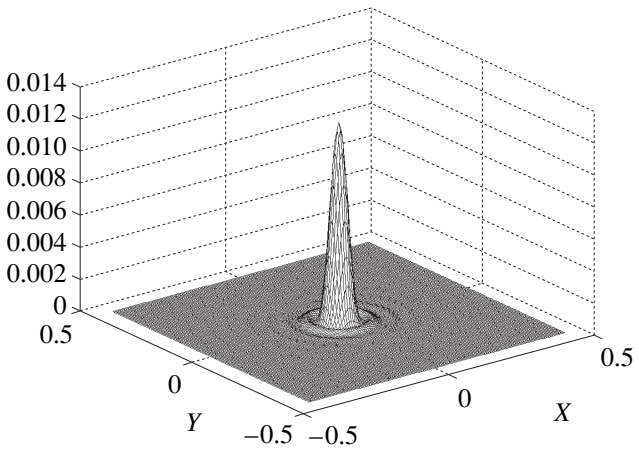

Fig. 1. In-focus image of a point source formed by an ideal telescope under the observing conditions (38). The X and Y coordinates are in arcseconds.

i.e., the Airy diffraction pattern. We assume the following values of the attendant parameters:

$$\begin{cases} \text{Telescope diameter} & D = 2400 \text{ mm}, \\ \text{Focal ratio} & \bar{F} = 24.0, \\ \text{Wavelength} & \lambda = 6328 \text{ Å}, \\ \text{Star brightness} & S = 1 \times 10^7 \text{ events}, \\ \text{Background level} & b_{mn} = 10 \text{ events pixel}^{-1}, \\ \text{Maximum order of the Zernike decomposition} & n = 55, \\ \text{Discretization in the exit pupil} & M = 32, \\ \text{Discretization in the image plan} & g = 8. \end{cases} \tag{38}$$

Thus, the image sizes are 256×256 pixels, and the Fisher matrix is 54×54 in size. The accumulated number of photoevents approximately corresponds to a 1-s exposure of a 7^m star for a 1000 Å-wide spectral range. Figure 1 shows the image of the pointlike source in the telescope focal plane, and Fig. 2 presents the spectrum and eigenvectors $\{v_k\}$ of the Fisher matrix (the components of vectors $\{v_k\}$ are ≤ 1 in magnitude). The shifted [according to (21)] numbering of coefficients $\{\alpha_l\}$ and $\{a_j\}$ should be borne in mind here.

As we see from Fig. 2a, the spectrum of I descends moderately steeply up to the 30th coefficient ($\lambda_1/\lambda_{30} \simeq 2.2$), but then an abrupt cutoff whose value is determined by a compute zero occurs. This implies that the inverse problem is unstable. Based on the in-focus pattern, we can estimate only the first principal component $p_1 - p_{30}$, while the higher principal components cannot be recovered in principle. The amplitude of individual types of aberrations of the Zernike series can be estimated from different principal components, but it should be kept in mind that the estimation accuracy in this case may decrease appreciably. Some coefficients, primarily those of axisymmetric aberrations, remain unknown. This result might be expected in advance, because the contributions of individual aberrations of the above type are difficult to separate by the appearance of the symmetrically blurred image.

As for the eigenvectors of I, the appearance of v_1 in Fig. 2b leads us to conclude that the coefficients with $l = 1, 7$ ($j = 2, 8$) enter into the most reliable principal component with the largest (in absolute value) weight. Turning to (12), we see that these numbers correspond to a wavefront tilt and a third-order coma. The reason for combining these aberrations is that they both contain the factor $\cos\theta$. A similar combination with $j = 3$, 7 and with $\sin\theta$ is the next in recovery accuracy. The combination with $j = 9$, 19 follows next; this is a triangular fifth- and seventh-order coma with $\sin 3\theta$. Note that the accuracy of calculating the higher (in number) eigenvectors, as well as the corresponding eigenvalues, is rather low.

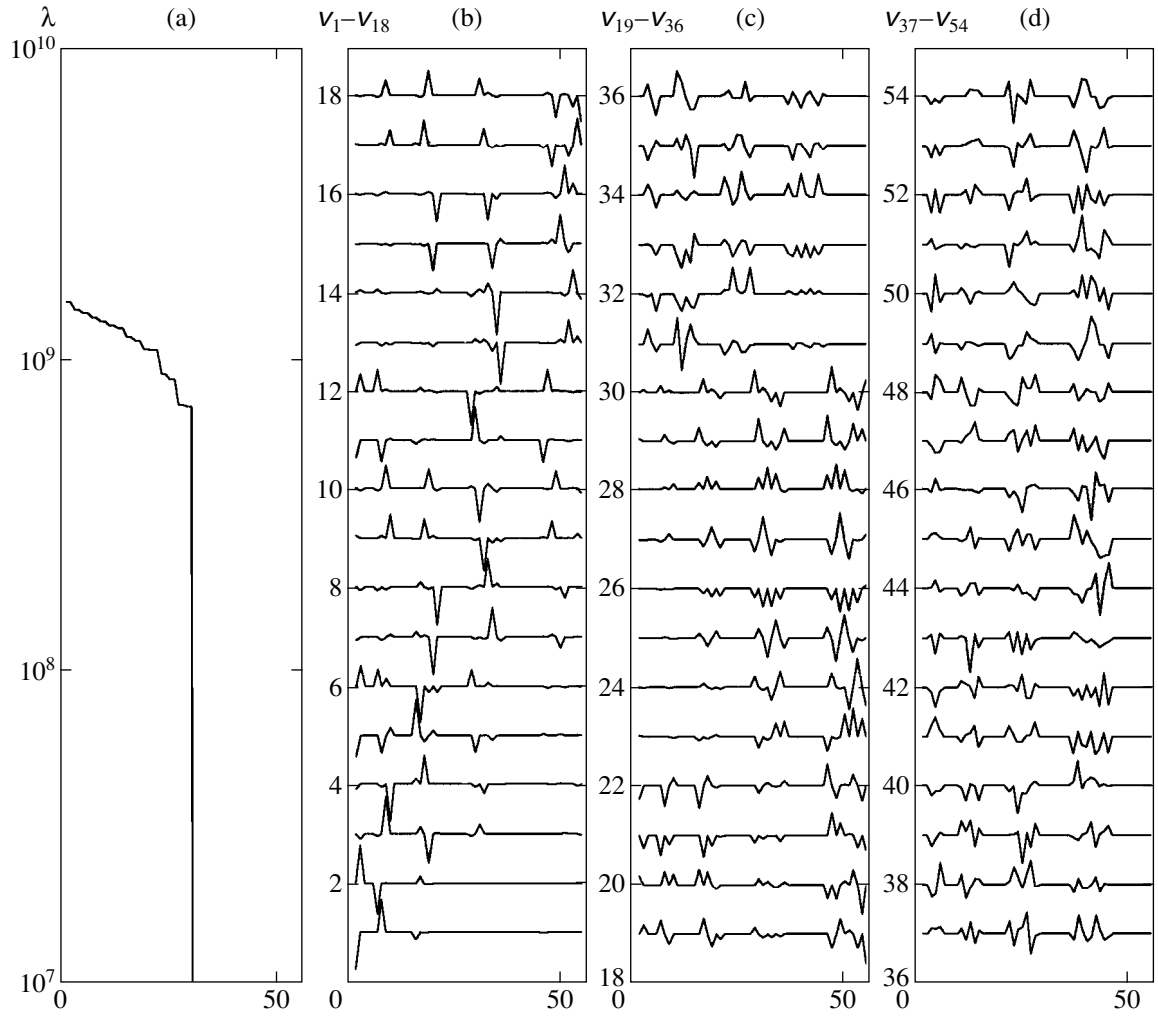

Fig. 2. Spectrum (a) and eigenvectors (b–d) of the Fisher matrix for the image in Fig. 1. (a) The component number of the corresponding vector is along the *X* axis, and the eigenvalues λ_k are along the *Y* axis; (b–d) vector numbers. The scale was chosen so that the separation between the successive plots for v_k was 1.

Let us consider the changes that arise for an out-of-focus plane of observation, for example, for δz = +5.0 mm: As before, the telescope is assumed to be ideal (Figs. 3 and 4). The spectrum of *I* changed radically: it covers a mere one and a half orders of magnitude ($\lambda_1/\lambda_{54} \simeq 30$), implying that the inverse problem became stable (in particular, well-conditioned). In this case, the stability of the inverse problem is quite understandable: Out-of-focus images allow many types of phase errors to be localized on the pupil fairly reliably (see also [10]). However, the in-focus pattern may be preferred regarding some types of aberration.

The eigenvectors of the Fisher matrix for out-of-focus images suggest a significant separation of aberrations of different types. For example, p_1 and p_2 give mainly information about the Zernike terms with $j = 36$, 35, which are proportional to $\rho^7\cos 7\theta$ and $\rho^7\sin 7\theta$, respectively. If we are interested, for example, in the third-order spherical aberration ($j = 11$), it dominates in p_{28}, although there are also traces of the defocus ($j = 4$) and a fifth-order ($j = 22$) and seventh-order ($j = 37$) spherical aberration in this component. The required aberration can be completely isolated by using p_{11} and similar principal components which include the same types of aberrations with different weights. Other aberrations of the optical system can be recovered in a similar way.

Finally, we turn to the case where the optical system is imperfect. Figure 5 shows the out-of-focus star image for the parameters specified in (38), the defocus δz = +5.0, and the following four nonzero coefficients of the Zernike series:

$$a_7 = 0.05, \quad a_{11} = 0.10, \quad a_{45} = 0.03, \quad a_{55} = -0.03. \tag{39}$$

Recall that the aberrations are in fractions of the wavelength. When choosing the numbers of the nonzero coefficients, we had in mind adaptive optics, where not only classical aberrations but also high-frequency harmonics were represented.

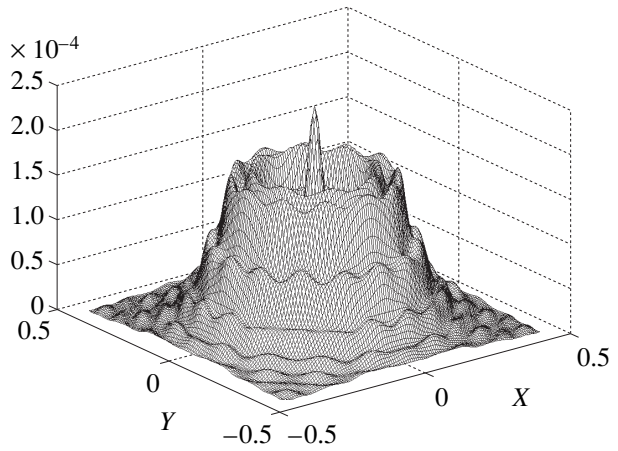

Fig. 3. Image of a point source formed by an ideal telescope when the plane of observations is shifted by 5 mm along the optical axis. The *X* and *Y* coordinates are in arcseconds.

Information about the spectrum and eigenvectors of the Fisher matrix is given in Fig. 6. We see that the inverse problem remained stable ($\lambda_1/\lambda_{54} \simeq 22$), so the phase can be retrieved reliably. At the same time, a comparison of Figs. 4b-4d with the corresponding Figs. 6b–6d shows that the cross-correlations between the estimates of aberrations of different types in this case strengthened. For example, the first principal component contains a linear combination of the ninth-order aberrations with j = 20, 32, which are proportional to $\rho^5\sin 5\theta$. The strengthening of the correlation between the statistical estimates of the coefficients of the Zernike series with increasing aberrations suggests that this series does not adequately describe the problem to be solved.

5. PHASE RETRIEVAL BY THE MAXIMUM-LIKELIHOOD METHOD

Any method of estimating the object (or, in other words, solving the inverse problem) is based on the distribution density $f(y|\alpha)$ assumed in the model. This circumstance is expressed most clearly in the *maximum-likelihood* (ML) *method* introduced by Fisher [40]. For the observed image realization y_0, the corresponding ML estimate of the vector parameter $\hat{\alpha}(y_0)$ is defined as

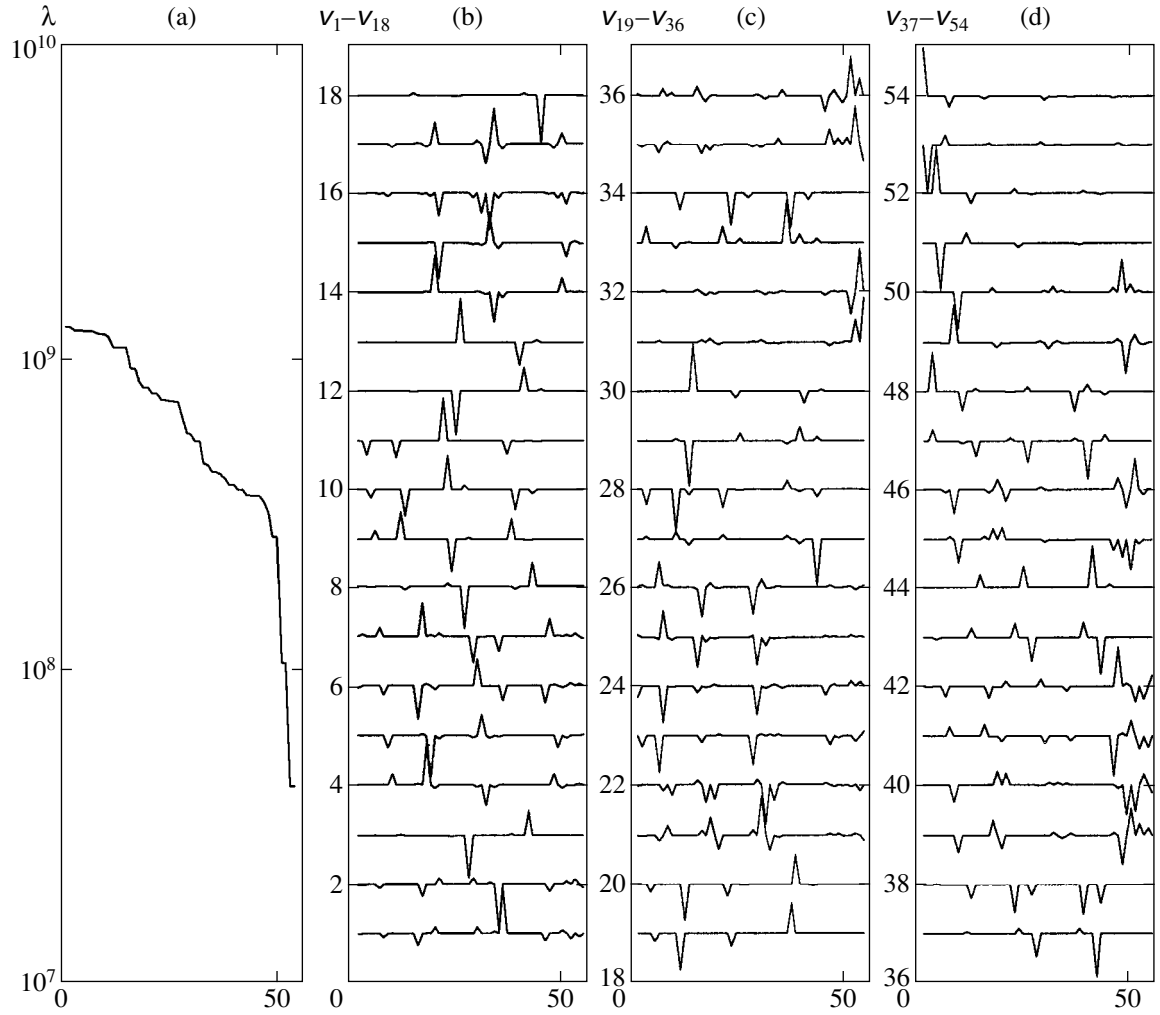

Fig. 4. (a) Spectrum and (b–d) eigenvectors of the Fisher matrix for the image in Fig. 3.

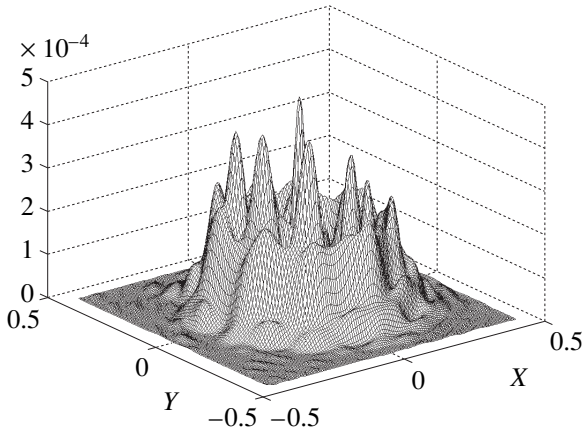

Fig. 5. Image of a point source formed by a telescope with the aberrations (39) when the plane of observations is shifted by 5 mm along the optical axis. The X and Y coordinates are in arcseconds.

the point in space $(\alpha_1, \ldots, \alpha_{n-1})$ that gives a maximum of the likelihood function $f(y_0|\alpha)$ or, equivalently, a minimum of the information (17),

$$\hat{\alpha}(y_0) \equiv \operatorname{argmin}_{\alpha} J(y_0|\alpha). \quad (40)$$

After $\hat{\alpha}(y_0)$ has been calculated, the ML estimates of coefficients $a_2, a_3, \ldots, a_n$ can be determined from formulas (21).

For one or a few parameters, their ML estimates almost always have optimal properties, particularly in the asymptotic region [37]. However, when a large number of parameters are estimated, quite often we encounter a completely different state of affairs: The ML estimate becomes unstable. The reasons for this phenomenon were previously considered in detail [19, 20]; in the long run, the validity of the ML method is determined by the spectrum of the Fisher information matrix for the inverse problem in question.

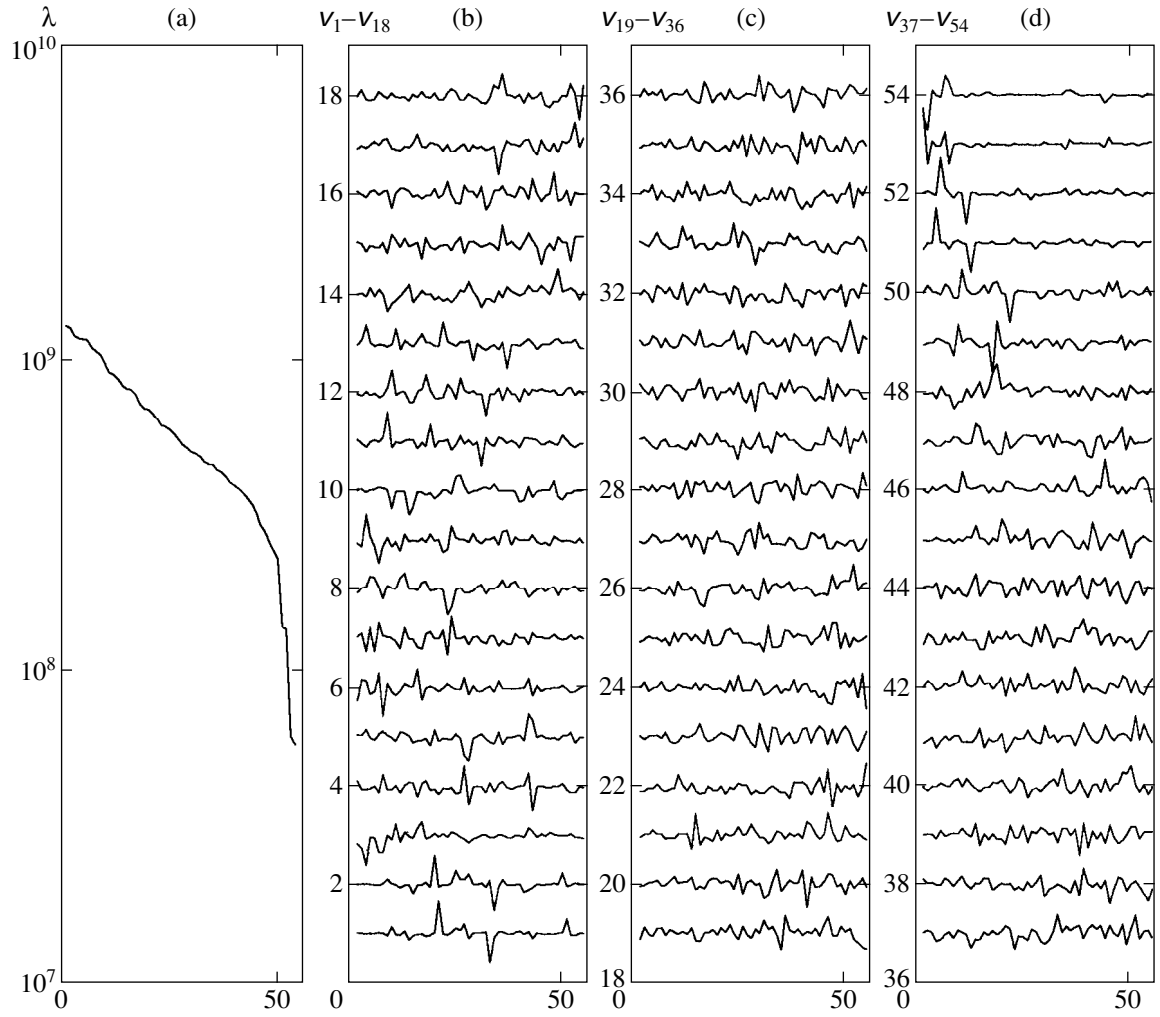

Fig. 6. (a) Spectrum and (b–d) eigenvectors of the Fisher matrix for the image in Fig. 5.

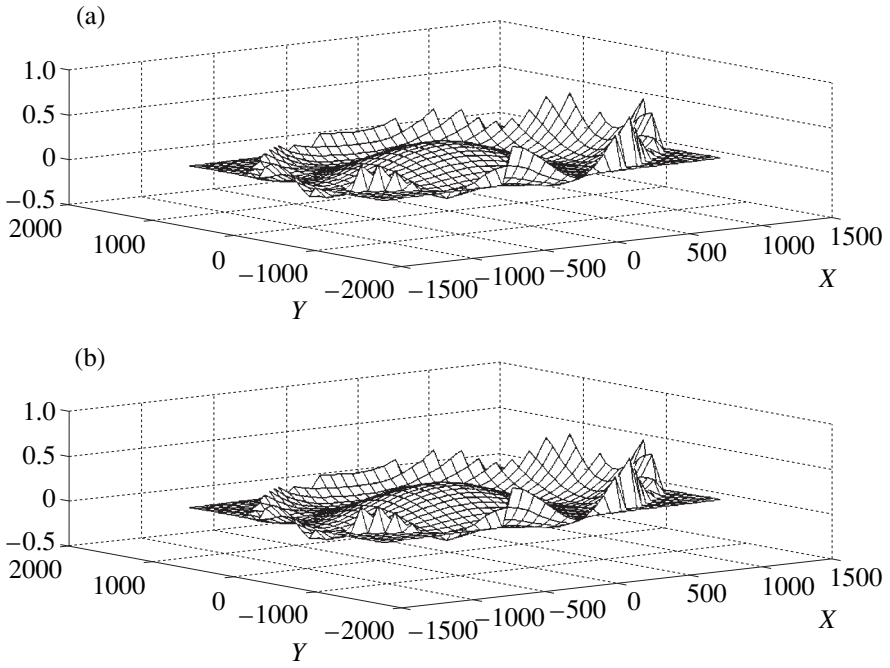

Fig. 7. (a) Initial phase function and (b) its maximum-likehood estimate.

An analysis of model cases of the inverse problem in Sect. 4 shows that, when out-of-focus images are considered, the inverse problem is stable. For this reason, a relatively simple inversion method can be used; as an example, we restrict ourselves to obtaining the ML estimate $\hat{a}$ of the coefficients of aberration decomposition into Zernike polynomials. The minimum in (40) was sought by one of the efficient optimization methods, for example, the quasi-Newton algorithm, Davidon–Fletcher–Powell's or Nelder–Mead's method (see, e.g., [41]). The procedure can be speeded up by using an analytical representation for the gradient of Poissonian information,

$$\frac{\partial}{\partial \alpha_l} J(\nu|\alpha) = \sum_{j=1}^{R} (\nu_j/q_j - 1) H_{jl}, \quad l = 1, 2, \ldots, n-1. \tag{41}$$

It should be noted that the function minimized in the phase problem takes a very complex form in multidimensional space, including "ravines" and local minima. For this reason, due attention should be paid to choosing an efficient algorithm and testing the reliability of the global minimum found [42].

For the model calculations, we took the values (39) as the nonzero coefficients of aberrations of the initial wavefront at the total number of decomposition terms $n = 55$. The corresponding out-of-focus image is shown in Fig. 5; this pattern was used to obtain the ML estimates of the Zernike coefficients. In this case, the deviation of the estimates of the Zernike coefficients from their true values did not exceed 10^{-4}. Figure 7 shows the initial wavefront and the result of its restoration from the observed image intensity. Not only classical aberrations but also the Zernike high-frequency terms are seen to be restored.

6. CONCLUDING REMARKS

In recent years, various applications of the probability theory have increasingly used the Karhunen–Loeve decomposition into eigenvectors of the covariance function of the random process under consideration [43–45]. The advantages of this decomposition primarily stem from the fact that the coefficients of the derived series are statistically uncorrelated with each other. In other words, each of the succeeding coefficients carries information about the process that is independent of the preceding segment of the series, and this information accrues (in the linear approximation) most effectively. The Karhunen–Loeve series is naturally distinguished from a host of other possible decompositions into orthonormal functions.

The decomposition of the Fisher matrix into eigenvectors [19, 20] plays a similar role in the theory of inverse problems. Indeed, for a linear probabilistic model of observational-data formation, the covariance matrix Ω of the inverse (or maximum-likelihood) solution is approximately equal to I^{-1}; the preceding assertion follows from the fact that any matrix and its inverse matrix have the same set of eigenvectors. The same relationship between I and Ω also approximately holds for more complicated models of data formation; the Fisher matrix naturally includes information about all details of the model (for example, about photon noise

for image formation). The coefficients $\{p_j\}$ of the corresponding decomposition given by (37), the *principal components of the inverse estimate*, are therefore of fundamental importance in obtaining an optimal inverse solution. The variance of the principal components, which determines the accuracy of the inverse solution, is simply related to the spectrum of the Fisher matrix.

Returning to the inverse problems of wave optics, it should be noted that, for all their convenience, the Zernike polynomials have not been naturally distinguished by the problem itself. Fortunately, as was shown by Roddier *et al.* [45], the difference between the Zernike polynomials and the Karhunen-Loeve functions is small when the wavefront perturbations are analyzed. It should, nevertheless, be borne in mind that this situation does not persist under more complicated observing conditions, in particular, when noise plays a major role.

Note that the concept of condition number c $c \equiv \lambda_{max}/\lambda_{min}$ is not adequate to judge whether the solution of the inverse problem is reliable. If $c \gg 1$, then the problem is considered ill-conditioned. However, a large c may result from the relative smallness of only the "tail" in the spectrum of the Fisher matrix, whereas most of the principal components contain valuable information. This situation takes place, for example, for the phase problem when in-focus images are analyzed (see Sect. 5). For this reason, we use the concept of *stability* of the inverse problem by associating it with the appearance of the entire spectrum of the Fisher matrix rather than with its two extreme values.

Finally, note that images for various defocuses should be invoked for a more reliable phase retrieval; the corresponding patterns can be analyzed individually and simultaneously. Here, we cannot dwell on this practically important subject.

ACKNOWLEDGMENTS

I am grateful to V.V. Biryukov and P.A. Jansson for helpful discussions of the problems concerned. This study was supported by the Russian Foundation for Basic Research (project no. 96-02-17296a).

REFERENCES

1. J. W. Goodman, *Statistical Optics* (Wiley-Interscience, New York, 1985; Mir, Moscow, 1988).
2. G. I. Vasilenko and A. M. Taratorin, *Image Restoration* (Radio i Svyaz', Moscow, 1986).
3. A. V. Goncharskiĭ, V. V. Popov, and V. V. Stepanov, *An Introduction to Computer Optics* (Mosk. Gos. Univ., Moscow, 1991).
4. P. A. Jansson, *Deconvolution of Images and Spectra* (Academic, San Diego, 1997).
5. C. van Schooneveld, *Image Formation from Coherence Functions in Astronomy* in *Proceedings of IAU Colloquium* (Dordrecht, Reidel, 1979; Mir, Moscow, 1982), No. 49.
6. A. A. Tokovinin, *Stellar Interferometers* (Nauka, Moscow, 1988).
7. C. J. Burrows, J. A. Holtzman, S. M. Faber, *et al.*, Astrophys. J. Lett. **369**, L21 (1991).
8. A. G. Tescher, Proc. SPIE **1567** (1991).
9. C. Roddier and F. Roddier, Appl. Opt. **32**, 2992 (1993).
10. J. R. Fienup, J. C. Marron, T. J. Schulz, *et al.*, Appl. Opt. **32**, 1747 (1993).
11. R. J. Hanisch and R. L. White, Eds., *The Restoration of HST Images and Spectra-II* (NASA, 1994).
12. R. G. Lyon, J. E. Dorband, and J. M. Hollis, Appl. Opt. **36**, 1752 (1997).
13. R. W. Gerchberg and W. O. Saxton, Optik **35**, 237 (1972).
14. J. R. Fienup, Opt. Lett. **3**, 27 (1978).
15. J. R. Fienup, Opt. Eng. **18**, 529 (1979).
16. J. R. Fienup, Appl. Opt. **21**, 2758 (1982).
17. J. C. Dainty and J. R. Fienup, *Image Recovery: Theory and Application*, Ed. by H. Stark (Academic, New York, 1987), Chap. 7, p. 231.
18. V. Yu. Terebizh, Astron. Astrophys. Trans. **1**, 3 (1991).
19. V. Yu. Terebizh, Usp. Fiz. Nauk **165**, 143 (1995a).
20. V. Yu. Terebizh, Int. J. Imag. Syst. Technol. **6**, 358 (1995b).
21. M. Born and E. Wolf, *Principles of Optics* (Pergamon, Oxford, 1964).
22. S. N. Bezdid'ko, Opt.–Mekh. Prom. **9**, 58 (1974).
23. F. Zernike, Physica **1**, 689 (1934).
24. R. J. Noll, J. Opt. Soc. Amer. **66**, 207 (1976).
25. V. A. Kotel'nikov, in *Proceedings of All-Russia Conference on Technical Reconstruction of Communications and Weak-Current Industry* (Moscow, 1933).
26. C. Shannon, Bell Syst. Techn. J. **27**, 379, 623 (1948).
27. C. Shannon, Proc. IRE **37**, 10 (1949).
28. D. R. Cox, J. R. Statist. Soc. **B17**, 129 (1955).
29. L. Mandel, Proc. Phys. Soc. London **72**, 1037 (1958).
30. L. Mandel, Proc. Phys. Soc. London **74**, 233 (1959).
31. C. L. Mehta, *Progress in Optics*, Ed. by E. Wolf (North Holland, Amsterdam, 1970), Vol. 8, p. 373.
32. G. J. Troup, *Progress in Quantum Electronics*, Ed. by J. H. Sanders and S. Stenholm (Pergamon, Oxford, 1972), Vol. 2, Part 1, p. 1.
33. V. Yu. Terebizh, *Time Series Analysis in Astrophysics* (Nauka, Moscow, 1992).
34. D. L. Snyder, A. M. Hammoud, and R. L. White, J. Opt. Soc. Amer. A **10**, 1014 (1993).
35. R. A. Fisher, Phil. Trans. R. Soc. London A **222**, 309 (1922).
36. M. Kendall and A. Stewart, *The Advanced Theory of Statistics. Inference and Relationship* (Griffin, London, 1969; Nauka, Moscow, 1973).

37. A. A. Borovkov, *Mathematical Statistics* (Nauka, Moscow, 1984).
38. W. H. Press, S. A. Teukolsky, W. T. Vetterling, and B. P. Flannery, *Numerical Recipes* (Cambridge Univ., Cambridge, 1992).
39. W. U. Pratt, *Digital Image Processing* (Wiley, New York, 1978; Mir, Moscow, 1982).
40. R. A. Fisher, Messenger of Mathematics **41**, 150 (1912).
41. R. Fletcher, *Practical Methods of Optimization, vol. 1, Unconstrained Optimization* (Wiley, New York, 1980), Vol. 1.
42. J. R. Fienup and C. C. Wackerman, J. Opt. Soc. Amer. A **3**, 1897 (1986).
43. M. Loeve, *Probability Theory* (Van Nostrand, New York, 1963; Inostrannaya Literatura, Moscow, 1962).
44. A. K. Jain, *Fundamentals of Digital Image Processing* (Prentice-Hall, New Jersey, 1989).
45. F. Roddier, M. Northcott, and J. E. Graves, Publ. Astron. Soc. Pacif. **103**, 131 (1991).

Translated by V. Astakhov

Astronomy Letters, Vol. 26, No. 1, 2000, pp. 9–21. Translated from Pis'ma v Astronomicheskiĭ Zhurnal, Vol. 26, No. 1, 2000, pp. 13–26.

One Hundred Years of Observations of the Be Star HDE 245770 (the X-ray Binary A0535+26/V725 Tau): The End of an Active Phase?

V. M. Lyuty* and G. V. Zaĭtseva

Sternberg Astronomical Institute, Universitetskiĭ pr. 13, Moscow, 119899 Russia

Received April 29, 1999; in final form, July 20, 1999

Abstract—*UBV* observations of the X-ray binary system A0535+26/V725 Tau at the Crimean Station of the Sternberg Astronomical Institute in 1980–1998 are presented. Based on our and published data, we analyze the photometric history of the star from 1898. Over a period of 100 years, the star apparently showed all three activity phases (B, Be, Be-shell) of Be stars. We conclude that the X-ray activity of the object is attributable to the 1970–1997 outburst of the Be star due to envelope ejection. The star's colors during the minimum light of 1998 and its 1953–1956 colors (before the outburst) correspond to the spectral type B0–B1 at the color excesses $E_{B-V} = 0.74$ and $E_{U-B} = 0.48$, in agreement with the current spectral type O9.7. The minimum light of 1998 and the color excesses are used to determine the colors of the additional radiation, analyze their evolution during the 1973–1997 outburst, and refine the distance to the object (3 kpc). The colors of the additional radiation at maximum light of the star (1973–1980) match the colors of a hydrogen plasma with $T_e = 1.5 \times 10^4$ K which is optically thick in the Balmer continuum. The brightness decline corresponds to a decrease in the optical depth of the plasma; at $V \simeq 9\overset{m}{.}1$, it becomes optically thin in the Balmer continuum with $T_e = 10^4$ K and $N_e = 10^{10}$–10^{12} cm^{-3}. This conclusion is consistent with the model of a circumstellar envelope but is inconsistent with the existence of an accretion disk around the neutron star. All the additional radiation responsible for the optical variability is produced by a single source. The intensity of the Hα emission line at maximum light (1975–1980) is triple its intensity in 1987–1997, when quasi-periodic light fluctuations with $P \approx 1400^{\rm d}$ were observed [1]. At this time, the line intensity correlated with brightness. The Hα line was in absorption at the minimum of 1998, and, at present, the star's active phase appears to have ended. *© 2000 MAIK "Nauka/Interperiodica".*

INTRODUCTION

The transient X-ray source A0535+26, which was identified with a variable Be star that was subsequently designated as V725 Tau, has been extensively studied since April 1975, when the first of the so-called "giant" X-ray outbursts was recorded. This is believed to be a binary system with a neutron star, a pulsar with a period of 103 s and an orbital period of $111^{\rm d}$ (see the review article of Giovannelli and Graziati [2]). The orbit is highly eccentric, and X-ray outbursts are observed during periastron passage. The object belongs to massive X-ray binaries in which the primary is a star of spectral type O9e–B1e, luminosity class III–V, and mass 10–$20M_\odot$, while the secondary is a neutron star. In particular, the spectral type of the optical star in A0535+26/V725 Tau was estimated to be O9.7 IIIe [3]. The material that accretes onto the neutron star is mainly supplied through mass loss from a rapidly rotating Be star and stellar wind. Such systems are distinguished by long periods (up to several hundred days) and high orbital eccentricities, which appears to produce the phenomenon of a transient, flaring X-ray source (an X-ray outburst is observed during periastron passage). In contrast to the "standard" massive close (Cyg X-1-type) X-ray binaries, in which the optical star fills its Roche lobe, these systems were called Be/XR binaries.

The optical radiation of such a system is mainly produced by the Be star and the surrounding envelope. An accretion disk (AD) around the neutron star may also be a contributor. Gnedin *et al.* [4] were the first to have attempted to separate the additional (relative to the Be star) optical and infrared (*UBVRIJHK*) radiation and concluded that this radiation could be interpreted as the radiation of an AD whose parameters vary with time. Lyuty *et al.* [5] noticed that the object's X-ray activity was related to the global outburst of the Be star which began in late 1960s–early 1970s and reached a maximum in 1975, when the first of the three giant X-ray outbursts was observed. Such an outburst is attributable to a variable rate of mass loss from the Be star.

The luminous blue stars are known (see, e.g., [6]) to be variable in wide time and amplitude ranges. A moderate variability of $\Delta V \simeq 1^m$ is observed in most of these stars and is caused by the ejection of a dense envelope, which can be assumed to be the stellar pseudophotosphere. In this case, the bolometric luminosity is constant, but the pseudophotospheric temperature

* e-mail: lyuty@sai.crimea.ua

decreases and the radius increases. Since the star rapidly rotates (hundreds of km s^{-1} on the equator), a disklike, rather than spherically symmetric envelope, is formed.

Clark *et al.* [1, 7] investigated the spectroscopic and photometric variability of V725 Tau by using the 1983–1997 observations and showed that the optical variability was apparently attributable to a disklike envelope around the OB star (circumstellar disk), which is optically thin in *UBV*. The light variations are caused by variations of the emission measure in the circumstellar disk that emits by the free-free and bound-free mechanisms. There is no evidence for the existence of a second variable source (AD). A transient AD appears to be formed around the neutron star during giant outbursts [8]. In particular, the existence of an AD during the giant outburst of 1994 was proven [9]. However, the contribution of the AD to the optical luminosity of V725 Tau is very small and apparently does not exceed a few percent.

In this paper, we present our *UBV* observations of the star at the Crimean Station of the Sternberg Astronomical Institute (SAI) in 1980–1998 and analyze its photometric behavior over a period of 100 years and the color characteristics of the additional (relative to the Be star) radiation responsible for the optical variability.

OBSERVATIONS

Our observations began in the spring of 1983 and were carried out with a photon-counting *UBV* photometer attached to the 60-m telescope of the Crimean Station of the SAI (pos. Nauchnyi). The instrumental photometric system was very close to Johnson's standard photometric system, as suggested by the mean transformation coefficients that were determined during six observing seasons in 1967–1990 from observations of standard stars in the Pleiades, Praesepe, and IC 4665 open clusters: $k_1 = -0.045 \pm 0.019$, $k_2 = 0.999 \pm 0.012$, $k_3 = 1.013 \pm 0.014$ [the corresponding formulas are $\Delta V = \Delta v + k_1\Delta(B–V)$, $\Delta(B–V) = k_2\Delta(b–v)$, and $\Delta(U–B) = k_3\Delta(u–b)$. As we see, k_1 is close to zero, while k_2 and k_3 are close to unity.

As the local standard, we used star "e" from [10], in which the following magnitudes are given for it: $V = 10\overset{m}{.}54 \pm 0\overset{m}{.}03$, $B–V = +0\overset{m}{.}45 \pm 0\overset{m}{.}03$, and $U–B = +0\overset{m}{.}19 \pm 0\overset{m}{.}05$. This comparison star was also used by Rössiger [11], who obtained its magnitudes similar to those of Lenouvel and Flogèr [10]: $V = 10\overset{m}{.}54$, $B–V = +0\overset{m}{.}45$, $U–B = +0\overset{m}{.}22$. Our measurements in 1984 and 1997 yielded the same magnitudes as those obtained by Lenouvel and Flogèr [10] but with a higher accuracy: $V = 10\overset{m}{.}53 \pm 0\overset{m}{.}01$, $B–V = +0\overset{m}{.}45 \pm 0\overset{m}{.}01$, and $U–B = +0\overset{m}{.}18 \pm 0\overset{m}{.}02$. As we see, the measurements of different authors over a period of 40 years yield the same magnitudes. Only the measurements by Walker in 1958 [11] differ markedly (up to $0\overset{m}{.}1$) from them; they are most likely erroneous.

Some of our observations have already been published [4, 5]; here, we present only the observations after 1988, as well as the observations that were performed by A.A. Aslanov in 1980 at the same site and with the same telescope and photometer and that he put at our disposal (see the table). Since Aslanov used the comparison star BD+26°876, we had to determine its magnitudes by referencing to the same standard (SA 48-3) which we used to determine the magnitudes of star "e" and reduce Aslanov's observations to our comparison star. Thus, Aslanov's observations constitute a single, homogeneous series with our measurements but are separated from ours by a period of three years and overlap in time with the observations by other authors. In our analysis, we therefore used Aslanov's observations together with published data.

LIGHT AND COLOR CURVES

Portions of the light and color curves for the object have been published at different times. The most complete curves for a long time interval are given in [1, 5, 7]. We now have an opportunity to present the photoelectric light and color curves for A0535+26/V725 over a period of 25 years, from 1973 until 1998. The first systematic *UBV* observations of the object, which was not known at that time as an X-ray source, were initiated by Rössiger [11]. In their previous study, Rössiger and Wenzel [12], who used this star as one of the comparison stars for the observations of RR Tau, noticed its weak variability. These observations, together with the observations by De Loor *et al.* [13] and Aslanov (see the table), are the main photometric *UBV* data for V725 Tau before 1983. We did not use the observations of other authors after 1983, because, first, they could violate the homogeneity of the series (see [5]) and, second, they are rather few in number compared to our observations, while our observations represent satisfactorily the star's variability in 1983–1998.

Since here we are primarily interested in the global variability of the object, while the star also exhibits a rapid variability with a significant amplitude, up to $0\overset{m}{.}1$ in two or three days and up to $0\overset{m}{.}05$ during the night, we averaged the measurements close in time and/or brightness. These average magnitudes and colors are shown in Fig. 1, where the arrows mark the times of giant X-ray outbursts (we have in mind only the outbursts observed in the intermediate energy band 2–10 keV). Occasionally, the outburst in April 1989 is regarded as a giant outburst [2], but its spectrum was very hard: from 0.6 Crab in the band 2–6 keV to 4.3 Crab in the band 16–26 keV [14]. In the intermediate energy band 2–10 keV, it should apparently be considered "normal." This outburst is marked in Fig. 1 by the dashed arrow.

Several features can be noted in the behavior of the star's light and color during 25 years (see Fig. 1):

(1) On the average, the brightness declined from $8^m.8$–$8^m.9$ to $9^m.45$; the *B–V* color index decreased, while *U–B* first decreased but after 1995 began to increase.

(2) Three brightness states can be distinguished: (i) the high brightness in 1973–1981, the colors do not correlate with brightness; (ii) the pulsations in 1983–1995 at a nearly constant mean brightness, *B–V* varies in antiphase with phase with brightness, and *U–B* does not correlate with brightness; and (iii) the brightness decline after 1995 with a small outburst in 1996; *B–V* also anticorrelates with brightness, while *U–B* anticorrelates with *B–V*.

(3) The transitions between these states roughly coincide in time with giant outbursts; before the 1975 outburst, the *V* brightness was constant, while the colors varied appreciably; after the 1980 outburst, the brightness declined by more than $0^m.2$, but the color indices were nearly constant; after the 1994 outburst, the colors varied in antiphase—the star became bluer in *B–V* but redder in *U–B*.

In the fall of 1997, the star's brightness had declined to the level of the 1950s for the first time since 1973 and has remained approximately at this level to the present day (late 1998), undergoing only short-term fluctuations with an amplitude up to $0^m.1$. The dereddened colors correspond to a B0 star (see below for details on the colors). The lowest brightness was recorded in 1998, at which the colors $B–V = +0.425$ and $U–B = –0.604$ turned out to be similar to the colors in the mid-1950s, before the outburst [15, 10]: $B–V = +0.45$ and $+0.46$, $U–B = –0.54$ and $–0.53$, respectively.

PHOTOMETRIC HISTORY OF THE STAR

For the subsequent analysis, it is of interest to trace the photometric history of the star. Stier and Liller [16] gave yearly means of the Harvard photographic observations since 1898 and noted that the fading in 1940–1955 may have been a real effect. Rössiger [17] gave the Sonneberg photographic observations of the star since 1930. The Harvard and Sonneberg observations overlap in time, but their means differ markedly in the same years. For the calibration, we used the photoelectric observations by Hiltner [15] and Lenouvel and Flogèr [10] by assuming $B_{pg} = m_{pg} – 0.05$ for the Sonneberg observations and $B_{pg} = m_{pg} + 0.18$ for the Harvard observations before 1970 (the Harvard observations in 1973 and 1974 have a zero correction, which may be explained by the already commenced outburst of the star).

The archived photographic observations reduced in this way, together with the seasonally averaged photoelectric data, are shown in Fig. 2 and give an idea of the star's photometric behavior over a period of 100 years. The secular brightness decline from 1898 until 1950 is particularly noteworthy. The minimum in 1945–1949 is real—it is confirmed by the Sonneberg data. It is unlikely that the rapid (of the order of a year) fluctuations are real: first, the amplitude of these fluctuations is within the accuracy of photographic photometry, and, second, the Harvard and Sonneberg data disagree. In particular, the "outburst" of 1933 as inferred from the Harvard data is in conflict with the Sonneberg data.

In 1950–1965, the star was in quiescence; its brightness was at the mean level of $B = 9^m.83$ (indicated by the dashed line in Fig. 2), and then a fairly rapid brightness rise to the maximum of 1975–1980 began. We clearly see in Fig. 2 that the giant outbursts are not accidental but are associated with certain features of the light curve. The first outburst in 1975 occurred after some brightness level near the maximum was reached (maximum in *V*); the second outburst (1980) occurred before an abrupt brightness decline, after which quasi-periodic (~1400 days) fluctuations [7] set in at a nearly constant mean level; and after the third outburst (1994), the amplitude of these fluctuations abruptly decreased (the maximum of 1996 agrees with a quasi-period of 1400 days), and the brightness declined to the 1950–1965 level in 1997–1998 and below this level in the fall of 1998. The filled square in Fig. 2 marks *minimum minimorum*, the lowest brightness for the entire period of photoelectric observations, which was observed in the fall of 1998. It may well be that the same minimum as that in 1945–1949 will be observed in the next several years.

Thus, at least two different states of the star were observed during the century: quiescence (1898–1965) and an outburst—an active phase (1970–1997) with the amplitude $\Delta V = 0^m.55$. This behavior is characteristic of Be stars with a moderate variability and is explained by the ejection of an envelope which produces a pseudophotosphere [6]. In this case, the outburst amplitude is determined by a change in the mass-loss rate $\Delta \log \dot{M} \approx –0.3\Delta V$. The bolometric luminosity is nearly constant, the pseudophotospheric temperature decreases compared to the photosphere of the Be star, and its radius increases.

ADDITIONAL RADIATION

Mean Color Indices

To elucidate the nature of the optical variability in A0535+26/V725 Tau, it is first necessary to separate the additional (relative to the Be star) radiation and determine its characteristics. For this purpose, the intrinsic *UBV* magnitudes of the star must be known. We could take the 1953–1956 magnitudes as the main brightness, but the star's mean brightness in the fall of 1997 declined below this level. In the fall of 1998, we managed to record the minimum brightness in all

Photoelectric observations of A0536+26/V725 Tau in 1980 and 1988–1998

JD 2400000+	*V*	*B–V*	*U–B*	JD 2400000+	*V*	*B–V*	*U–B*
44254.526	8.87	0.54	–0.60	48158.519	9.311	0.415	–0.670
44257.334	8.86	0.56	–0.65	48158.562	9.307	0.421	–0.678
44261.217	8.864	0.536	–0.568	48164.570	9.320	0.430	–0.655
44488.560	8.878	0.562	–0.61	48176.523	9.217	0.460	–0.656
44489.555	8.868	0.552	–0.61	48188.519	9.286	0.433	–0.694
44490.563	8.863	0.567	–0.63	48189.452	9.286	0.447	–0.690
44493.557	8.86	0.56	–0.55	48211.404	9.218	0.464	–0.696
44494.576	8.88	0.57	–0.62	48211.417	9.218	0.468	–0.684
44589.515	8.88	0.57	–0.625	48244.268	9.295	0.447	–0.677
44590.401	8.89	0.56	–0.69	48251.265	9.308	0.424	–0.678
44599.401	8.93	0.56	–0.72	48251.277	9.305	0.431	–0.672
44600.469	8.88	0.60	–0.72	48252.233	9.275	0.431	–0.718
47417.559	9.140	0.475	–0.645	48272.206	9.321	0.424	–0.658
47418.570	9.110	0.491	–0.666	48274.222	9.317	0.428	–0.678
47419.554	9.090	0.509	–0.666	48294.240	9.251	0.451	–0.704
47420.577	9.092	0.497	–0.670	48295.291	9.257	0.452	–0.673
47439.578	9.127	0.499	–0.669	48325.251	9.157	0.477	–0.672
47449.542	9.093	0.502	–0.638	48505.565	9.107	0.513	–0.689
47450.574	9.091	0.492	–0.667	48508.573	9.112	0.496	–0.704
47451.554	9.077	0.489	–0.625	48509.575	9.114	0.503	–0.704
47536.342	9.001	0.516	–0.616	48515.568	9.088	0.516	–0.701
47540.322	9.005	0.515	–0.626	48516.573	9.084	0.519	–0.698
47569.266	8.994	0.515	–0.634	48525.585	9.056	0.525	–0.693
47586.256	8.982	0.523	–0.628	48534.592	9.104	0.501	–0.680
47607.248	8.974	0.531	–0.620	48539.565	9.118	0.524	–0.689
47624.263	9.014	0.543	–0.629	48540.472	9.122	0.501	–0.698
47834.615	9.231	0.459	–0.714	48541.557	9.112	0.511	–0.701
47835.485	9.240	0.437	–0.708	48543.512	9.108	0.503	–0.714
47836.445	9.219	0.478	–0.700	48546.451	9.131	0.508	–0.719
47837.557	9.251	0.462	–0.698	48566.406	9.136	0.517	–0.723
47838.472	9.286	0.451	–0.716	48576.472	9.155	0.506	–0.718
47855.450	9.227	0.441	–0.699	48603.369	9.218	0.472	–0.722
47861.394	9.238	0.459	–0.702	48856.520	9.005	0.511	–0.616
47943.228	9.098	0.491	–0.651	48861.526	8.988	0.513	–0.599
47943.235	9.102	0.491	–0.653	48864.526	8.975	0.524	–0.644
47944.225	9.115	0.486	–0.664	48865.496	8.993	0.513	–0.615
47944.238	9.113	0.486	–0.656	48866.498	8.991	0.536	–0.622
47946.224	9.132	0.491	–0.686	48870.500	9.011	0.510	–0.614
47946.230	9.125	0.490	–0.690	48893.502	8.989	0.528	–0.636
47948.233	9.134	0.487	–0.683	48894.598	8.989	0.509	–0.645
47966.260	9.162	0.486	–0.696	48916.497	8.981	0.529	–0.653
47968.269	9.150	0.484	–0.668	48930.521	9.008	0.526	–0.642
47970.258	9.172	0.466	–0.656	48958.345	9.004	0.527	–0.658
47971.276	9.178	0.489	–0.721	48959.335	8.993	0.528	–0.651
47981.243	9.157	0.487	–0.702	48961.315	8.988	0.538	–0.661
47984.291	9.139	0.461	–0.656	48992.222	9.096	0.508	–0.717
47986.286	9.155	0.479	–0.713	49002.212	9.090	0.523	–0.687
48151.565	9.348	0.421	–0.650	49006.254	9.093	0.517	–0.727

Table. (Contd.)

JD 2400000+	*V*	*B–V*	*U–B*	JD 2400000+	*V*	*B–V*	*U–B*
49031.317	9.092	0.487	–0.687	49973.552	9.333	0.435	–0.676
49059.275	9.092	0.507	–0.691	49973.559	9.343	0.424	–0.678
49062.282	9.108	0.517	–0.681	49998.462	9.339	0.420	–0.731
49245.553	9.024	0.524	–0.685	49998.468	9.342	0.426	–0.727
49246.561	9.033	0.532	–0.680	50002.435	9.279	0.442	–0.628
49248.540	9.028	0.534	–0.672	50002.446	9.273	0.447	–0.649
49251.571	9.038	0.535	–0.684	50002.452	9.278	0.440	–0.654
49253.557	9.049	0.528	–0.672	50004.424	9.254	0.457	–0.661
49255.568	9.041	0.524	–0.682	50006.436	9.283	0.440	–0.676
49273.544	9.029	0.528	–0.687	50007.423	9.294	0.444	–0.673
49274.597	9.017	0.518	–0.680	50007.434	9.294	0.443	–0.669
49359.261	9.187	0.476	–0.689	50008.418	9.309	0.441	–0.663
49360.323	9.193	0.475	–0.683	50008.430	9.312	0.437	–0.669
49373.411	9.198	0.474	–0.683	50009.392	9.308	0.430	–0.666
49381.228	9.224	0.459	–0.712	50009.404	9.310	0.439	–0.675
49393.293	9.241	0.458	–0.677	50010.431	9.332	0.429	–0.667
49394.297	9.244	0.455	–0.687	50010.444	9.326	0.436	–0.675
49400.322	9.254	0.441	–0.667	50014.394	9.334	0.442	–0.677
49401.290	9.249	0.454	–0.680	50014.406	9.332	0.435	–0.658
49407.217	9.274	0.472	–0.696	50015.428	9.348	0.439	–0.674
49412.260	9.273	0.442	–0.670	50015.442	9.359	0.428	–0.669
49438.231	9.182	0.480	–0.676	50047.385	9.326	0.434	–0.678
49442.244	9.158	0.486	–0.673	50047.396	9.313	0.449	–0.688
49444.254	9.181	0.475	–0.656	50048.408	9.307	0.448	–0.678
49450.252	9.147	0.484	–0.652	50048.442	9.293	0.439	–0.688
49457.244	9.183	0.490	–0.650	50048.455	9.288	0.443	–0.682
49596.538	9.300	0.450	–0.695	50064.386	9.293	0.436	–0.702
49600.543	9.324	0.462	–0.685	50064.418	9.286	0.439	–0.681
49601.518	9.335	0.434	–0.687	50064.431	9.288	0.442	–0.687
49609.556	9.344	0.433	–0.648	50093.468	9.233	0.463	–0.721
49611.562	9.336	0.442	–0.665	50093.475	9.195	0.465	–0.678
49629.460	9.292	0.431	–0.646	50095.488	9.206	0.469	–0.675
49630.552	9.295	0.435	–0.654	50102.287	9.255	0.454	–0.693
49640.540	9.242	0.457	–0.682	50106.298	9.249	0.452	–0.688
49653.418	9.297	0.446	–0.658	50108.194	9.278	0.458	–0.691
49654.470	9.300	0.450	–0.680	50115.299	9.267	0.437	–0.746
49658.379	9.320	0.448	–0.664	50116.369	9.265	0.435	–0.680
49663.462	9.316	0.440	–0.665	50117.193	9.271	0.441	–0.695
49665.460	9.335	0.420	–0.686	50121.303	9.236	0.454	–0.692
49692.367	9.296	0.426	–0.664	50133.343	9.250	0.465	–0.688
49716.333	9.302	0.435	–0.670	50139.215	9.241	0.472	–0.700
49717.328	9.314	0.434	–0.664	50139.240	9.251	0.459	–0.734
49737.238	9.315	0.445	–0.674	50155.221	9.273	0.476	–0.677
49751.351	9.313	0.461	–0.669	50170.298	9.28	0.50	–0.71
49771.230	9.353	0.420	–0.648	50177.258	9.231	0.449	–0.770
49772.232	9.364	0.417	–0.647	50178.256	9.259	0.439	–0.705
49778.244	9.361	0.422	–0.663	50311.535	9.157	0.508	–0.682
49782.232	9.382	0.414	–0.641	50361.468	9.119	0.497	–0.703
49820.270	9.306	0.446	–0.666	50362.516	9.161	0.500	–0.701
49820.278	9.311	0.442	–0.670	50373.542	9.157	0.497	–0.719
49825.262	9.286	0.470	–0.667	50373.558	9.152	0.504	–0.724

Table. (Contd.)

JD 2400000+	*V*	*B–V*	*U–B*	JD 2400000+	*V*	*B–V*	*U–B*
50392.604	9.230	0.469	–0.711	50760.384	9.451	0.412	–0.618
50393.595	9.226	0.477	–0.711	50760.415	9.462	0.398	–0.602
50393.607	9.232	0.485	–0.714	50761.426	9.448	0.406	–0.602
50395.513	9.224	0.480	–0.721	50762.423	9.443	0.405	–0.617
50395.537	9.229	0.476	–0.714	50762.458	9.436	0.407	–0.596
50397.469	9.227	0.461	–0.715	50783.483	9.445	0.403	–0.626
50400.465	9.240	0.473	–0.707	50793.310	9.455	0.413	–0.618
50400.498	9.229	0.470	–0.705	50802.348	9.418	0.407	–0.642
50402.553	9.228	0.483	–0.734	50817.248	9.472	0.396	–0.604
50403.452	9.244	0.463	–0.708	50818.227	9.469	0.398	–0.595
50405.392	9.199	0.479	–0.716	50827.296	9.477	0.409	–0.573
50408.510	9.257	0.455	–0.705	50863.287	9.442	0.402	–0.610
50478.279	9.295	0.434	–0.676	50867.304	9.465	0.413	–0.629
50484.356	9.304	0.442	–0.695	50868.246	9.470	0.404	–0.617
50487.282	9.344	0.430	–0.685	50875.291	9.452	0.407	–0.600
50491.308	9.350	0.434	–0.715	50920.246	9.449	0.417	–0.617
50491.320	9.356	0.427	–0.717	50920.252	9.456	0.420	–0.641
50504.347	9.357	0.424	–0.689	51044.551	9.461	0.419	–0.585
50505.324	9.370	0.425	–0.674	51046.548	9.472	0.445	–0.628
50509.303	9.354	0.430	–0.669	51052.553	9.399	0.442	–0.603
50510.324	9.350	0.429	–0.646	51054.551	9.475	0.417	–0.619
50510.338	9.357	0.425	–0.646	51061.544	9.458	0.421	–0.604
50519.296	9.376	0.419	–0.664	51074.569	9.448	0.414	–0.603
50519.308	9.369	0.423	–0.649	51074.582	9.460	0.405	–0.606
50521.322	9.377	0.425	–0.655	51075.513	9.430	0.422	–0.605
50526.313	9.363	0.426	–0.687	51075.521	9.437	0.414	–0.600
50689.558	9.390	0.416	–0.624	51081.504	9.441	0.417	–0.602
50689.565	9.387	0.419	–0.636	51081.517	9.461	0.395	–0.599
50690.552	9.344	0.425	–0.628	51088.536	9.477	0.410	–0.626
50696.562	9.414	0.406	–0.614	51103.549	9.452	0.400	–0.618
50699.566	9.404	0.412	–0.621	51103.555	9.492	0.388	–0.628
50704.560	9.425	0.412	–0.612	51104.479	9.473	0.403	–0.614
50726.502	9.421	0.390	–0.617	51104.492	9.472	0.403	–0.605
50730.460	9.445	0.405	–0.609	51105.405	9.472	0.404	–0.589
50748.452	9.441	0.405	–0.619	51110.382	9.475	0.407	–0.600
50748.463	9.450	0.398	–0.611	51111.443	9.475	0.408	–0.622
50751.592	9.444	0.398	–0.602	51112.482	9.468	0.401	–0.615
50753.459	9.430	0.401	–0.606	51112.493	9.464	0.412	–0.620
50753.470	9.444	0.394	–0.598	51137.350	9.408	0.418	–0.623
50754.586	9.446	0.402	–0.599	51141.364	9.448	0.394	–0.611
50754.618	9.440	0.408	–0.603	51141.369	9.438	0.415	–0.632
50755.447	9.440	0.397	–0.623	51163.284	9.418	0.412	–0.607
50755.474	9.440	0.408	–0.623	51163.288	9.413	0.410	–0.613
50758.430	9.435	0.413	–0.620	51164.382	9.448	0.414	–0.610
50758.455	9.431	0.415	–0.604	51164.386	9.443	0.418	–0.624
50759.428	9.449	0.405	–0.612	51175.276	9.466	0.408	–0.603
50759.454	9.446	0.401	–0.598	51175.281	9.472	0.408	–0.611

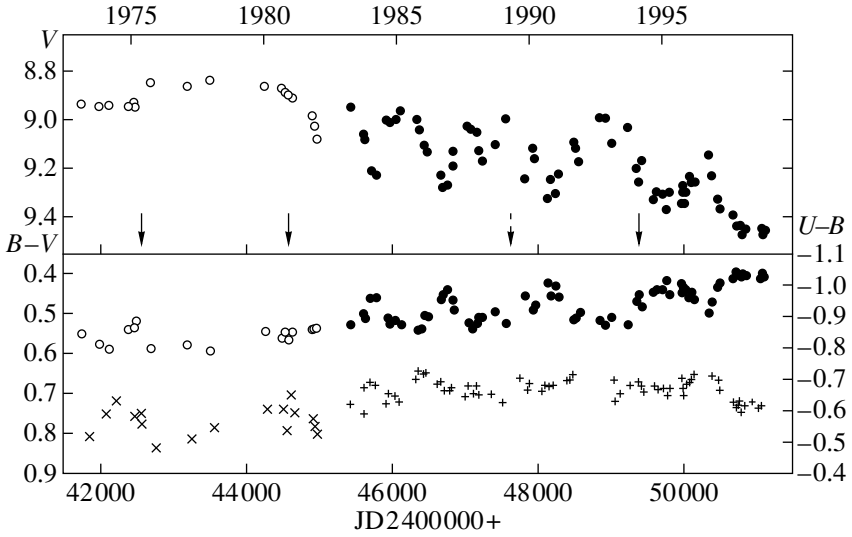

Fig. 1. Smoothed light and color curves of V725 Tau/A0535+26: the filled circles and pluses are our observations in 1983–1998, and the open circles and crosses are the observations of other authors before 1983 ([11, 35, 13]; Aslanov, see the table). The arrows mark the times of giant X-ray outbursts.

26 years of photoelectric observations (*minimum minimorum*). Apparently because of the rapid variability in the star, the minimum brightness in different bands was observed at different times and was found to be $V_{\min} = 9\overset{m}{.}492 \pm 0\overset{m}{.}005$, $B_{\min} = 9\overset{m}{.}917 \pm 0\overset{m}{.}005$, and $U_{\min} = 9\overset{m}{.}313 \pm 0\overset{m}{.}008$; the colors at this minimum were $B–V = 0\overset{m}{.}425$ and $U–B = -0\overset{m}{.}604$.

Next, the colors must be corrected for the reddening, which is rather large for V725 Tau. Margon *et al.* [18] and Wade and Oke [19] gave the color excesses $E_{B–V} = 0\overset{m}{.}8$ and $0\overset{m}{.}80$, respectively, while Giangrande *et al.* [3] obtained $E_{B–V} = 0\overset{m}{.}82 \pm 0\overset{m}{.}04$ and $E_{U–B} = 0\overset{m}{.}55 \pm 0\overset{m}{.}04$. However, these values appear to be slightly overestimated. Since the luminosity class of the star was found to be III–V, the dereddened colors must correspond to the main sequence. If the radiation from the B star proper is assumed to have been observed in 1953–1956 and in the fall of 1998 (*minimum minimorum*), then we obtain the reddenings $E_{B–V} = 0\overset{m}{.}74$ and $E_{U–B} = 0\overset{m}{.}48$. In this case, the color excess $E_{B–V}$ matches the value $0\overset{m}{.}75 \pm 0\overset{m}{.}05$ obtained from the 2200 Å interstellar band [2], while $E_{U–B}$ is slightly smaller than that followed from the normal reddening law. Below, we use our color excesses.

Thus, using the *minimum minimorum* magnitudes and our color excesses, we can derive the intrinsic colors of the additional radiation, which determined the outburst (active phase) of the star in 1973–1997 (see Fig. 2). In Fig. 3, the colors of the additional radiation are plotted against observed brightness. The $(B–V)_{\text{add}}$ color index monotonically decreases with declining brightness, while $(U–B)_{\text{add}}$ first decreases and then begins to increase. Comparing Fig. 3 with the light curve in Fig. 1, we see that the rise in brightness by $\Delta V \simeq 0\overset{m}{.}1$ from 1973 until 1977 and its subsequent decline after 1980 had no effect on the dependence in Fig. 3: The colors of the additional radiation depend only on brightness and not on the time when this brightness was reached. Only one data point deviates appreciably from the mean dependence of $(U–B)_{\text{add}}$ on V_{obs} (it corresponds to the minimum in late 1981–early 1982; see Figs. 1 and 2). It thus follows that all the additional radiation of 1973–1997 was attributable to a single source, apparently the circumstellar envelope (recall once again that here we do not consider rapid fluctuations of a relatively small amplitude, which may have a different nature).

Noteworthy is the large scatter for $(U–B)_{\text{add}}$, which is much larger than the observational errors and is mostly likely attributable to the Balmer emission jump.

Variability of the Hα Emission Line

If the additional radiation originates in the circumstellar envelope, then the intensity of emission lines, primarily Hα, must correlate with brightness. Such a correlation was actually found [1]: The Hα equivalent width as deduced from the 1987–1996 data correlates with *V* magnitude and *B–V* color at a 95% confidence level. It should be noted, however, that the continuum also varies; i.e., the equivalent width of the line reflects not only the variability of its intensity but also the continuum variability. Allowance for the continuum variability must therefore increase the confidence level of the correlation. In particular, if the continuum variability is taken into account, the correlation coefficient for

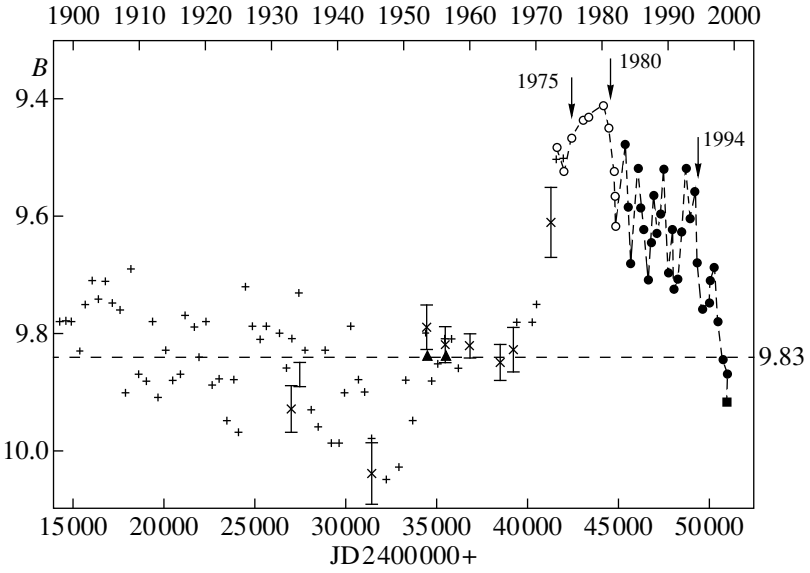

Fig. 2. Photometric history of the star from 1898: The pluses are the Harvard photographic observations [16], the crosses are the Sonneberg observations [17], the triangles are the photoelectric observations by Hiltner [15] and Lenouvel and Flogèr [10], and the square is the *minimum minimorum* of 1998; the remaining notation is the same as that in Fig. 1.

the 1987–1996 data increases by more than a factor of 1.5, and the confidence level increases to 99.9%.

The maximum brightness was observed in 1975–1980 (Fig. 2), and the first spectroscopic observations began approximately at the same time. We collected all published data on Hα equivalent-width determinations from 1975 until 1981 [13, 19–24] and reduced all values to the same continuum $V = 9\overset{m}{.}50$ by assuming that the continuum variations near Hα were proportional to those in *V*. This reduced equivalent width $EW_{\rm red}$ is proportional to the line intensity. When the dates of observation in *V* and in Hα did not coincide, we took the nearest date (but no farther than ten days) of *V* measurements with allowance for the variability pattern (Fig. 1). These results, together with the data of Clark *et al.* [1], which were also reduced to $V = 9\overset{m}{.}50$, are shown in the upper panel of Fig. 3. The open circles represent the 1975–1981 data, and the filled circles represent the 1987–1996 and 1997–1998 data [25].

Figure 3 shows not only a clear dependence of the Hα intensity on brightness but also a different behavior of this dependence at different times. In 1975–1981 (open circles) the Hα intensity was, on the average, triple that in 1987–1996. There is no significant correlation between line intensity and brightness. However, Aab [24] noted a considerable increase in *EW*(Hα) in January 1981, three months after the giant outburst of 1980, but it is hard to tell whether this increase is attributable to the outburst, because there were no spectroscopic observations during the outburst.

All 1987–1998 data show a good correlation with brightness; the correlation coefficient is $r = 0.70$. The Hα line in emission rather than in absorption corresponds to the lowest brightness in the fall of 1998 [25]. However, two different levels can be clearly identified in the 1987–1997 dependence: $EW_{\rm red}(\text{H}\alpha) = -14.6 \pm 0.9$ for $V = 9\overset{m}{.}0$–$9\overset{m}{.}15$, $\bar{V} = 9\overset{m}{.}11$ and $EW_{\rm red}(\text{H}\alpha) = -9.1 \pm 0.4$ for $V = 9\overset{m}{.}2$–$9\overset{m}{.}4$, $\bar{V} = 9\overset{m}{.}30$. The separation into these two levels depends not on time but only on brightness, which is apparently attributable to changes of the physical conditions in the envelope.

Nature of the Additional Radiation

We now try to determine the characteristics and nature of this additional radiation, at least qualitatively. Since, as was already pointed out above, we are concerned with the global variations, let us smooth the brightness dependences of the colors of the additional radiation (Fig. 3) by a moving average with the interval $\Delta V = 0\overset{m}{.}1$ and with a shift by half the interval (a slightly smaller shift of the interval was used for a brightness lower than $9\overset{m}{.}3$). The positions of these mean colors of the additional radiation responsible for the optical variability in the two-color (*U–B*)–(*B–V*) diagram are shown in Fig. 4, which also shows the radiation of a different nature: main-sequence stars, a blackbody, synchrotron radiation, and the radiation of an optically thin and optically thick (in the Balmer continuum) hydrogen plasma [26]. In order not to overload the figure, we give only the errors in *U–B*, because the errors in *B–V* are approximately a factor of 2 smaller; the numbers denote different apparent magnitudes. In addition, Fig. 4 shows the star's positions as determined from the

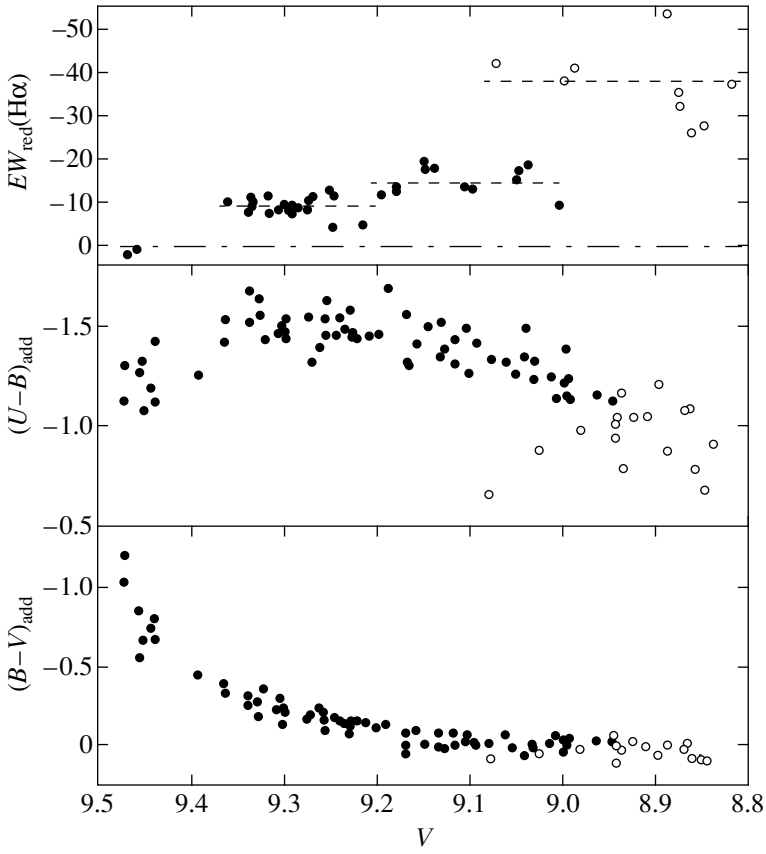

Fig. 3. Colors of the additional radiation in V725 Tau (the notation is the same as that in Fig. 1) and $EW(H\alpha)$ (in Angstroms) reduced to a single continuum level versus observed brightness. For $EW(H\alpha)$, the open and filled circles refer to 1975–1981 and 1987–1998, respectively.

1953–1956 observations before the outburst (triangles) and at *minimum minimorum* of 1998 (square). We clearly see that the additional radiation at maximum light $V_{obs} = 8\overset{m}{.}85$ corresponds best to an optically thick (in the Balmer continuum and in *UBV*) plasma with $T_e \sim 1.5 \times 10^4$ K (the colors are close to the blackbody line). It should be borne in mind, however, that the calculations were performed for a spherically symmetric envelope, while the envelope in our case is most likely disklike [7].

The brightness decline corresponds to a decrease of the optical depth both in *UBV* and in the Balmer continuum; the colors approach the lines for an optically thin (in the Balmer continuum) plasma with $T_e = 10^4$ K and $N_e = 10^{10}$–10^{12} cm^{-3}.The subsequent fading is apparently caused by a decrease of the optical depth in *UBV*. This behavior suggests the following natural scenario: An increase in the rate of mass loss from the Be star leads to the formation of a fairly dense envelope (pseudophotosphere), to a rise in brightness [6], and to the appearance of strong emission lines. In the course of time, the envelope begins to disperse, its optical depth decreases not only in the continuum but also in the lines, and the brightness and the emission-line intensity decrease. When the envelope becomes optically thin, it is no longer visible in *UBV* but apparently can still show up in the lines.

Indeed, at maximum light (1975–1980) the envelope was optically thick (see Figs. 2 and 4) and emitted radiation roughly as the stellar photosphere or, to be more precise, as a blackbody with $T_e \sim 12000$ K (pseudophotosphere) with a mean magnitude brighter than $V = 9\overset{m}{.}0$. The independence of EW_{red} on brightness can be explained by line saturation. The physical conditions in the envelope appear to have changed abruptly after the giant outburst of 1980: Quasi-periodic fluctuations set in at a nearly constant mean brightness $V = 9\overset{m}{.}15$, the envelope became optically thin in the Balmer continuum, and, in general, a dependence of the Hα intensity on brightness appeared. However, the two levels mentioned above, which may not accidentally correspond to the maximum and minimum of the 1400-day fluctuations, can be distinguished in this dependence. At a very low brightness (1998), the line is no longer in emission but in absorption: $EW_{red} \approx EW = 2.2$ Å (November 6, 1998). However, on November 9, 1998, a weak emission appeared on the red side, although, in

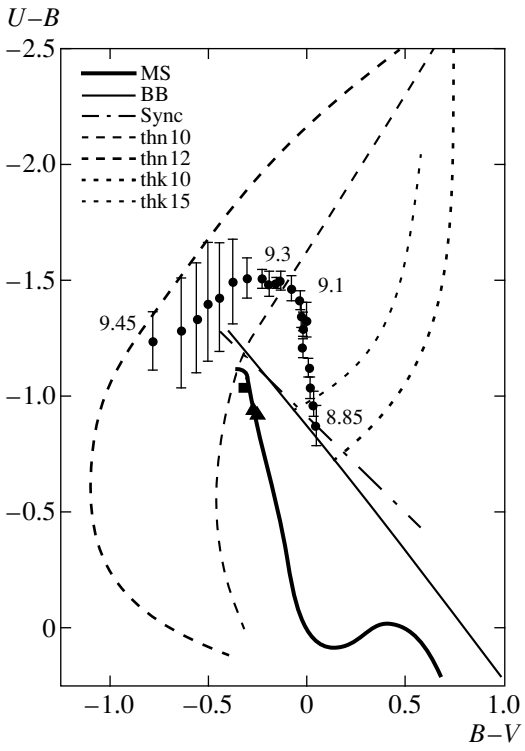

Fig. 4. Positions of the dereddened colors of the additional radiation in the (*U–B*)–(*B–V*) diagram; the observed brightness is indicated for some levels. Also shown are the positions of main-sequence (MS) stars, a blackbody (BB), synchrotron radiation (Sync), an optically thin (in the Balmer continuum) hydrogen plasma with $T_e = 10^4$ K and $N_e = 10^{10}$ (thn10) and $N_e = 10^{12}$ cm^{-3} (thn12), and an optically thick (in the Balmer continuum) plasma with $T_e = 10^4$ (thk10) and $T_e = 1.5 \times 10^4$ K (thk15). The filled triangles mark the star's positions in 1953–1956, and the filled square marks the *minimum minimorum* of 1998.

general, the line remained in absorption. The line FWHM (~1000 km s^{-1}) was essentially the same as that for the emission [25].

We now show that the additional radiation cannot be produced by the AD around the neutron star. An AD is known to emit radiation as a hot star with a temperature of (2–3) $\times$ 10^4 K [27]. Furthermore, the outer disk regions can be additionally heated by X-ray radiation; the energy release through heating can exceed the gravitational one [28, 29]. Since the AD as a plane figure emits maximum radiation in the direction perpendicular to its plane, it gives the largest contribution to the flux from the binary system at small orbital inclinations. Such a situation is observed in the system ScoX-1 [29], where the disk contribution to the optical flux is at a maximum, but the radiation from the AD, the star, and a hot spot cannot be separated.

However, there is a binary system (HZ Her/Her X-1) where we can separate the AD radiation and determine its color characteristics. Both optical and X-ray eclipses are observed in HZ Her. The optical flux from this system has three components: (i) a normal A5–F star, (ii) a hot spot on the star's side facing the X-ray pulsar, and (iii) an AD around the neutron star. Since the neutron-star size is much smaller than the size of a normal A–F star, at the beginning and at the end of an X-ray eclipse, we see the radiation from the star itself and from half the AD but do not see the hot spot, which gives the bulk of the optical flux. During a total eclipse (phase 0.0), we see the flux only from the undisturbed side of the normal star. We can thus easily determine the AD colors observed at different eclipse phases [30].

In Fig. 5, the mean colors of the AD in HZ Her which correspond to different parts of the eclipsed disk region are indicated by the open diamonds; the upper diamond corresponds to half the disk at the beginning of the X-ray eclipse. The total colors of the AD are close to the colors of main-sequence B1–B5-stars (B5 corresponds to the outer, colder parts of the disk). The colors of the additional radiation in A0535+26/V725 Tau, first, are far from the AD colors and, second, exhibit a completely different pattern of variations with total flux. We therefore conclude that the contribution of the AD in this system is very small and unlikely exceeds a few percent.

This figure also shows the color variations of the additional radiation during the giant outbursts of 1980 and 1994 and the normal outburst of 1983. The X-ray outbursts are known to be divided into giant and normal outbursts only by the amplitude, but we do not know whether they are different in nature. However, Motch *et al.* [8] assume that a transient AD is formed around the neutron star during giant outbursts and that stellar-wind accretion takes place during normal outbursts. The first giant outburst occurred in late April–early May 1975, when the object's visibility season for ground-based observations had ended. The 1980 and 1994 outbursts were extensively observed in X rays and optically.

Numbers 1–5 without symbols in Fig. 5 indicate the color behavior of the additional radiation during the giant outburst of 1980 (G80). The color variations correspond to the variations both in temperature and in optical depth: A month before the outburst (1, 2), the temperature was higher, while the optical depth was smaller than those at the maximum (3); the minimum temperature and the maximum optical depth were observed ten days after the maximum (4); and a month after the maximum, the state was approximately the same (5) as a month before the maximum. The color variations during the normal outburst in October 1983 (N83, 6–9) were completely different in pattern. First, the circumstellar envelope became optically thin in the Balmer continuum, and, second, the optical depth in *UBV* decreased at the maximum (8). The colors during the giant outburst of 1994 (10–14) exhibited approximately the same behavior; i.e., the nature of the 1994

outburst is apparently the same as that of a normal outburst, but the nature of the outburst in 1980 (and most likely in 1975) is clearly completely different.

DISCUSSION

This article is a continuation of the series of papers [1, 7, 31] on the study of long-term variability in the Be/XR binary system A0535+26/V725 Tau. Previously, the following conclusions were reached: The circumstellar envelope (disk) is responsible for the object's optical variability; there is no evidence for the presence of a second variable source (an AD around the neutron star); the long-term (years or, possibly, months) variability of $EW(\mathrm{H}\alpha)$ correlates with the V magnitude and the $B–V$ color, but there is no such correlation for V/R (the ratio of the violet and red emission peaks), although the V/R ratio varies in a fairly wide range, possibly periodically with a period of about a year. If this period is interpreted as the period of the global one-armed oscillation (GOAO), i.e., as distortions of the circumstellar disk in the form of a one-armed density wave, then it turns out to be the shortest among the known periods for Be stars.

The infrared observations in 1992–1995 [31] show that, first, not only the long-term but also the fairly rapid (of the order of a month) infrared variability correlates well with the optical variability. Second, the density in the circumstellar disk was estimated from the intensity of Paschen and Brackett emission lines (Pa11–Pa20 and Br11–Br20; the transition between the optically thin and optically thick radiation corresponds to Pa13–Pa15 and Br13–Br17) to be $N_e = (0.15–1.5) \times 10^{12}$ cm^{-3}. This value is in good agreement with our estimate $N_e = 10^{10}–10^{12}$ for a brightness lower than $V = 9\overset{m}{.}1–9\overset{m}{.}2$ (see Fig. 4); in 1992–1995, the brightness declined, on the average, from $9\overset{m}{.}0$ to $9\overset{m}{.}4$.

The photometric behavior of the star closely matches the behavior of a Be star during envelope ejection [6]. The pseudophotospheric temperature may decrease by a factor of 3 or 4, while the radius may increase by one order of magnitude or more. In our case, the B0III star has a radius of $\sim 15R_\odot$ and T_e = 28 000 K for $m_V = 9\overset{m}{.}50$ (at minimum). The colors at this minimum correspond to a spectral type slightly earlier than B0 (recall that the object's spectral type is O9.7IIIe). However, in 1953–1956, twenty years before the outburst, the colors corresponded to a spectral type slightly later than B0 (see Figs. 4 and 5); i.e., the stellar temperature turned out to be higher after the outburst when the shell phase ended. The star apparently "prepared" for the envelope ejection in the 1950s.

At maximum light m, $m_V = 8\overset{m}{.}85$, but the colors correspond to a blackbody with $T_e \sim 12\,000$ K. In order not only to offset the decrease in temperature but also to ensure the increase in luminosity, the radius of the emitting surface must increase tenfold. Thus, at maximum light we see not the B0 star but its cooler pseudophotosphere with an effective radius of $\sim 150R_\odot$. This is probably the reason why there is a confusion with the distance determination for the object. For example, assuming that $M_V = –4.9$ (B0III) and $m_V = 8.9$, Wade and Oke [19] give a distance of 1.8 kpc. The same value was obtained by Giangrande *et al.* [3] for the spectral type O9.7IIIe and $m_V = 8.85$. Margon *et al.* [18] obtained a distance of 3.6 kpc by assuming that $M_V = –6$ (supergiant), while Janot-Pacheko *et al.* [32] give 2.6 kpc. The largest distance of 4.8 kpc was obtained by Stier and Liller [16]. In all cases, the visual absorption A_V was assumed to be approximately the same, but all authors made the same mistake: the brightness at maximum was assumed to be that of the B0 star. In reality, the brightness at maximum is attributable to the emission from the circumstellar envelope with a much lower temperature, and only at minimum ($m_V = 9.50$) does the apparent magnitude correspond to the B0 star. Taking this into account, we obtained a distance of 2.9 kpc by assuming that the luminosity is $M_V = –5.0$ for the currently firmly established spectral type B0III. But the X-ray luminosity then turns out to be appreciably

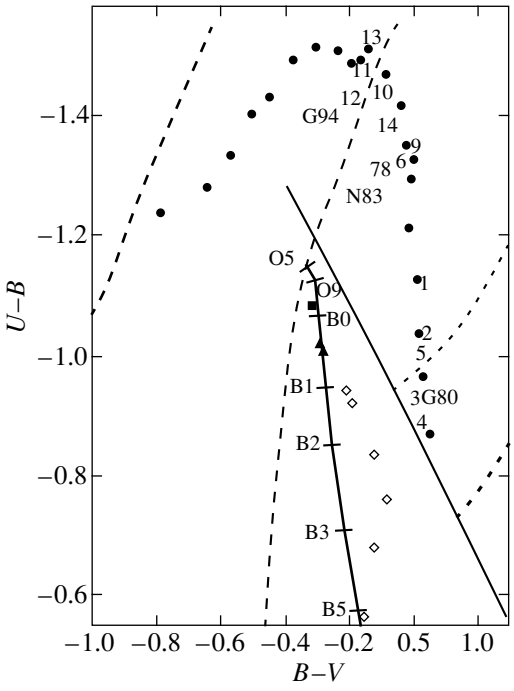

Fig. 5. Color variations (the numbers from 1 to 14) of the additional radiation during the giant X-ray outburst of 1980 (G80), the normal outburst of 1983 (N83), and the giant outburst of 1994 (G94). Numbers 3, 7, 8, and 12 correspond to the outburst maxima. The open diamonds give the positions of the mean color indices for the AD in HZ Her/Her X-1 for various fractions of the eclipsed AD part [30]; the upper diamond corresponds to half the AD observed at the beginning of the X-ray outburst. The remaining notation is the same as that in Fig. 4.

higher: $L_x = (1.5–2) \times 10^{-37}$ erg s^{-1} for giant outbursts at a distance of 1.8 kpc and is a factor of 2.5 higher at $D = 2.9$ kpc.

CONCLUSION

Here, we present the *UBV* observations of the X-ray Be/XR binary system A0535+26/V725 Tau after 1988 and analyze all photoelectric *UBV* observations of the object (1973–1998) and its photographic observations since 1898. The X-ray activity is associated with the outburst of the Be star that began after 1970 and that is attributable to envelope ejection. The optical *V* luminosity reached a maximum in 1975, when the largest (in amplitude and duration) X-ray outburst was observed. The envelope dispersed almost completely in the fall of 1998; the colors at the minimum of 1998 (*minimum minimorum*) correspond to a spectral type slightly earlier than B0, while the colors in 1953–1956 (before the outburst) correspond to a slightly later spectral type than B0; at the same color excesses, i.e., after the outburst (the completion of the shell phase), the star became slightly hotter. All the additional (relative to the Be star) radiation is attributable to a single source, the circumstellar envelope (disk), and the contribution of the AD around the neutron star does not exceed a few percent.

The star appears to have passed all activity phases of Be stars: B–Be–Be shell–B. The Hα line was in absorption in the fall of 1998, the maximum intensity of the emission line was observed at the maximum light in 1975–1980, and the intensity of the Hα emission line decreased with declining brightness. The star has been known as a definitely emission-line star since 1942 [33], while in 1922 and 1926, it was classified as B0 [16].

In general, the optical behavior of the star is consistent with the existing theory of Be stars, except for the appearance of quasi-periodic light fluctuations ($P \approx 1400^d$) with an amplitude $\Delta V \approx 0\overset{m}{.}3$ after 1980, when the second giant X-ray outburst was observed. Since the circumstellar envelope dispersed almost completely in the fall of 1998, it would be unreasonable to expect strong X-ray outbursts in the coming years. The object will most likely be a weak X-ray source, as it was before 1975 [34]. The recurrence period of the envelope ejection in A0535+26/V725 Tau is not known. However, since only one such episode ~25 years in duration was observed in the 20th century, the next episode will not occur soon.

ACKNOWLEDGMENTS

We wish to thank A.A. Aslanov for the 1980 observations and A.E. Tarasov, who provided the spectroscopic data of 1998.

REFERENCES

1. J. S. Clark, A. E. Tarasov, I. A. Steele, *et al.*, Mon. Not. R. Astron. Soc. **294**, 165 (1998).
2. F. Giovannelli and L.S. Graziati, Space. Sci. Rev. **59**, 1 (1992).
3. A. Giangrande, F. Giovannelli, C. Bartolini, *et al.*, Astron. Astrophys. Suppl. Ser. **40**, 289 (1980).
4. Yu. N. Gnedin, G. V. Zaĭtseva, V. M. Larionov, *et al.*, Astron. Zh. **65**, 1196 (1988).
5. V. M. Lyutyi, G. V. Zaĭtseva, and I. D. Latysheva, Pis'ma Astron. Zh. **15**, 421 (1989) [Sov. Astron. Lett. **15**, 182 (1989)]
6. H. J. Lamers, *Instabilities in Luminous Early Type Stars*, Ed. by H. J. Lamers and C. W. de Loore (Reidel, Dordrecht, 1987), p. 99.
7. J. S. Clark, V. M. Lyutyi, G. V. Zaĭtseva, *et al.*, Mon. Not. R. Astron. Soc. **302**, 167 (1999).
8. C. Motch, L. Stella, E. Janot-Pacheco, *et al.*, Astrophys. J. **369**, 490 (1991).
9. M. H. Finger, R. B. Wilson, and B. A. Harmon, Astrophys. J. **459**, 288 (1996).
10. F. Lenouvel and C. Flogèr, J. Obs. **40**, 1 (1957).
11. S. Rössiger, Mitt. Ver. Sterne **7**, 105 (1976).
12. S. Rössiger and W. Wenzel, Astron. Nachr. **295**, 47 (1974).
13. C. de Loor, F. Giovannelli, E. L. van Dessel, *et al.*, Astron. Astrophys. **141**, 279 (1984).
14. R. A. Sunyaev and the Kvant Team, IAU Circ. No. 4769 (1989).
15. W. A. Hiltner, Astrophys. J. Suppl. Ser. **2**, 389 (1956).
16. M. Stier and W. Liller, Astrophys. J. **206**, 257 (1976).
17. S. Rössiger, Die Sterne **55**, 76 (1979).
18. B. Margon, J. Nelson, G. Chanan, *et al.*, Astrophys. J. **216**, 811 (1977).
19. A. Wade and J. B. Oke, Astrophys. J. **215**, 568 (1977).
20. G. B. Baratta, R. Viotti, and A. Altomore, Astron. Astrophys. **65**, L21 (1978).
21. N. F. Voĭkhanskaya and M. D. Metreveli, Astron. Zh. **56**, 450 (1979).
22. N. F. Voĭkhanskaya, Pis'ma Astron. Zh. **6**, 582 (1980) [Sov. Astron. Lett. **6**, 305 (1980)].
23. O. É. Aab, L. V. Bychkova, I. M. Kopylov, *et al.*, Pis'ma Astron. Zh. **8**, 179 (1982) [Sov. Astron. Lett. **8**, 94 (1982)].
24. O. É. Aab, Astron. Zh. **62**, 339 (1985).
25. A. E. Tarasov, Private Communication (1998).
26. N. N. Chalenko, Astron. Zh. **76**, 529 (1999).
27. N. I. Shakura and R. A. Sunyaev, Astron. Astrophys. **24**, 337 (1973).
28. M. M. Basko and R. A. Sunyaev, Astrophys. Space Sci. **23**, 117 (1973).

29. V. M. Lyutyi and R. A. Sunyaev, Astron. Zh. **53**, 511 (1976).
30. E. K. Sheffer and V. M. Lyutyi, Astron. Zh. **74**, 209 (1997).
31. J. S. Clark, I. A. Steele, M. J. Coe, and P. Roche, Mon. Not. R. Astron. Soc. **297**, 657 (1998b).
32. E. Janot-Pacheco, C. Motch, and M. Mouchet, Astron. Astrophys. **177**, 91 (1987).
33. P. W. Merrill and C. G. Burwell, Astrophys. J. **98**, 153 (1943).
34. W. C. Priedhorsky and J. Terrell, Nature **303**, 681 (1983).
35. S. Rössiger, IAU Circ. No. 3184 (1978).

Translated by V. Astakhov